Excitonic and Raman Properties
of ZnSe/ $Zn_{1-x}Cd_xSe$
Strained-Layer Quantum Wells

Dissertation Presented to

the Faculty of the College of Engineering and Technology

Ohio University

In Partial Fulfillment

of the requirements for the Degree

Doctor of Philosophy

by

Vasant K. Shastri

November, 1991

ABSTRACT

This dissertation presents for the first time the detailed excitonic and Raman scattering investigations of strained-layer single quantum-well ZnSe/ $Zn_{1-x}Cd_xSe$ heterostructures. Recently, the existing group of molecular-beam epitaxially (MBE) grown II-VI materials has been enlarged by the successful growth of cubic (zinc-blende) CdSe and $Zn_{1-x}Cd_xSe$ on GaAs substrate. The heteroepitaxy of $Zn_{1-x}Cd_xSe$ on (100) GaAs by MBE results in single-phase zinc-blende crystals over the entire composition range from CdSe to ZnSe. In wide-gap II-VI semiconductors the luminescence spectra are dominated by excitonic transitions involving the electron subbands and hole subbands.

The photoluminescence under direct and indirect excitations are investigated in detail to study the carrier generation, transport and recombination mechanisms. The temperature dependence of photo-luminescence and resonant Raman scattering are investigated to study the exciton-phonon interaction and luminescence quenching mechanisms. Very strong 2LO phonon Raman scattering has been observed with single $Zn_{0.86}Cd_{0.14}Se$ quantum wells, where the scattered photon energy is in resonance with an exciton transition. The experimental confined exciton energies are compared with a finite-square potential-well model including band-nonparabolicity. The

TABLE OF CONTENTS

ACKNOWLEDGEMENTS

LIST OF FIGURES

LIST OF TABLES

CHAPTER 1

INTRODUCTION

1.1 General Background:

In the recent years, significant developments have taken place in the field of semiconductor heterojunctions, quantum-wells (QWs'), and superlattices (SLs') and their optoelectronic device application. The early researches (1969) and proposal by Esaki and Tsu [1,2] envisioned two types of layered-structures: namely doping and compositional type. The QW and superlattice idea emerged during their feasibility examination of growing layered-structures by epitaxy, especially for ultrathin wells and barriers, thin enough to exhibit resonant electron tunneling through the well/ barrier layers. Resonant tunneling arises from the interaction of electron waves with potential barriers. If the characteristic dimensions like the QW width, the periodicities in multi-quantum-wells (MQWs') are reduced to less than the electron mean free path λ, the entire system will enter a quantized regime of reduced dimensionality in the presence of nearly ideal interfaces. High quality heterostructures can have designed potential profiles and impurity distributions with dimensional control close to inter-atomic spacing and with defect-free interfaces. This

great precision has opened a window of opportunities for design and fabrication of devices in the quantum regime.

The growth of thin layers of different semiconductors by novel techniques like molecular-beam-epitaxy (MBE) and metal organic chemical vapor deposition (MOCVD), have enabled the growth of extremely high quality epitaxial interfaces. This offers the possibility to fabricate a large variety of artificial semiconductor structures; not only between lattice-matched, but even between materials which differ in lattice constants by several percent. Quantum-well structures in III-V compounds have attained significant importance because of their unique electronic properties;that can be tailored through choice of materials and layer thickness, allow promising application in modern semiconductor device technology. The wide-gap II-VI compounds are less studied as compared to III-V compounds, offer the possibility to fabricate optical devices from blue region to far-infrared region of the spectrum. Examples of such novel semiconductor structures include light-emitting diodes (LEDs'), lasers, optical modulators, MQW/ SL photo-detectors, and high-speed modulation-doped field-effect transistors (HS-MODFETs'). Superlattices from II-VI compound semi-conductors are particularly promising for optoelectronic devices for blue light-emitting-diodes (LEDs'), tunable color LEDs', and short wavelength semiconductor lasers.

The intriguing features of these QW structures basically arise from the localization of electron and hole wavefunctions which for small well-width, results in a quasi-two-dimensional (2D) carrier system. The optical properties of a quasi-2D system exhibit many unique characteristics which are different than those of bulk semiconductors.

When the lattice parameters of the bulk compounds are different, the hetero-layers are strained. These strains can cause profound changes in the electronic and optical properties and thus providing an extra degree of freedom in the device design. In a strained-layer superlattice (SLS) or strained-layer-quantum-well (SL-QW), lattice-mismatch is accommodated by elastic strain, rather than generation of misfit dislocations; provided that the layer thickness is less than some strain-dependent critical value.

The fundamental physical property that determines the possible application of a given heterojunction is the relative lineup of the band structures of the two materials joined at the interface (called as the band-offset). Theory of band-offsets have been reviewed extensively by several authors [7,14,16,18,60].

In wide-gap II-VI semiconductors the luminescent spectra are dominated by excitonic transitions involving the electron subbands

and hole subbands. Recently, the existing group of MBE grown II -VI materials have been enlarged by the successful growth of cubic (zinc-blende) CdSe and $Zn_{1-x}Cd_xSe$ on a (100) GaAs substrate by Samarth and Furdyna [65,66]. CdSe exists in wurtzite (WZ) structure in nature and bulk grown $Zn_{1-x}Cd_xSe$ is obtained over the entire composition range (0 < x < 1) and changes from zinc-blende (ZB) to wurtzite when composition x > 0.5, the interval 0.5 < x < 0.7 being the range of structural phase transitions [47]. In contrast, the heteroepitaxy of $Zn_{1-x}Cd_xSe$ on (100) GaAs by MBE results in single-phase zinc-blende crystals over the entire composition range from CdSe to ZnSe [65,66].

Observations of Raman scattering resonant with excitons in III-V QWs' and SLs' have been reported in the literature [44,45,52,67-69]. Two excellent review articles of experimental and theoretical results of the exciton-phonon interaction in QWs' and SLs' have been published [51,53].

1.2 Objectives and Organization:

The objective of this dissertation is to perform for the first time, the detailed excitonic and resonant Raman scattering investigations of strained-layer single quantum-well (SQW) ZnSe/ $Zn_{1-x}Cd_xSe$ hetero-structures. This particular investigation seems to be suitable for the

realization of narrow band emitters for a blue region of the visible spectrum. Photoluminescence (PL) spectra of the SQW hetero-structures are studied in detail. Lattice-mismatch as high as 1.011 % exists in single ZnSe/ $Zn_{1-x}Cd_xSe$ / ZnSe quantum wells with x=0.14. The strain effect shifts the band gap energy in the well and removes the degeneracy present at the zone center. The strain-induced effects on band structure and the energy transitions by confined carriers are calculated and observed in the PL spectra. The PL process like the generation of carriers, carrier transport and their confinement are analyzed in detail. The confined carrier (electrons and hole) energies are computed using a finite-square-potential well model. Resonant Raman scattering are observed for the first time in $Zn_{1-x}Cd_xSe$ quantum wells. Experimental results are compared with the theoretical model and calculations. The temperature dependencies of peak position, their intensities, and the linewidth are determined.

The dissertation is organized as follows: In Chapter 2, physics and applications of quantum-well structures, their evolution, theory of heterojunction band-lineup, electron states, strain and effect of strain on the optical properties of these structures are reviewed. Chapter 3 describes the spectroscopic techniques used to study the optical properties of the quantum-well structures. The results of photo-luminescence measurements are presented and observed features are

discussed. Experimentally observed radiative transitions are ascribed as free-exciton and bound-exciton transitions. Temperature dependence of photoluminescence and resonant Raman scattering are discussed in detail. Results of circular polarization measurements are also presented. In Chapter 4, the bandgap of $Zn_{1-x}Cd_xSe$ quantum-well as a function of composition is computed. The confined carrier energies are numerically computed by modeling single quantum-wells as finite-square-potential wells. Strain and strain effects on the energy of transition from heavy-hole, light-hole and splitoff-bands are computed. Experimental results are compared with the theoretical models and calculations. Conclusions and recommendations for future work are given in Chapter 5. Appendices list the special programs written to calculate the confined carrier energies, strain-shift due to heavy-hole, light-hole and split-off bands, together with sample calculations.

CHAPTER 2

LITERATURE REVIEW

Layered-structures like quantum-well and superlattices offer unique electronic and optical properties, and hence find importance in custom designed optoelectronic devices. By techniques like MBE and MOCVD, it is possible to grow ultrathin epitaxial layers and tailor the electronic properties, by varying the composition between the two semiconductors and by the layer thickness. The crucial parameters that govern the electronic properties of the heterojunction are the bandedge discontinuities.

In this chapter, starting from the fundamental concepts of QW structures, the theory of band lineup, electron states in a QW, strain in lattice mis-matched systems and the effect of strain on transition energies are reviewed.

2.1 Physics and applications of semiconductor quantum-well Structures:

Advances in the semiconductor technology have facilitated the fabrication of microstructures with dimensions in the atomic scale.

The availability of this class of semiconductor structures create new opportunities for the investigation of the physics of condensed matter under conditions of reduced dimensionality. In the case of electrons, quantum size effects occur when the physical dimensions are comparable to the characteristic lengths that determine the electron behavior, like the mean free path. These lengths range between 10 Å to 1000 Å.

New physics and novel devices are possible because of control of composition and doping of theses layered structures. These layered structures reveal a great wealth of physical phenomena. The existence of a 'unique axis' along the direction normal to the layers, which represents the direction in which the electron moves, is strongly altered by the ultrathin layers in the structure. On the other hand, the carriers' motion parallel to the plane of the layers is not substantially altered. Thus, semiconductor heterostructures can be fabricated with tailored composition and doping profiles, such that carriers are confined within one type of layers or quantum wells. This confers to carriers a quasi-two-dimensional character, that is at the center of some most exciting developments in experimental and theoretical semiconductor physics today. The unique features that attract much attention are the high mobility observed in 'modulation doped' heterojunctions and the enhanced optical properties seen close to the band gaps of quantum-well heterostructures. Periodic multi-layer

structures form superlattices, in which the folding of the Brillouin zone, strongly effects the energy band structure and symmetry selection rules, as compared to bulk semiconductors.

2.2 Evolution of semiconductor quantum wells and superlattices:

The early research on semiconductor superlattices was initiated with a proposal by Esaki and Tsu [1,2] for a one-dimensional potential structure engineered with epitaxy of alternating ultrathin layers (Fig. 1). The superlattice structures possess an unusual electronic property of quasi-two dimensional character [1,2]. The introduction of the superlattice potential perturbs the band structure of the host materials. Since the superlattice period is much longer than the original lattice constant, the Brillouin zone is divided into a series of minizones, causing narrow subbands, separated by forbidden regions [3] (Figs. 2 a & b).

Heteroepitaxy is of fundamental interest for the superlattice growth. The dimensions of these structures are controlled close to interatomic spacing and with almost defect-free interfaces. This great precision has cleared access to quantum regime. Semiconductor interfaces exhibit an abrupt discontinuity in the local band structure, usually associated with a gradual band bending in its neighborhood that
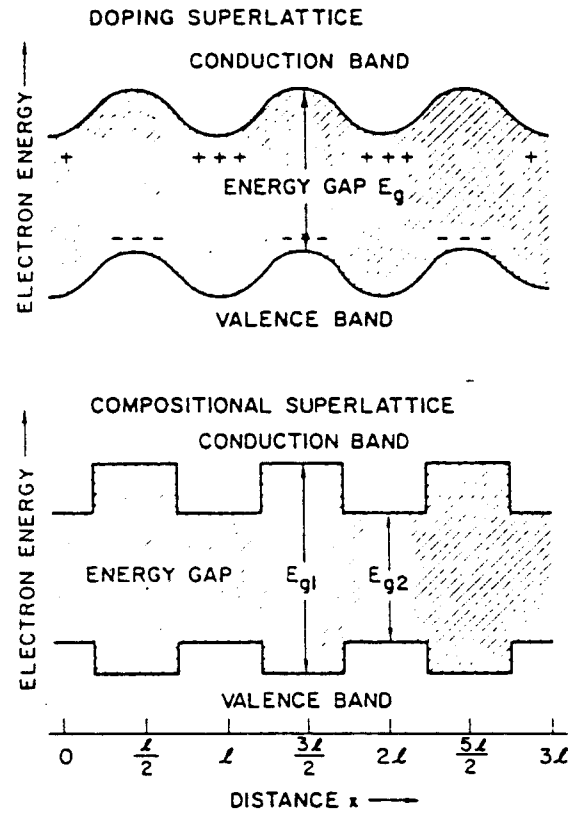
Figure 1.   Spatial variation of the conduction and valence bandedges in doping (top) and compositional (bottom) type layered structures [1,2].
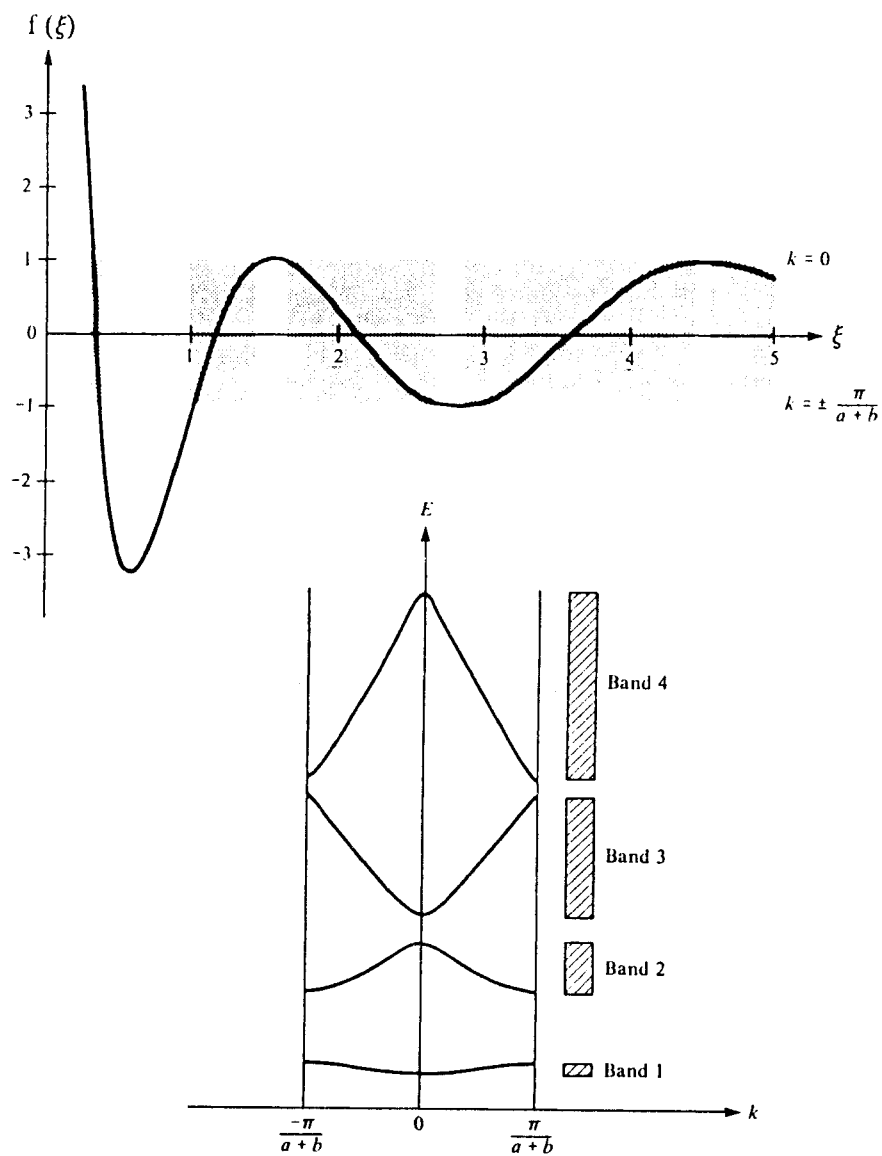
Figure 2 a. Kronig- Penney band model, reduced zone
representation.
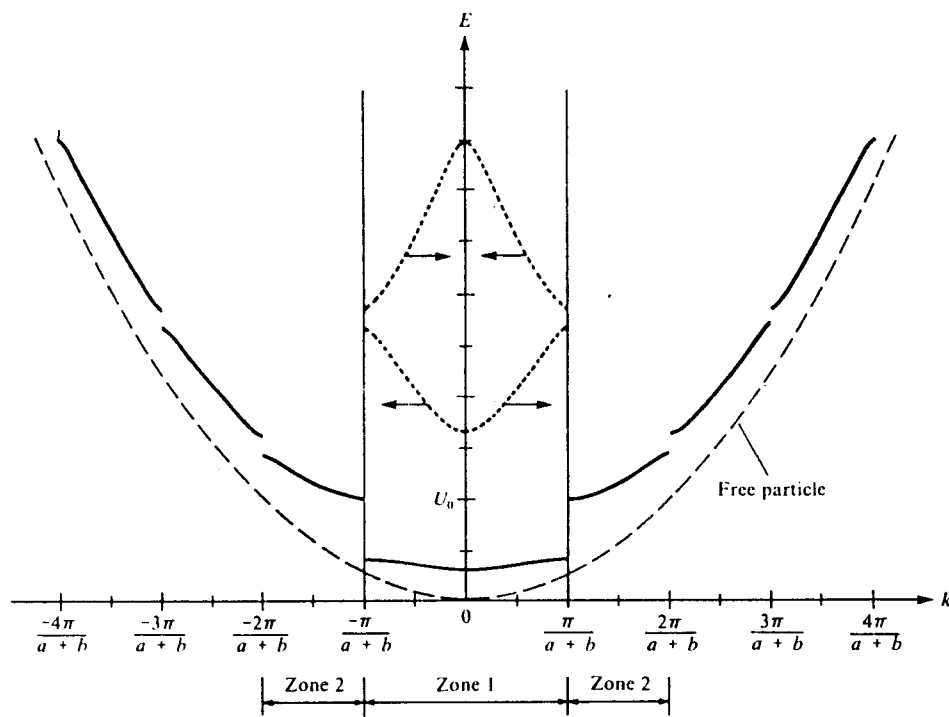
Figure 2 b. Kronig- Penney band model, extended zone representation.
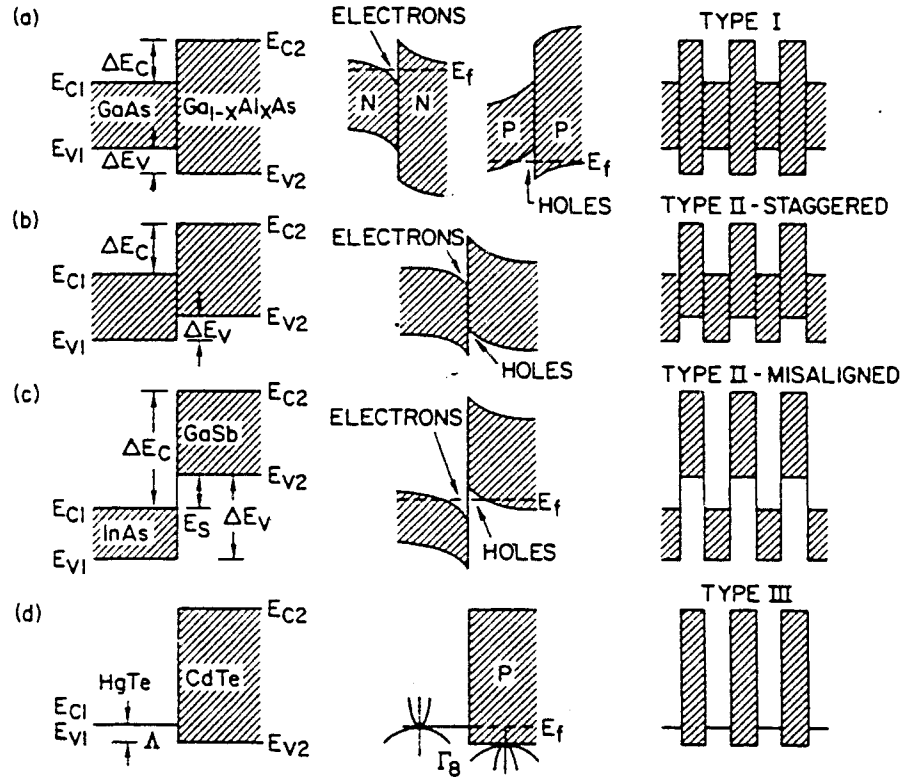
Figure 3.   Bandedge discontinuities in four different types of hetero-interfaces: band-offset(left), band bending, carrier confinement (middle), and superlattices (right) [1,2].

reflects space-charge effects. According to such discontinuity, the hetero-interfaces are classified into 4 kinds: Type I, Type II-staggered, Type II-misaligned, and Type III. The conduction-band discontinuity is denoted as ΔE_c and the valence-band discontinuity is denoted by ΔE_v between the two semiconductors. Figure 3 illustrates four different types of superlattices.

Type I applies to GaAs- AlAs, GaAs -GaP systems, etc., where their energy difference $\Delta E_g = \Delta E_c + \Delta E_v$. Type II staggered and misaligned apply to pairs of InAs-GaSb, InP-Al$_{1-x}$In$_x$As systems, etc., where their energy gap difference $\Delta E_g = |\Delta E_c - \Delta E_v|$ and electrons and holes are confined in the different semiconductors at their heterojunctions. In Type III the system is similar to HgTe-CdTe, where one of the constituent is semimetallic.

The bandedge discontinuities at the hetero-interfaces command all the properties of quantum wells and superlattices, constituting a most important parameter for the device design.

Optical investigation of these layered structures has revealed the salient features of quantum confinement. Dingle et al. [4] observed pronounced peaks in the optical absorption spectrum, representing bound states in single and double quantum wells. In the low-temperature measurements for such structures, several exciton peaks,

associated with different bound-electron and bound-hole states can be resolved.

Bandgap engineering consists of tailoring of associate materials to custom design the band structure of the heterostructure for some desired properties, unattainable in homostructures. The range of materials now grown in ultrathin layers is extremely wide. Some degree of the lattice-mismatch, yet small, at the hetero-interface is inevitable, because of the joining of the two different semiconductors. It is certainly desirable to select a pair of materials closely lattice-matched to obtain defect and stress-free interfaces. But, heterostructures lattice-mismatched, by 1 - 5% can be grown with no misfit dislocations, if the layers are sufficiently thin. This is because the mismatch is accommodated by uniform lattice strain [5,6]. The realization of this effect has lead to the development of ultrathin multilayer structures with a much wider group of materials. Within the allowed range, the choice of layer thickness allows one to select a strain value that offers an additional parameter for tailoring of electronic properties.

2.3.1 Theory of heterojunction band lineup:

The crucial parameters which determine the electronic behavior of the heterojunction are the valence and conduction band-edge discontinuities. These discontinuities are dependent, and are colletively referred as the band-lineup. Band-lineups determine the barrier for hole or electron transport across the interface, and act as boundary conditions in the calculation of band bending and electrostatic features.

Because the bandgaps of the two semiconductors $E_g(A)$ and $E_g(B)$ at the heterojunction are in general different, there is always a discontinuity in one or both band-edges at the interface. Figure 4 illustrates the band discontinuities between A and B semiconductors.

The valence-band discontinuity is given by

$$\Delta E_v(A, B) = E_v(B) - E_v(A) \qquad (2.1)$$

and the conduction-band discontinuity ΔE_c is given by

$$\Delta E_c(A, B) = E_c(B) - E_c(A) \qquad (2.2)$$

These discontinuities are related by

$$\Delta E_g = |\Delta E_c - \Delta E_v| \qquad (2.3)$$

where ΔE_g is the band gap difference between materials A and B.
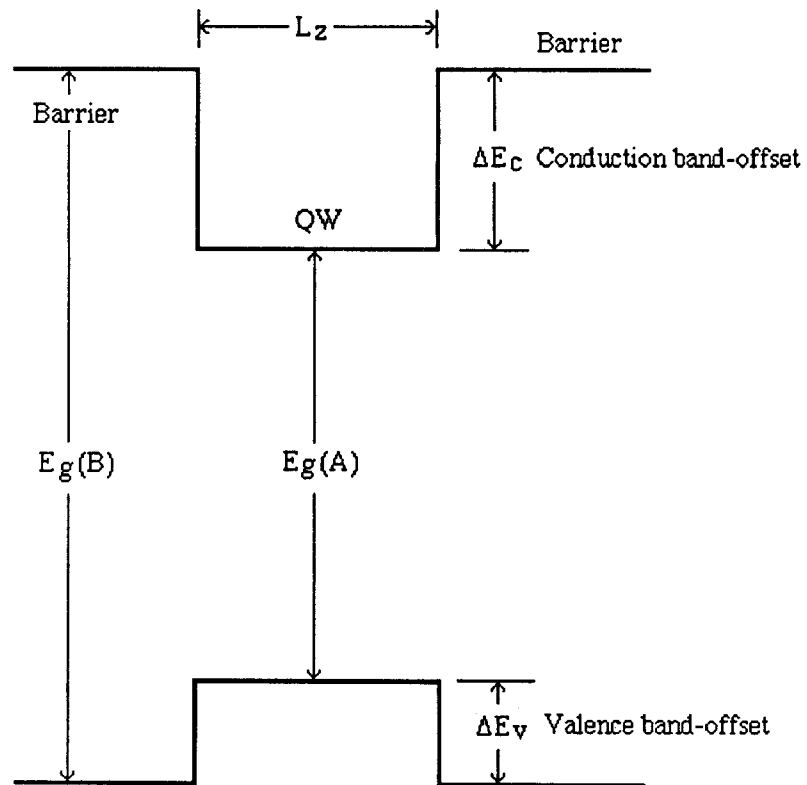
Figure 4.   Energy-band diagram for a semiconductor-semi-
conductor interface, illustrating the conduction-
band and valence-band offsets [17].

Either the valence-band discontinuity or the conduction-band discontinuity is sufficient to specify the band lineup, which is independent of the doping profile.

The band lineup or band offset, is an important consideration for the design of a device. The band lineup problem holds a special place in basic heterojunction interface physics, since it is one of the well-defined interface problems. In the above discussion, the band lineup problem amounted merely to determine the band-edge discontinuities at a given interface. However, in practice the problem is more complicated.

The theory of band lineup includes a variety of methods and approaches for solving the problem, and can be broadly divided into three categories. The first category consists of numerical calculations of the complete electronic structure of a specified interface. The accuracy of this approach is limited by the approximations made, in practice. The second category is the theoretical work, involving qualitative analysis of the problem, leading to model theories. Finally, the third category of work consists of analysis of electronic properties of the interface, given the band lineup, which includes quantum-well exciton energies, luminescence spectra, and impurity states at the

interface, etc. A critical review of this problem has been done by Tersoff [7].

The flexibility in a heterojunction originates from the use of two different semiconductors with two different sets of parameters, the most important of which are the minimum forbidden gaps E_g (A) and E_g (B) at the interface. The difference $\Delta E_g = E_g$ (A) - E_g (B) gives rise to valence-band discontinuity ΔE_v and the conduction-band discontinuity ΔE_c. This band discontinuity plays a leading role in determining the transport and optical properties of the interface.

The first fundamental step was formulated by Anderson's 'electron affinity rule' [8]. Many researchers have developed surface-sensitive experimental techniques [9], for example photoemission spectroscopy. In the recent years, the advent of these techniques has stimulated a renewed theoretical interest in this problem, and the formulation of several new discontinuity models [10,11]. The definition of the discontinuity problem is provided by practical aspects of device applications. The control of ΔE_v and ΔE_c must achieve an accuracy better than kT at room temperature, i.e., ± 0.25 meV. Therefore, the research goal is the formulation of theoretical approach capable of predicting ΔE_v and ΔE_c with the above mentioned accuracy.

In Anderson's approach [8], the relevant property of each semiconductor is its electron affinity. The basic prediction of this model is that the valence-band discontinuity is given by the difference between the electron affinities of the two semiconductors, $\Delta E_c = \chi_B - \chi_A$. Anderson's model is a general purpose theory, and given any two semiconductors, one substitutes the corresponding electron affinities and finds ΔE_c (see Table I). From an empirical point of view, the electron affinity is measured by extracting electrons from the semiconductors, and therefore, it is influenced by the interfaces between the surface and vacuum. The electron affinity rule uses a linear combination of the results of such measurements to describe all the factors contributing to the discontinuities.

A practical problem affecting the electron affinity rule is the difficulty in measuring the electron affinities, and the consequent lack of a more comprehensive and reliable data base. There is a discrepancy between theory and experimental results, in computation of band lineups using electron affinity rule (EAR). The failure of the EAR increases the emphasis on other linear models. The EAR rule, expresses the discontinuities in terms of the absolute position in energy of the valence-band edges of the two semi-conductors. Other models follow the same pattern, trying to identify a reference energy

TABLE I

Semiconductor parameters

Material	E_g, minimum bandgap* (eV, room temp.)	Electron affinity** (eV)
CdS	2.42	4.79
CdSe	1.74	4.95
CdTe	1.44	4.28
ZnS	3.54	3.9
ZnSe	2.58	4.09
ZnTe	2.26	3.53

* from CRC Handbook of Chemistry and Physics.

** from Reference [76].

level (the vacuum level for the EAR), then to estimate the absolute position in energy of the valence-band edges, E_v (A) and E_v (B). Finally ΔE_v is predicted from the absolute positions, $\Delta E_v = E_v$ (B)- E_v (A).

The problem of finding a theory capable of calculating the valence-band edge positions with respect to some absolute reference level. Harrison [12] emphasized that the simplest and meaningful band calculations which place all systems on the same scale are the 'tight-binding' calculations based upon universal parameters. Thus, this approach is best suited to find E_v terms for different semiconductors, whose differences define the band lineup ΔE_v. Harrison's approach is quite accurate to experimentally determined band-offsets.

In Frensley- Kroemer model, a pseudopotential approach is used to estimate the valence-band edge positions [13]. The reference energy in each semiconductor is the interstitial potential V_1, which is the average of the electrostatic potentials at the midpoints between adjacent atoms. The result of this approach is its linear character, including dipole corrections. The Microscopic study of semiconductor heterojunctions by photoemission measurements [14] and problem of heterojunction band discontinuities has been reviewed by Margaritondo et al. [14].

2.3.2 Nature of valence-band edge discontinuity:

To obtain insight into the nature of the band edge discontinuity, one relies on the combination of experiment and theory. Theory provides predictions based on certain assumptions. Then a comparison between experimental results and theoretical predictions provides a verification of those assumptions and can help identify the origin of the physical property. Detailed theoretical calculations are complex and lack in accuracy, and have lead the researchers to rely on some semiquantitative theories.

A number of semiquantitative approaches have been proposed to describe the band edge discontinuity. Such approaches include Anderson's electron affinity rule [8], Harrison's LCAO model [12], Frensley- Kroemer pseudo-potential model [13], and induced gap state model by Tersoff [15]. Below a short description of the essential features of various semiquantitative theories are discussed:

1. Anderson's model:

In a heterojunction, the vacuum level is parallel to the band edges and continuous throughout the junction in the absence of dipole layers. Under these assumptions the conduction-band discontinuity can be expressed as the difference between the electron affinities (χ_1 and χ_2)

of the two semi-conductors forming the heterojunction, $\Delta E_c = \chi_1 - \chi_2$. This model has some practical drawbacks, such as the accurate measurement of electron affinity to predict ΔE_c.

2. Frensley and Kroemer's model:

According to Frensley and Kroemer, the average interstitial potential derived from the electrostatic part of the total periodic potential for the bulk semiconductor, is continuous throughout the interface in the absence of dipole layers. On this basis, they calculated the valence-band maximum with respect to the average interstitial potential using the self-consistent pseudopotential approach for the bulk materials. The valence-band discontinuity is given by, $\Delta E_v = E_v(B) - E_v(A)$, where $E_v(A)$ and $E_v(B)$ are the valence-band positions of the two semiconductors as given by pseudopotential calculations. This model has been later modified to include the interface dipoles. The modification is a correction determined from the relative electro-negativities of the constituents of the semiconductors.

3. Harrison's model:

In this model, the valence-band maximum is calculated by the linear combination of atomiclike orbital (LCAO) approach, for the bulk semiconductors. The valence-band discontinuity is given by $\Delta E_v =$

$E_v(B) - E_v(A)$, where $E_v(A)$ and $E_v(B)$ are the calculated valence-band maxima of the two semiconductors. The calculation of valence-band maxima includes the p-atomic energy states of the anion and cation of the semiconductor and the interatomic distances.

4. Tersoff's model:

According to Tersoff, the mid-gap energy position for a semiconductor should be the reference point to calculate the band discontinuities. The mid-gap energy position is calculated by minimizing the interface dipole that results from the band discontinuity states, is obtained by assuming charge neutrality at the interface and, consequently, zero interfacial dipole. This calculation requires the knowledge of the band structure of the semiconductor under consideration. The band discontinuity is given by $\Delta E_v = E_B(B) - E_B(A)$, where $E_B(A)$ and $E_B(B)$ are the mid-gap energy positions for the two semiconductors forming the heterojunction.

A common feature of the above models is that, they express the band discontinuities as the difference between two terms characteristic of the two semiconductors. Extensive experimental work has been performed over the past two decades to verify the consequences of the above mentioned semiquantitative theories and to asses their accuracy limits. Many of these experiments addressed the

question of the interface and its contribution to the band edge discontinuity. Most experiments sought a parameter by which they would have control over band edge discontinuity, like the consequence of linearity, overlayer ordering, and dependence of surface orientation, etc. Light scattering determinations of band-offsets in GaAs/$Al_{1-x}Ga_xAs$ heterojunction by Menendez et al. [16] is noteworthy. A review of heterojunction interface characteristic and also the theoretical and experimental work related to band discontinuities has been done by A. D. Katnani [17].

Self-consistent calculation of the electronic structure of the interfaces have been performed by several authors [18,19]. Most of these calculations are made with local density approximation (LDA).

Kromer [60] has presented a critical review of theory of heterojunctions. Kromer has presented the results of Harrison theory (HAO) in a simple table form for III-V and II-VI compounds. The energies have been expressed relative to the top of the valence band of GaAs. Specific application of HAO theory and the values from Kromers' table in our calculation will be discussed in Chapter 4.

2.4 Electron states:

Dingle et al. [20] first performed optical measurements on a rectangular GaAs/ $Al_{1-x}Ga_xAs$ quantum-well heterostructure (QWH). The $Al_{1-x}Ga_xAs$ layers were thick enough to ensure that carriers are localized to a GaAs layer. The smaller band gap material sandwiched between layers of larger band gap material (barrier) constituted the quantum-well. The investigations performed on this structure by absorption spectroscopy, concerns the bound states of a particle confined to a one-dimensional QW of thickness L_z, when this thickness is comparable to the de Broglie wavelength of the particle. In this case a discrete spectrum of energy levels is created for the particle in the well. The eigenvalues of the energy relevant to these levels depends strongly on the well thickness L_z. For very large L_z, a continuum of states results and the particle will no longer be in the quantum limit. For an infinitely deep rectangular potential well, the solution to Schrodinger wave equation leads to the energy eigenvalues $E_n = (\hbar^2\pi^2/2m) (n/L_z)^2$, n =1,2,3 .... The dependence of the energy eigenvalues E_n of the bound states in a quantum well on the dimension of the well (L_z in 1D case) is known as the quantum size effect (QSE).

For the particle (electron or hole) subband calculations in quantum-well heterostructure, the effective mass approximation

(EMA) has been the most widely used method [21]. In its simplest form, this method uses the standard time-independent Schrodinger equation separately for the conduction and for the valence bands, respectively, with the mass of electron or hole replaced by its band-edge effective mass. For the background discussion, one can follow the considerations of Bastard and Brum [22] and apply the effective mass envelope function approximation. This approximate theoretical scheme is straightforward and proven efficient leading to analytical results. There are two important considerations: the first, is because most of the host materials forming the heterojunction has similar band structures. The periodic parts of Bloch functions [23] of the relevant band edges do not differ very much from one host material to the other. The second, is connected with the somewhat low excitation level of the carriers in the QW, which has the consequence that the relevant energy states are closer to the band extrema of the hosts. Thus, only a small fraction of the host Brillouin zone participates in the formation of the particle energy states.

In the envelope function scheme, consider the growth direction of the semiconductor heterostructure as the z-axis. The host materials will be called from now on well (W) and barrier (B) of the QW heterostructure, respectively. Each host materials has its own lattice constant, and a band structure characterized by dispersion relations $\varepsilon_n^B(k_B)$, $\varepsilon_n^W(k_W)$ and Bloch functions $\psi_{nk_B}^B(r)$ and $\psi_{nk_W}^W(r)$. The band

edges relevant to optical properties of the discussed quantum-well heterostructure have the Γ_6 (conduction band), Γ_8 (principle valence bands for heavy-holes and light-holes), and Γ_7 (valence band splitoff by Δ from the Γ_8 edge through spin-orbit coupling) symmetries [24]. Under flat band conditions, the quantum-mechanical wave function $\psi^{WB}(r)$ describing the physical states of the particles in the well-barrier layers may be expanded as:

$$\psi^{WB}(\mathbf{r}) = \sum_n C_n^{WB} (\mathbf{k}_\perp, k_z^{WB}) \, u_{n0}^{WB}(\mathbf{r}) \, \exp[i(\mathbf{k}_\perp\mathbf{r}_\perp + k_z^{WB}z)] \qquad (2.4)$$

where $\mathbf{k}_\perp$ (k_x, k_y) and $\mathbf{r}_\perp$ (r_x, r_y) are two-dimensional wave and position vectors respectively, and n is a bulk band index that extends over the host band edges. Notice that, $\mathbf{k}_\perp$ is real, since in the layer plane, the heterostructure has the same transition invariance as the host. On the other hand k_z^{WB} is either real or imaginary, depending on whether the particle energy corresponds to a propagating or evanescent state within the W and B layers, respectively.

The wave function $\psi^{WB}(\mathbf{r})$ is the sum of products of: (i) the envelope functions [slowly varying functions at the scale of the host unit cells- the plane waves in $\psi^{WB}(\mathbf{r})$], (ii) by the rapidly varying periodic parts of band-edge Bloch functions $u_{n0}^{WB}(\mathbf{r})$. It is the clear cut separation between the spatial extensions of the two kinds of terms that underlay the envelope function scheme. The rapidly varying

terms will enter the heterostructure calculations only through effective parameters: with the host crystalline potentials, they fix the bandgaps, interband p-matrix elements, etc. these quantities are assumed to be a priori known in the envelope function approximation. For the slowly varying terms the envelope function f(z), a relevant Schrodinger-like equation governing their spatial behavior, has to be solved [22]. The two simplifying considerations, inherent in the above discussed envelope function approximation, mean that the wave function $\psi^{WB}(r)$ may be restricted only to 8 terms in n, which are relevant to the Γ_6, Γ_7, and twice Γ_8 bands, while the periodic parts of Bloch functions are assumed to be the same in both, the well (W) and the barrier (B) layers.

In type I heterostructures $k_\perp = 0$, and the light-hole and heavy-hole levels decouple. The equations for the envelope functions f(z), relevant to electrons, light-holes and heavy-holes, respectively, have the form [22]

$$- (\hbar^2/2)\, \partial/\partial z \,\{1/m(z) * \partial f(z)/\partial z\} \;+\; V(z)\, f(z) = E f(z) \qquad (2.5)$$

When taking the energy zero for holes at the top of the degenerated Γ_8 band of the bulk W material, and for electrons at the bottom of the Γ_6 band of the W material, then $V(z) = \Gamma_6{}^B - \Gamma_6{}^W = \Delta E_c$ for the conduction band electrons, while $V(z) = - (\Gamma_8{}^B - \Gamma_8{}^W) = \Delta E_v$ for the

light and heavy-holes. The first term on the left-hand side of equation (2) represents the quantum mechanical operator of kinetic energy acting on the envelope function relevant to the specific particle. From physical point of view, this term is finite throughout the quantum-well heterostructure. This requirement leads to the necessary boundary conditions that have to be fulfilled by the envelope functions. Accordingly, both f(z) and {1/m(z) * ∂f(z)/∂z} should be continuous for all values of the z-coordinate, including the QW interfaces at z = ± $L_z/2$.

The f(z) functions can be chosen either even or odd in z. The following equations give the bound states of the particles confined to rectangular quantum-wells [22]

for even f(z) (corresponding to even values of quantum number n):

$$\tan \, (m_W E_n L_z^2/ \, 2\hbar^2)^{1/2} = \{ \, m_W(\Delta E_{c,v} - E_n)/ \, m_B E_n\}^{1/2} \qquad (2.6)$$

and for odd f(z), and odd n:

$$\text{cotan} \, (m_W E_n L_z^2/ \, 2\hbar^2)^{1/2} = - \{ \, m_W(\Delta E_{c,v} - E_n)/ \, m_B E_n\}^{1/2} \qquad (2.7)$$

Figure 5 illustrates the bound states and wavefunctions in a QW. Evidently, the energy eigen values E_n of the particles confined to the quantum-wells may be determined from these equations if the following quantities are known for the considered material system: the

Γ-point effective masses, m^W(3D) and m^B(3D), of the particle in the well and barrier bulk materials, respectively, and the band-edge discontinuities $\Delta E_c = Q\Delta E_g$(3D) and $\Delta E_v = (1- Q)\Delta E_g$(3D), with ΔE_g(3D) $= E_g^B$(3D) - E_g^W(3D).

The conduction band, which exhibits Γ_6 symmetry, is made up of spherical s-orbitals [24,25]. This results in isotropy of this band in the zinc-blende crystal lattice. Therefore, the effective mass of the conduction electrons has the same value m_e for all directions in the crystal lattice. The principle valence bands, with Γ_8 symmetry, are made up of p-orbitals coupled with the spin to the total angular momentum J = 3/2 [24,25]. This results in anisotropy of these bands. The effective masses of the light-holes and heavy-holes are therefore different in different directions in the zincblende crystal lattice [26]. They may be expressed by applying the Luttinger parameters γ_1, γ_2, and γ_3 [27].

D. Gershoni et al. [28] have numerically calculated the energy levels of the confined carrier in the quantum well by finding the roots of the equation:

$$f(E) = [r_1(E) - 1/ r_1(E)] \sin r_2(E) - 2 \cos r_2(E) \tag{2.8}$$

$$\text{where } r_1(E) = k_W(E) m_B(E) / k_B(E) m_W(E) \tag{2.9}$$

$$\text{and} \quad r_2(E) = k_W(E) L_W \tag{2.10}$$
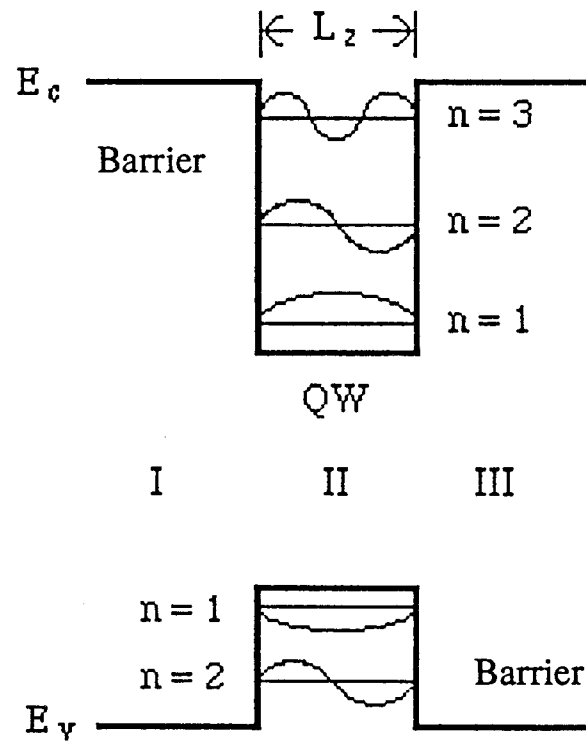
Figure 5.   Bound states and wavefunctions in a QW.

In the above equation L, k, m stand for the well-width, carrier wave vectors, and effective masses in the confinement direction, and the subscripts W and B stand for the well and the barrier, respectively.

The dispersion relations that correlate the wave vector to the particle energy E, measured from the bottom of the well are given by

$$E = \hbar^2 k_W^2 / 2 \, m_W \quad (E) \tag{2.11}$$

$$\text{and } E = V_B - \hbar^2 k_B^2 / 2 \, m_B \quad (E) \tag{2.12}$$

where V_B is the barrier potential or the band discontinuity.

2.5 2D excitons in quantum-well heterostructures:

Spatial localization of electrons and holes in a quantum-well causes a dramatic enhancement of excitonic effects [29]. Excitons dominate optical properties like absorption or luminescence of quantum-well heterostructures. Excitons are fundamental electronic excitations of semiconductor crystals. Excitons are the electron-hole pair formed by coulombic interaction. They occur when a single electron is transferred from one of the fully occupied valence bands into an unoccupied level in the conduction band. The transition of the valence band electron through the energy gap of the semiconductor into the conduction-band leaves an unoccupied energy state in the valence-band (hole, a particle with a positive charge). This description of the

electronic excitation was first discussed by Wannier, and are called as Wannier excitons.

Wannier excitons, from now on simply excitons, are usually generated in semiconductors through absorption of photons, accompanied by creation or destruction of lattice phonons. An ideal semiconductor crystal is transparent to light of photon energy less than the energy gap E_g. Therefore, the photon energy at which this crystal starts to absorb optical radiation is characteristic to the crystal, called as the fundamental absorption edge. Optical properties of crystals near the absorption edge are strongly influenced by the fact that the electron and the hole created in the excitation process interact with each other.

An exciton state is a two-particle state, which resembles a hydrogen atom, to which a characteristic Bohr radius and a binding energy may be assigned (Fig. 6). The quantum-mechanical wave-function associated with an exciton has the spherical symmetry of the s-orbital of the hydrogen atom, and a set of hydrogenlike quantum numbers (n, l,...) that characterize the relative motion of the electron and the hole to create an exciton.
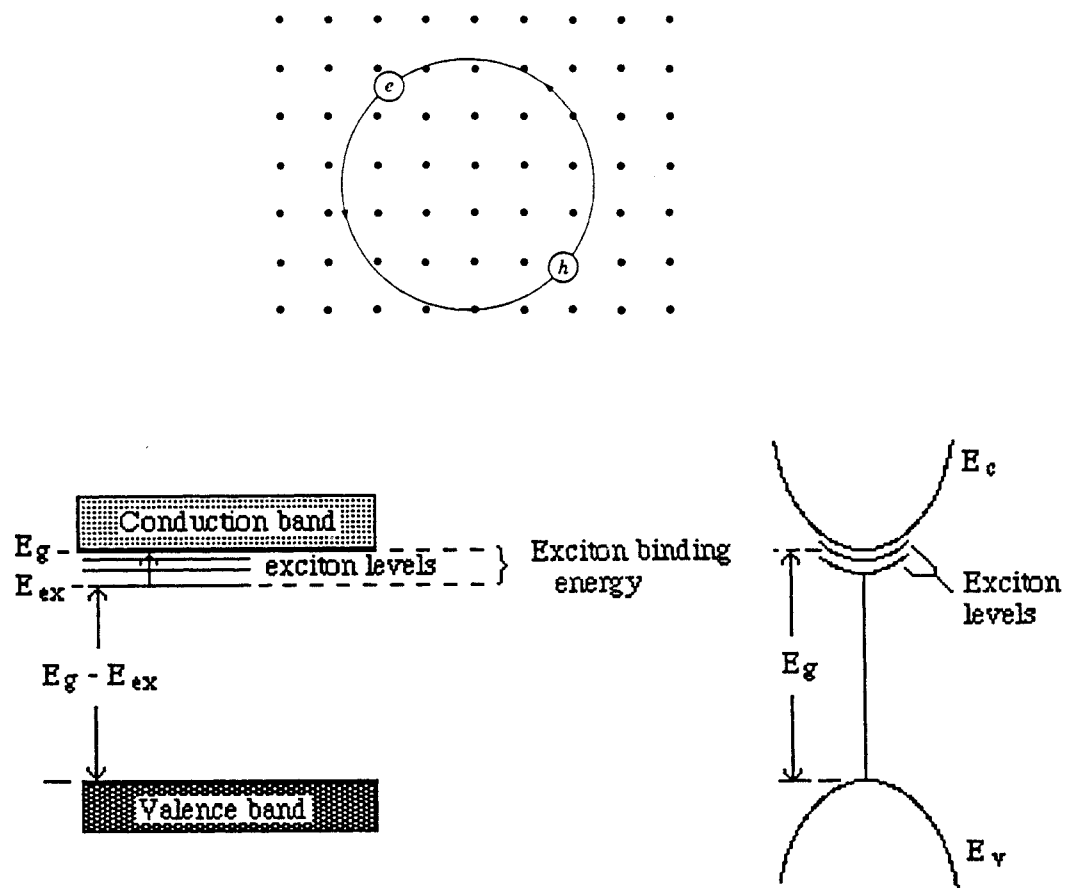
Figure 6. Energy level diagram for an exciton and its excited
-states, the exciton energy being referred to the
edge of the conduction band.

A short review of the theory of Wannier excitons in bulk semi-conductors can be found in Ref. 30. In quantum-well heterostructures, where carrier masses are very anisotropic, the confinement of an exciton to the well layer changes considerably the properties of this two-particle system. The anisotropy effects on excitonic properties have been theoretically analyzed by Grundmann and Bimberg [29].

2.6 Hole-energy levels:

The bulk hole bands are described in the Kane model by basis functions with angular momentum $J = 3/2$ symmetry. That means, four-fold degeneracy at $k= 0$ neglecting the spin-orbit split-off valence band. The dispersion near $k= 0$ can be described by Luttinger Hamiltonian as:

$$H = \hbar^2 / 2m_0 \; [\; (\gamma_1 + 5/2 \; \gamma_2) \; k^2 - 2\gamma_2(k_x^2 J_x^2 + k_y^2 J_y^2 + k_z^2 J_z^2)$$
$$- 4\gamma_3 \; (\{ \; k_x \cdot k_y \} \; \{ J_x \cdot J_y + \ldots \ldots \ldots \}) \;] \qquad (2.13)$$

where γ_1, γ_2, and γ_3 are the Luttinger parameters of the valence band.

In the bulk, propagation can be described in terms of heavy-hole and light-hole propagation in a given direction. Taking the z-axis as the quantization axis for the angular momentum, the direction of propagation of the hole, the levels $J_z = \pm 3/2$ and $J = \pm 1/2$ give a simple dispersion relation from Eqn. (2.13). Taking k_z in a [100]

direction, the kinetic energy of holes is

$$E = \hbar^2 k_z^2 / 2m_0 \, (\gamma_1 - 2\gamma_2) \quad \text{for} \quad J_z = \pm \, 3/2 \qquad (2.14)$$

$$= \hbar^2 k_z^2 / 2m_0 \, (\gamma_1 + 2\gamma_2) \quad \text{for} \quad J_z = \pm \, 1/2 \qquad (2.15)$$

From Eqns. (2.14 & 2.15), one can find the heavy-hole mass as:

$$m_h = m_0 / \, (\gamma_1 - 2\gamma_2) \qquad (2.16)$$

and light-hole mass as:

$$m_l = m_0 / \, (\gamma_1 + 2\gamma_2) \qquad (2.17)$$

In a successive perturbation approach, for hole levels in a quantum well, one first treats the quantum-well potential as a perturbation to the k= 0 unperturbed states, then adds the Luttinger interaction as a new perturbation to the quantum well levels. As a first perturbation, the quantum well potential lifts the degeneracy between the $J_z = \pm \, 3/2$ and 1/2 bands as they correspond to different masses. According to the Luttinger Eqn. (2.13), if we insert the values $k_x = k_\perp$, $k_y = k_z = 0$, the dispersion in a [100] direction perpendicular to z - direction is given by:

$$E = \hbar^2 k_\perp^2 / 2m_0 \, (\gamma_1 + \gamma_2) \quad \text{for} \quad J_z = \pm \, 3/2 \qquad (2.18)$$

and

$$E = \hbar^2 k_\perp^2 / 2m_0 \, (\gamma_1 - \gamma_2) \quad \text{for} \quad J_z = \pm \, 1/2 \qquad (2.19)$$

The transverse dispersion equation corresponding to $J_z = \pm 3/2$ (heavy-hole band along the z-direction) now has a light mass ($m_0/ (\gamma_1 + \gamma_2)$), whereas the $J_z = \pm 1/2$ has a heavy mass. The above procedure describes qualitatively the valence band effects. Figure 7 illustrates the hole dispersion curves. C. Weisbuch [31] has modified the **k. p** perturbation, which yields the dispersion along with the perturbation introduced by the quantum well. It is suggested that one has to diagonalize a perturbative Hamiltonian:

$$H = H_{\mathbf{k.p}} + H_{QW} \qquad (2.20)$$

in the degenerate set of valence-band levels at k= 0.

Besides energy quantization along the z-axis, the main property of quantum wells and thin structures is the bi-dimensionality in the density of states. As the motion along the z-direction is quantized an electron possesses only two degrees of freedom along the x and y directions.

2.7 Selection rules:

The quantum well and superlattice potentials are symmetric under space reflection changing from z into -z. Therefore, parity is a good quantum number; i.e., the envelope wavefunctions are characterized by their even or odd character under space reflection.
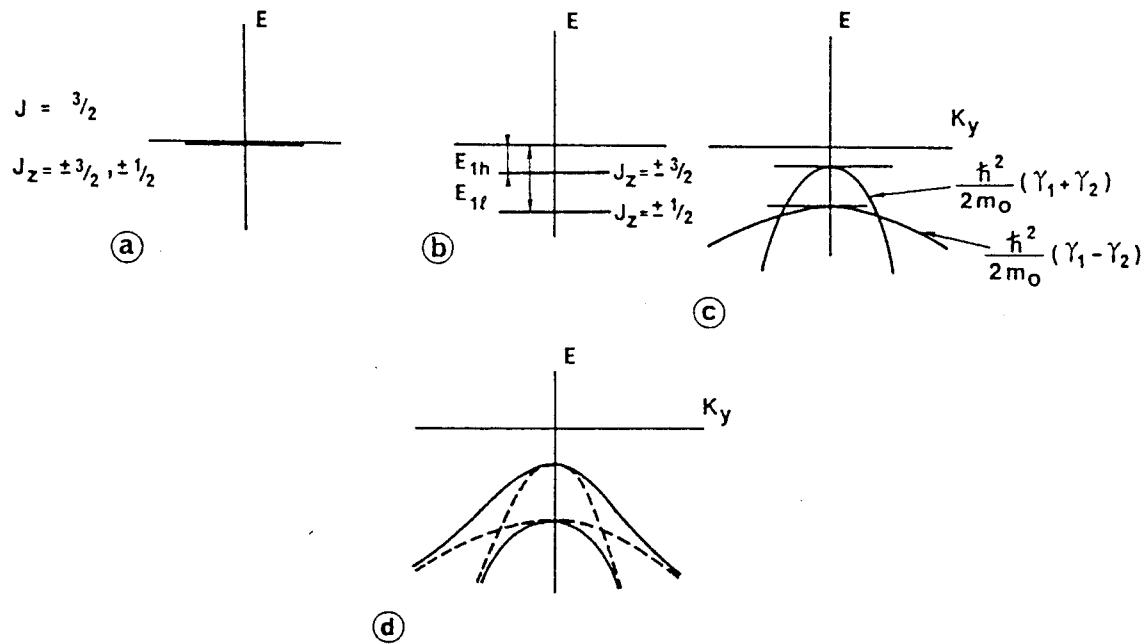
Figure 7.   Hole dispersion curve in a quantum well.

quantum-well potential lifts the 4-fold degeneracy of holes [in 3D, (a)] at $k = 0$. (b). The $\mathbf{k} \cdot \mathbf{p}$ interaction term as described by the Luttinger Hamiltonian then yields the dispersion in the y direction (for example) (c); finally, higher-order terms lead to an anticrossing behavior, (d).

The interband transition probability for particles confined in quantum wells can be calculated by perturbation theory and is the product of an optical matrix element times a density of states [31]. Considering the electric-dipole matrix element, the factorization procedure leads to the following results.

(1) The usual change of parity of electric-dipole transitions appears in the Bloch integral matrix element.

(2) Transitions are then allowed for confined states with the same envelope function symmetry under space reflection.

(3) In the infinite-well approximations, due to the orthogonality of the envelope wavefunction, only transitions between confined valence and conduction states with the same quantum number n are allowed ($\Delta n = 0$ rule).

Light polarization matrix elements can be calculated at $k = 0$, where the quantum-well potential acts as a simple perturbation to the Kane description of bands. The split-valence states retain their symmetry characterized by the angular momentum of the Bloch wavefunctions: the heavy-hole level at $k = 0$ has $J_z = \pm 3/2$; the light-hole level has $J_z = \pm 1/2$. The various allowed transitions can be calculated as the transitions between ground levels with $J = 3/2$, $J_z = \pm 3/2$ or $J_z = \pm 1/2$ and excited levels $J = 1/2$, $J_z = \pm 1/2$. Using classical

description of radiation emission, which states that an electric dipole radiates mainly perpendicular to its own motion and does not radiate in the parallel direction, the following selection rules can be deduced for light absorption or emission [32].

Light propagating perpendicular to the layers:

Only those dipole moments in the plane can absorb or radiate. Free electron-hole absorption is three times larger for the heavy-hole band (HH) than for the light-hole band (LH) transitions. Under circularly polarized light excitation 100% spin polarization occurs when electrons are only excited from one of the heavy-hole or the light-hole band.

Light propagating along the layers:

The heavy-hole transition can only occur with light polarization parallel to the layer (TE mode). The light-hole transitions occur for both TE and TM light polarizations. The relative intensities of the TE and TM modes are ratio 1: (2/3). Dingle reports that the TE mode luminescence to heavy-hole transition is larger than the TM emission.

Figure 8 shows the optical selection rules for absorption and luminescence between Bloch states of valence and conduction-bands.
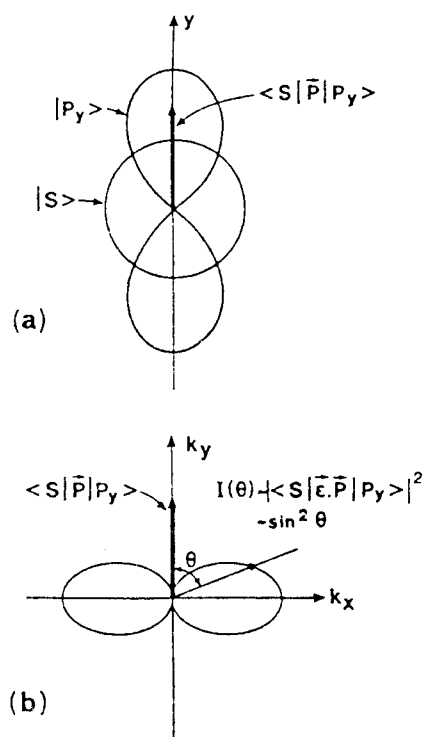
Figure 8 a. Optical selection rules for absorption and lumin-
escence between Bloch states of valence and
conduction bands: (a) diploe matrix element
(b) emission diagram of that dipole.

ELECTRON STATES

HEAVY-HOLE STATES   LIGHT-HOLE STATES

(c)

(d)

interface planes

light emission direction
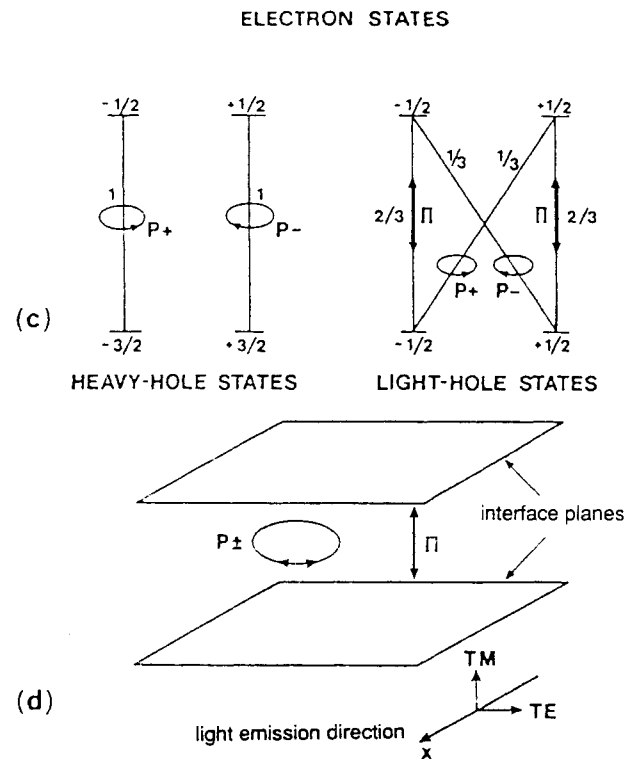
Figure 8 b.   Optical selection rules for absorption and luminescence between Bloch states of valence and conduction bands: (c) possible dipole moments (d) dipole moments in a QW situation [31].

2.8 Strain and strain effects:

In wide gap II-VI compound quantum-well heterostructures, the physical system has elastic strain (ε) due to lattice mis-match. H. Asai and K. Oe [33] have developed a procedure for theoretically calculating the strain in III-V semi-conductors. According to the procedure, the effect of elastic strain is such that, the energy shift of the heavy-hole valence-band ΔE_0 (1) and the energy shift of the light-hole valence-band ΔE_0 (2), respectively, is given by

$$\Delta E_0 \ (1) = [\ -2a \ (C_{11} - C_{12})/C_{11} + b(C_{11} + 2C_{12})/C_{11}] \ \varepsilon \qquad (2.21)$$

$$\text{and} \quad \Delta E_0 \ (2) = [\ -2a \ (C_{11} - C_{12})/C_{11} - b(C_{11} + 2C_{12})/C_{11}] \ \varepsilon \qquad (2.22)$$

where ε is the elastic strain, 'a' the hydrostatic deformation potential,'b' the shear deformation potential, and C_{ij} is the elastic stiffness constant of the material forming the heterostructure.

The elastic strain in the quantum-well is given by :

$$\varepsilon = \Delta a/a \ = \ [a \ (\text{barrier}) - a \ (QW) \ ] \ / \ a \ (QW) \qquad (2.23)$$

The strain ε is positive for compressive stress, produced by a biaxial stress parallel to [100] and [010]. Pikus and Bir [34] have developed a scheme to formulate the orbital strain Hamiltonian for the given bands at k = 0. Figure 9 shows the band diagram of a QW structure under biaxial strain.
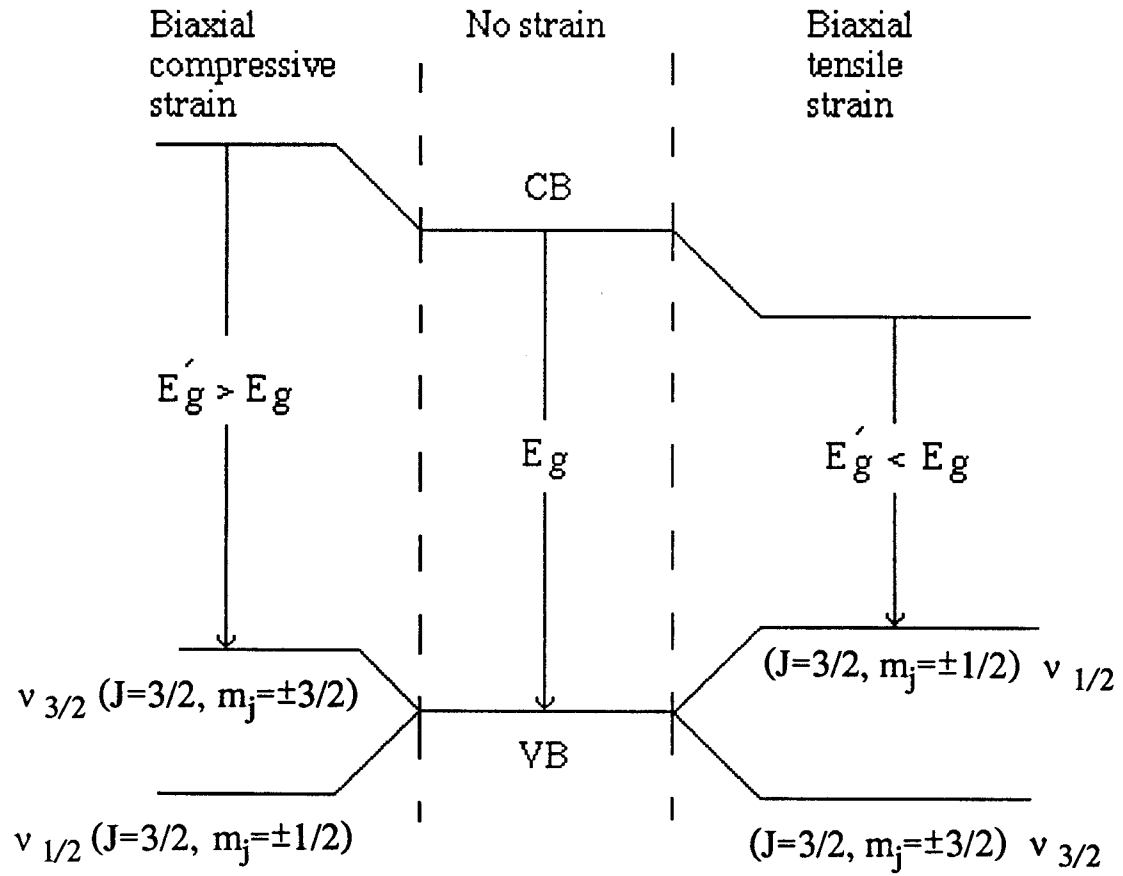
Figure 9. Schematic band diagram of a hetero-interface under biaxial strain at the zone center.

For a zinc-blende type material, the valence bands at k = 0 consist of a fourfold $P_{3/2}$ multiplet (J=3/2, m_j=± 3/2, ± 1/2 in spherical notation) and a twofold $P_{1/2}$ multiplet (J=1/2, m_j=± 1/2). The biaxial stress splits the $P_{3/2}$ multiplet, because of the hydrostatic stress component of the strain, shifts the 'center of gravity' of the $P_{3/2}$ multiplet. And also shifts the $P_{1/2}$ multiplet relative to the conduction band. The three valence bands as are labeled as V_1 (J=3/2, m_j=±3/2), V_2 (J=3/2, m_j=±1/2), and V_3 (J=1/2, m_j=±1/2) (Fig. 10). The transitions between the lowest conduction band and theses valence bands at k=0 are labeled as E_0 (1), E_0 (2), and (E_0 + Δ_0), heavy-hole, light-hole, and split-band, respectively.

With the above formulation of confined carrier transition with the energy shift due to strain, the energies for observable excitonic transitions from the heavy-hole band to the nth quantized subband is given by

$$E_{nH} = E_n + E_{zH} + E_{HH} \qquad (2.24)$$

where E_n is the allowed conduction band energy, E_{zH} is the strain shift of the QW heavy-hole band, and E_{HH} is the heavy-hole exciton
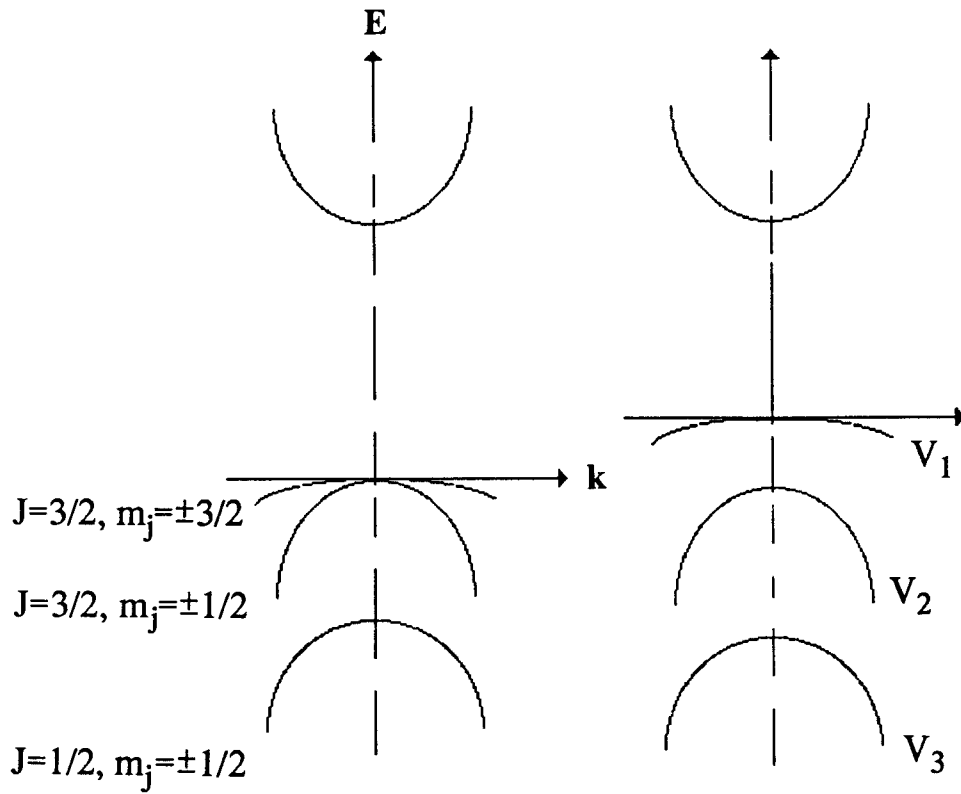
Figure 10. Schematic representation of the valence bands and the lowest conduction band: unstrained and strained due to biaxial compressive stress in zinc-blende type semiconductors at k=0.

binding energy. In the same manner, the energy of an excitonic transition from the light-hole band to the nth quantized subband is given by

$$E_{nL} = E_n + E_{zL} + E_{LH} \qquad (2.25)$$

where E_{zL} is the strain-induced shift of the QW light-hole band and E_{LH} is the light-hole exciton binding energy.

2.9 Luminescence:

The phenomena of luminescence, i.e., the emission of light by excited atoms, molecules, or condensed matter that occurs in excess to thermal radiation is caused by radiative transitions between energy levels of the excited species. Each feature of the luminescence spectrum of the physical system is connected with a definite electronic transition that originates on some excited electronic energy level, and after the emission of a photon (sometimes combined with generation of a phonon) terminates when the electron reaches a lower energy level. Depending on the way in which the excited levels become populated or becomes energetically excited, different luminescence processes may occur. If the physical system is excited by electromagnetic radiation (light), photoluminescence occurs, while electroluminescence is excited by applying an electric field (voltage) to the system.

In semiconductors, luminescence is caused by radiative recombination of excited individual or coupled charge carriers. These may be: (i) free electrons or holes occupying the energy levels in the conduction and valence bands, respectively, (ii) electrons or holes bound to ionized impurities, and (iii) excitons (electron-hole pairs

coupled by Coulomb interaction). Excitons may move throughout the crystal lattice of the semiconductor (free-exciton), or become localized by interaction with an active point defect of the lattice or on interfaces occurring in the semiconductor structure (bound excitons).

Luminescence spectroscopy has the advantage of the ability to differentiate between species involved in different recombination processes involved and can provide information on many types of centers in the crystal lattice. Luminescence techniques belong to the most sensitive, nondestructive methods of analyzing both intrinsic and extrinsic semiconductor properties. Luminescence spectroscopy, i.e., light emission versus wavelength observed under fixed optical or electron-beam excitation is commonly used to ascertain physical characteristics of quantum-well heterostructures.

Reihlen et al. [49] have calculated the photogeneration of carriers in the GaInAs/ InP quantum-well, and report that it is negligible as compared to that occurring in the InP barriers. They observed the quantum-well PL to be several orders stronger than the barrier PL in the 10 - 300 K temperature range. They explain the increase in PL intensity, due to the rapid and efficient transfer of photogenerated carriers from barriers into the quantum-well. The integrated quantum-well PL intensity decreased by two orders of magnitude as

the temperature was raised from 10 - 300 K, which they attribute to a decrease of the radiative quantum efficiency of the quantum-well.

Using a uniform absorption coefficient for the barrier at a particular excitation wavelength at a low temperature, one can find the percentage of the incident photons absorbed within the epitaxial barrier layers, during a PL experiment [75].

The quantum-wells give very strong PL, even though their absorption is negligible. That means, the photogenerated carriers in the barriers are efficiently transferred into the quantum-well, before recombination occurs. Reihlen [49] have developed a rate-equation model describing radiative and non-radiative recombination in the barriers and in the quantum-well, and transfer of carriers from the barriers into the quantum-well.

2.10 Composition dependence of the bandgap:

Hill [56] reports that the bowing of the energy-gap in semiconductor alloy results from the nonlinear dependence of the crystal potential on the properties of the component ions. The energy gap of an alloy A_xB_{1-x} in terms of the pure compound energy E_g (A) and

E_g (B) can be described as

$$E_g(x) = E_g \text{ (B)} + (E_g \text{ (A)} - E_g \text{ (B)} - b)x + bx^2 \qquad (2.26)$$

where ' b' is the bowing parameter.

The difference between the linear average

$$E_{g,AV} = xE_g \text{ (A)} + (1-x) E_g \text{ (B)} \qquad (2.27)$$

and $E_g(x)$ is $\delta E = E_{g,AV} - E_g(x) = x(1-x)b \qquad (2.28)$

According to Hill [56], the alloy MF_xG_{1-x} behaves as if the pseudo-anion $F_{0.5}G_{0.5}$ has a covalent radius equal to $1/2$ ($r_F + r_G$). The difference between the potential for the pseudo-anion and the average of the potentials of the F and G ions is:

$$V_b = Ze/ \ (8\pi\varepsilon_0) \ \{ \ (r_F - r_G)^2/ \ r_F r_G \ (r_F + r_G) \} \qquad (2.29)$$

where Z is the valence number of the intersubstitutional ions F and G, r_F and r_G are the scaled covalent radii of F and G ions (Paulings' constants), and 'e' is the electron charge. Assuming the reduction in energy δE in the energy-gap at x=0.5 is equal to the screened potential V_b, the bowing parameter can be written as:

$$b = Zer_{AV}/ \ 4\pi\varepsilon_0 \ \{ \ 1/r_F - 1/r_G \}^2 \exp \ (-sa \ \sqrt{3}/8) \qquad (2.30)$$

where $r_{AV} = 1/2$ ($r_F + r_G$), and 's' is the screening constant.

2.11 Temperature dependence of the bandgap:

The variation of the energy gap (E_g) of a semiconductor with temperature T is suggested by Varshni [35]:

$$E_g (T) = E_g (0) - \alpha T^2 / (T + \beta) \qquad (2.31)$$

where E_g is the energy gap which may be direct (E_{gd}) or indirect (E_{gid}), E_0 the value of energy gap at 0^0 K, and α and β are some constants.

Varshni reports that, most of the variation in energy gap with temperature is believed to arise from the following two mechanisms:

(1) a shift in the relative position of the conduction and valence bands due to the temperature-dependent dilation of the lattice. The effect is nonlinear in the low temperature range and linear at high temperatures.

(2) a shift in the relative position of the conduction and valence bands due to a temperature-dependent electron-lattice interaction.

The temperature dependence has the following form:

$$T \ll \theta$$

$$\Delta E_g \propto T^2 \qquad (2.32)$$

$$T \gg \theta$$

$$\Delta E_g \propto T \qquad\qquad (2.33)$$

where θ is the Debye temperature.

Due to fluctuations of the thickness of the $Zn_{1-x}Cd_xSe$ quantum well layer across the lateral direction, the effective bandgap of the QW is modulated in real space as shown in Figure 11. Generally, this modulation results in a broadening of the PL emission spectrum. In the low-temperature range, most of the free carriers occupy low-energy states according to the Fermi-Dirac distribution. As a result, the energy of the PL peak represents mainly the bandgap minima E_{1h}^{min} in the band modulation. When temperature is increased, more and more free carriers will occupy stationary higher-energy states and the PL emission peak broadens and shifts to higher-energy value.

Due to this thermal population of the higher-energy states with excited free carriers, at higher temperatures with QW luminescence more and more regions will originate where the modulated bandgap has its maximum value E_{1h}^{max}. As a consequence, the PL peak shifts to higher energies as compared to the minima of the modulated bands. In a rough estimate, this relative shift is in the order of kT. At the same time, as the PL peak shifts to higher energy values (with respect

High temperature

PL

CB

E_{1h}^{min} E_{1h}^{max} $\hbar\omega^{peak} \approx E_{1h}^{max}$

VB

ENERGY

Low temperature

PL

CB

E_{1h}^{min} E_{1h}^{max} $\hbar\omega^{peak} \approx E_{1h}^{min}$

VB

LATERAL DIRECTION ALONG THE LAYER
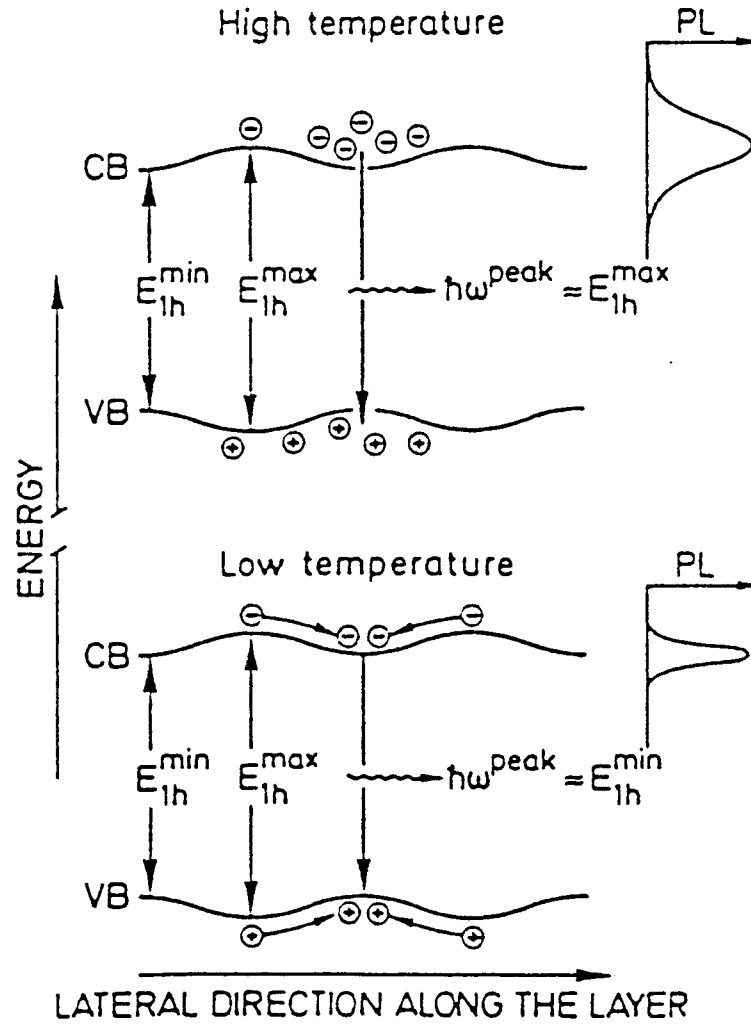
Figure 11. Schematic illustration of the real-space energy-band modulation due to lateral thickness fluctuations at low and high sample temperatures in $Zn_{1-x}Cd_xSe$ single QWs'.

to the band-edge minimum) the bandgap shifts to the lower energies due to the bandgap shrinkage when the temperature is increased. Thus the total change of the PL peak energy E_{1h} between 10 - 300 K is given by both effects: a blue shift of about kT ~ 25 meV due to thermal population of higher energy states and a red shift of about 100 meV (in bulk GaAs) due to the bandgap shrinkage.

Jiang et al. [48] have investigated the temperature dependence of GaAs quantum well structure and report that experimentally they observed 78 meV PL emission peak shift. Based on the above model, the PL emission peak shift should lie in the range of about 75 meV, which is in good agreement with the experimental results.

2.12 Linewidth of excitons in quantum wells as a function of temperature:

The main contribution to the linewidth of excitons is attributed to lattice interactions via polar optical phonons and to inhomogeneous fluctuations in the thickness of the well [36,37]. The studies of electron transport in a heterostructure suggests that these contributions are dominant at high temperatures [38].

Theoretically, one can calculate the linewidth broadening due to various scattering mechanisms. By the Fermi golden rule, the transition rate $W^{(j)}$ for various scattering mechanisms can be calculated if the unperturbed wavefunction of the quasi-particle is specified. The linewidth (HWHM) is then determined by $\Gamma_j = hW^{(j)}/2$ for various scattering mechanisms.

It is assumed that the electron-hole pairs generated by incident light are completely confined in the quantum well layer of thickness L in the z-direction, and are free to move along the well/ barrier interface, the ρ plane. The wavefunction of the exciton in the ground state may be approximated by [39]

$$\psi(\rho, z_e, z_h, R) = A\, e^{iK \cdot R}\, e^{-\beta\rho/2} \cos(\pi z_e/ L) \cos(\pi z_h/ L) \qquad (2.34)$$

where A is the normalization constant, K and R are the wave vector and polar vector of the center of mass of the exciton in the ρ' plane, ρ is the relative distance between electron and hole, β is a variational parameter, and z_e and z_h are the respective projections on the z-axis of the electron and hole positions.

The transition rate $W^{(j)}$ due to phonon-exciton interaction is given by Tait and Weiher [40] for acoustic and polar optical phonon

scattering, considering all phonon mechanisms to be inelastic. In acoustic phonon scattering, there are two types of scattering potentials: one involving piezoelectric and the other deformation mechanisms [38]. In polar optical phonon scattering, because the optical phonon energy, $\hbar \omega_0$ is larger than the binding energy of an exciton $E_{ex}(L)$, after a collision of an exciton with an optical phonon, the exciton is either totally ionized or the optical phonon energy is transformed into kinetic energy of the center of mass with elevation of the exciton to an excited state.

The calculation of scattering cross section of free excitons from impurities (neutral and ionized) in a quasi-two-dimensional system is extremely complicated, because of the quantum confinement of free carriers, the binding energy of an impurity depends on the thickness of the well layer and the location of the impurity [41]. J. Lee et al. [38] have invoked a phenomenological formula.

The transition rate $W^{(imp)}$ is proportional to the number N^+ of scattering centers N that are ionized,

$$W^{(imp)}(0) = CN^+ = W_0 \, e^{-<E_b>/k_B T} \tag{2.35}$$

where $<E_b>$ is the binding energy averaged over all possible locations

of the impurities. The parameter W_0 = CN is determined by fitting the experimental data.

The evaluation of total linewidth HWHM ($\Gamma_j = hW^{(j)}/2$) is obtained by combining the effects of all scattering mechanisms, and is given by:

$$\Gamma_{tot}^+ = \Gamma_0^+ + \Gamma_a T + \Gamma_{ph}/(e^{\hbar\omega_0/k_B T} - 1) + \Gamma_{imp}^+ e^{-<E_b>/k_B T} \qquad (2.36)$$

where the first term Γ_0^+ is the linewidth due to inhomogeneous fluctuations of the well width, and Γ_{imp}^+ is the linewidth due to the ionized impurity scattering. Γ_{ph} is the exciton- LO phonon coupling constant and $\hbar\omega_0$ is the LO phonon energy (30.81 meV in ZnSe). Γ_a is a coefficient of the exciton-acoustic phonon interaction, and $<E_b>$ is the binding energy of the donor averaged over all positions of the impurities within the well-layer. The second term represents the linewidth due to acoustic phonon scattering via deformation and piezoelectric potentials and the third term is due to optical phonon scattering.

J. Lee et al. have investigated the luminescence linewidth of excitons in GaAs/ $Al_xGa_{1-x}As$ multiple quantum well structure, and have used the above formulation to fit their experimental data. They mention that for both heavy-hole and light-hole excitons, the

theoretical model predicts the HWHM increases sublinearly in the low temperature range. They also report that, in the sample investigated, (i) at low temperatures acoustic phonon scattering is the dominant mechanism, (ii) when the temperature is larger than 20 - 25 K, ionized impurity scattering begins to make a significant contribution to the HWHM, and (iii) when the temperature T is higher than 200 K, polar optical phonon scattering becomes the dominant mechanism.

2.13 Raman Scattering :

The nearly backscattering geometry is frequently used [81]. Light propagates inside the sample along directions close to the normal to the plane of the quasi-2D system. It is often convenient to set $\theta + \phi = 90^0$. In this case the in-plane and normal components of the scattering wavevector are given by:

$$k = 2\pi/\lambda_L \{ \sin \theta - \cos \theta \} \qquad (2.37)$$

and $$k_z = (4\pi/\lambda_L)\eta(\lambda_L) \{ 1 - [1/2\eta(\lambda_L)]2 \} \qquad (2.38)$$

where λ_L is the incident laser wavelength and $\eta(\lambda_L)$ is the refractive index. The in-plane component k can be varied from a small value, at $\theta = 45^0$, up to maximum of $k \sim 10^5$ cm^{-1}. Larger values of k can be achieved with the more conventional backscattering geometry in which $\theta + \phi = 0^0$.

Raman scattering involves two photons - one in and one out-. In the Raman effect, a photon is scattered inelastically by the semiconductor crystal/ mixed-composition alloy with the creation (Stokes) or annihilation (anti-Stokes) of a phonon. The selection rule for the first-order Raman effect are :

$$\omega = \omega' \pm \Omega \text{ , and } k = k' \pm K \qquad (2.39)$$

where ω, k refer to incident photon, ω' and k' refer to the scattered photon. Ω and K refer to the phonon created or destroyed in the scattering event. In the second-order Raman effect, inelastic light scattering is accompanied by two phonons; creation of two phonons or the absorption of two phonons, or creation of one phonon and the absorption of one phonon. The phonons may have different frequencies. The selection rules in the second-order Raman effect are:

$$\omega = \omega' \pm \Omega \pm \Omega' \text{ , and } k = k' \pm K \pm K' + G \qquad (2.40)$$

where G is the reciprocal lattice vector. Figure 12 illustrates the Raman scattering process.

In the first-order Raman effect in the optical region it is not possible in terms of energy to have a reciprocal lattice vector because the photon wave vectors k, k' and their difference are much smaller
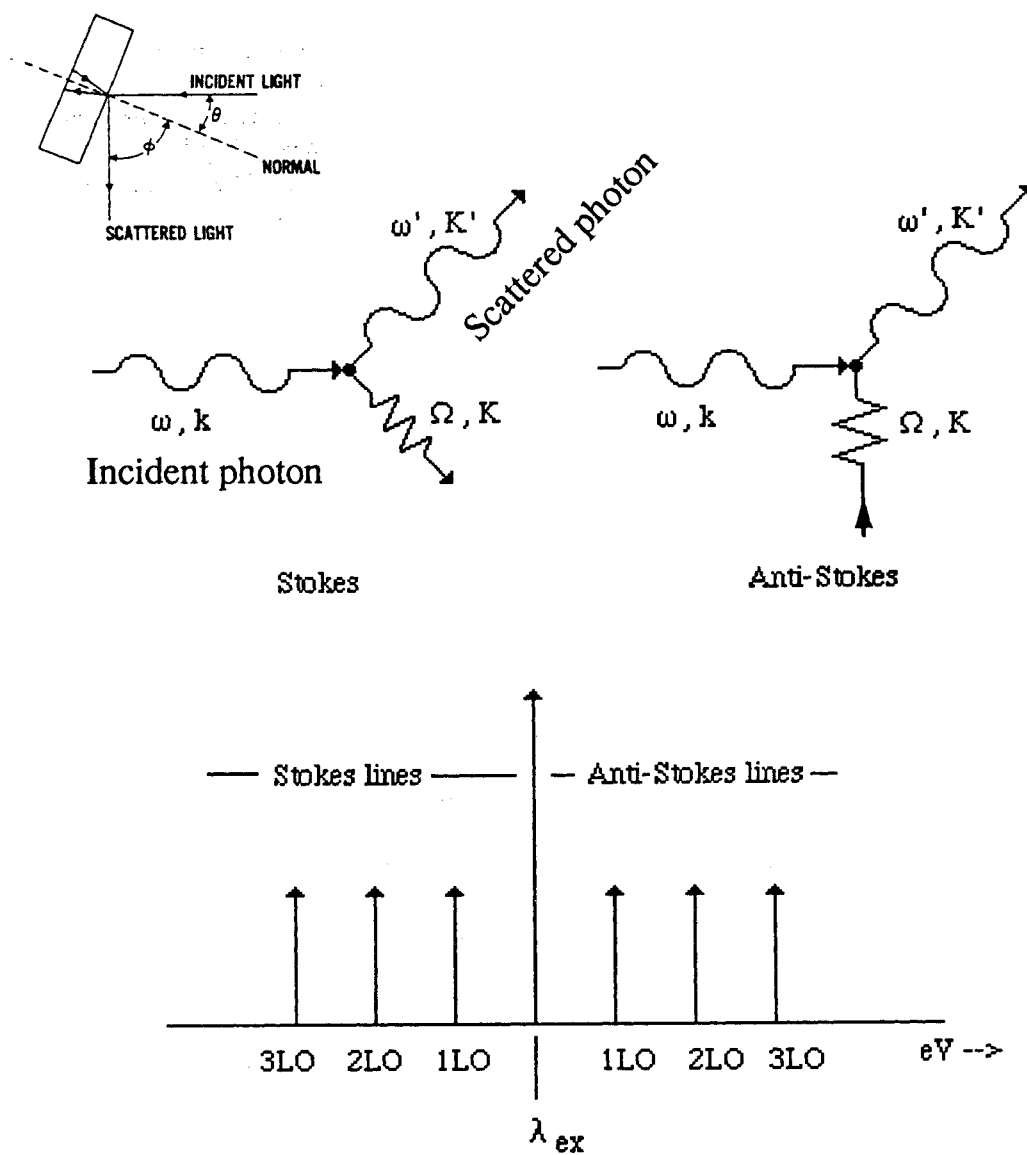
Figure 12. Representation of inelastic scattering and Raman lines with Stokes and Anti-stokes lines.

than the shortest reciprocal lattice vector G. On the contrary, in the second-order effect it is possible for the difference of the phonon wavevectors K, K' to be a reciprocal lattice vector.

When the energy of the exciting radiation approaches the edge of the interband absorption of crystals the cross section of Raman scattering is considerably enhanced. R. C. Miller et al. [52] have reported enhanced Raman scattering in square GaAs/ $Al_xGa_{1-x}As$ quantum wells when either the incident photon or scattered photon energy are resonant with the exciton transition in the well. They also report the first observation of resonant Raman scattering (RRS) with GaAs quantum wells where the incident and scattered photon energies are resonant with a 2D exciton transition. This type of LO phonon resonant Raman scattering is unique to quantum-wells where the exciton energies are tunable via the QW structure parameters.

2.14 Resonance Raman Scattering (RRS):

Excitons in multiple-quantum well (MQW) heterostructures are formed by electron-hole pairs confined in the well layers. For example, in GaAs - (AlGa)As heterostructure, excitons are confined in the GaAs layers. This reduction in dimensionality results in an enhancement of the exciton behavior. Optical properties of MQW's show several sharp

transitions that are characterized as excitons constructed from particle-in-a-well eigenstates [20, 42,43].

The QW potential and the degree of confinement of the exciton are affected by the choice of the material parameters, such as the width of the well and barrier layers. The width of the well insures both lower dimensionality and a sharp exciton. The width of the barrier determines the coupling between electron and hole states in adjacent wells. Zucker et al. [44] investigated GaAs- (AlGa)As sample consisting of 65 periods of 96Å GaAs and 98Å (AlGa)As using a tunable dye-laser. The Raman spectra obtained in resonance with the n= 1 and n= 2 excitons showed only the LO phonons of GaAs. For incident photon energies near the n= 3 and higher excitons, they also observed the LO phonons of (AlGa)As, evidencing the appreciable penetration of the barriers by theses excitons. In the energy range of the n= 1 heavy-hole exciton peak there is a correspondence between the excitation and Raman spectra. The resonant enhancement, in which the incident photon energy coincides with that of the exciton, is called the *incoming resonance*. A resonant behavior where the scattered photon energy equals that of the optical transition is termed as the *outgoing resonance* [92]. Observation of Raman scattering resonant with excitons in III-V compound quantum wells [45] and in II-VI compound (Cd,Hg)Te system [46] have been reported recently.

In most Raman scattering experiments the incoming and outgoing resonances cannot be separately resolved. Double resonances are expected only in the presence of sharp optical structure, and thus is a characteristic signature of exciton behavior. Double resonances are only possible when the laser frequency $\omega_L > \omega_1 + 2\,\Omega_{LO}$, where ω_L is the laser frequency, ω_1 the exciton energy and Ω_{LO} the LO-phonon frequency [45]. Figure 13 illustrates 2LO resonant Raman scattering process. Resonant Raman scattering (RRS) by phonons provides the link between electronic and lattice-dynamical properties. Raman scattering by LO phonons has been observed near electronic critical points in scattering configurations, which are forbidden according to dipole-selection rules [46].

2.15 Relation between elastic tensors of wurtzite and zinc-blende structure materials:

Martin [63] has derived a transformation which relates the fourth-rank elastic tensors of sphalerite (zinc-blende or ZB) and wurtzite (WZ) tetrahedrally coordinated compounds. The transformation permits a simple derivation of effective cubic constants from WZ compounds. Zinc-blende crystals are face-centered cubic (fcc with T_d symmetry) with two atoms per primitive cell, where as WZ crystals are
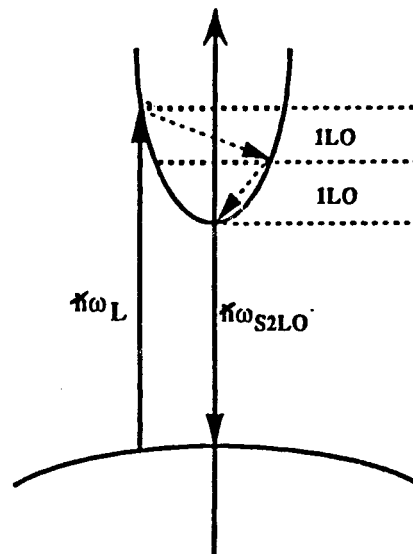
Figure 13. Schematic representation of resonant Raman scattering.

hexagonal (with C_{6v} symmetry) with four atoms per cell. The fundamental relation between ZB and WZ structures is that the local environment of any atom in either ZB or WZ is exactly the same through the second neighbor. The two lattices differ only in the arrangement of third and more distant neighbors. The procedure involves simple rotations which apply to tensorial property. Table II presents the effective cubic constants of wurtzite crystals [63]. The bulk modulus is given by $B = 1/3 \, (C_{11} + 2C_{12})$ and shear constant $C_s = 1/2 \, (C_{11} - C_{12})$, where C_{11} and C_{12} are the elastic stiffness constants of the material. From Table II taking the values for effective modulus B and C_s, one has to solve for the elastic constant C_{ij} in ZB form.

2.16 Exciton complexes:

Recombination radiation from silicon crystals containing one of the Group III or V elements as an added impurity, show extremely sharp lines at low temperatures under high-resolution spectroscopic measurements. These lines are interpreted as the radiation produced by the recombination of an electron and a hole both of which are bound in an immobile four-particle complex consisting of an impurity ion and three electronic particles. J. R. Haynes [80] report that the ratio of the integrated intensity in the sharp lines to that of the intensity of principal exciton line are found to be proportional to the

TABLE II

Effective cubic constants for wurtzite crystals

Units are 10^{11} dyn/cm^2

Material	B^{eff}	C_s^{eff}	C_{44}^{eff}
SiO	22.06	11.90	25.15
BeO	22.52	11.69	19.96
ZnO	14.33	4.55	5.49
CdS	6.11	1.26	2.41
CdSe	5.31	1.02	2.23

amount of impurity added. Earlier investigations on impure semiconductor materials have shown the existence of exciton recombination and donor-acceptor recombination with LO phonon replicas [82]. Bogardus et al. [83] investigated the exciton complexes in pure GaAs doped with one type of shallow acceptor and one type of shallow donor, e.g., Si; observed several sharp emission peaks in the photoluminescence spectra. They attribute the major emission lines due to excitons: either free excitons, excitons trapped on neutral or ionized impurities, or excitons trapped on impurity pairs (donor-acceptor recombination). The less intense lines are due to phonon replicas and emission from excited states of excitons. Sharma and Rodriguez [84] have calculated the binding energies of excitons bound to neutral donors, for the particular case of GaAs. They assumed an effective mass ratio of $\sigma = m_e / m_h = 0.15$ and predicted a binding energy for an exciton X trapped on an ionized donor D^+, of $E_{XD^+} = 1.06 \, E_D$, where E_D is the binding energy of the isolated donor D^0. For an exciton trapped on an ionized acceptor A-, they find $E_{XA^-} = 1.4 \, E_A$. The binding energy for excitons bound to neutral impurities is usually expressed in terms of the dissociation energy D_0, i.e., the energy required to separate the complex into a neutral impurity and a free exciton. For a exciton bound to neutral donors D^0, Sharma and Rodriguez calculate a dissociation energy of $D_0 = 0.13 \, E_D$, giving a

binding energy of $E_{XD^0} = E_X + 0.13 \; E_D$. Here E_X is the binding energy of the free exciton. According to Hopfield [85], the binding energy of exciton-neutral acceptor complex is $E_{XA^0} = E_X + 0.07 \; E_A$ for GaAs. Combining the results of Hopfield and Sharma, one can estimate the photon emission energy $\hbar\omega$ of radiative annihilation of the exciton complexes (D^0,X), (D^+,X), (A^0,X), and (A^-,X) as [83]:

$$\hbar\omega(X_{D^0}) = E_g - E_X - 0.13 \; E_D \qquad (2.41)$$

$$\hbar\omega(X_{D^+}) = E_g - E_D - 0.06 \; E_D \qquad (2.42)$$

$$\hbar\omega(X_{A^0}) = E_g - E_X - 0.07 \; E_A \qquad (2.43)$$

$$\hbar\omega(X_{A^-}) = E_g - E_A - 0.40 \; E_A \qquad (2.44)$$

From effective mass approximation based on hydrogenic model, E_X can be found and the ratio $\sigma = m_e/m_h$ can be assumed for the particular semiconductor of interest. The binding energy of the donor $E_D = (1 - \sigma) \; E_X$ and the binding energy of the acceptor $E_A = E_D/\sigma$ is calculated.

2.17 Circular Polarization:

When the electrons are excited with circularly polarized light from the valence band, the electron spins are optically oriented and this manifests itself in a circular polarization of the recombination

[86,87]. Upon excitation by the circularly polarized light, owing to the symmetry properties of the wavefunctions and the connection between angular momentum and the momentum, a preferred-direction along the momentum of the produced holes, is created in the valence band, with a symmetry axis that coincides with the direction of the light beam [88]. The circular polarization phenomena are determined by the relative strengths (3 and 1), the m_j values ($\pm 3/2$ and $\pm 1/2$), and the effective hole masses ($m_h^*=0.45m_0$ and $m_l^*=0.088m_0$ for the heavy and light holes, respectively in a GaAs system). Since the electron states are $m_j = \pm 1/2$, the resonant absorption of $\sigma+$ ($\Delta m_j = +1$) polarized light by heavy and light hole transitions, will generate electrons with $m_j= -1/2$ and $+1/2$, respectively. With $m_h^* > m_l^*$, the emission at low temperatures will be via the heavy-hole ground state [89]. Thus assuming a spin relaxed hole population and incomplete electron spin-relaxation, resonant excitation of the lowest energy heavy or light hole exciton transitions lead to the emission from the ground-state heavy-hole exciton polarized $\sigma+$ and $\sigma-$, respectively. At higher temperatures where the lowest light-hole level is thermally populated, the above resonant excitation conditions give rise to emission from the ground-state light-hole exciton with polarization $\sigma-$ and $\sigma+$, respectively. As there is always some relaxation of the electron spins, the luminescence will

not be 100% polarized. A decreased or negative polarization, i.e., a polarization opposite to the incident polarization, is the significant features of light-hole transitions for excitation, with detection set at the heavy-hole emission which is the usual way of obtaining an excitation spectrum. For nonresonant excitation, at low temperatures σ+ emission dominates, since the heavy-hole transitions are three times stronger than the light-hole transitions. Thus circular polarization techniques are very useful in identifying transitions. Figure 14 illustrates the selection rules for absorption and emission transitions for GaAs type quantum wells, under circular polarized light.
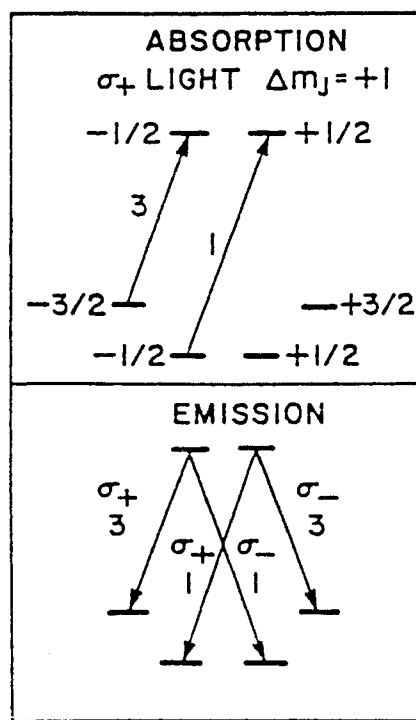
Figure 14. Selection rules for absorption and emission under circularly polarized excitation [89].

CHAPTER 3

EXPERIMENTAL TECHNIQUES
AND
THE PHOTOLUMINESCENCE SPECTRA

Luminescence spectroscopy, that is, the light emission over a range of wavelengths observed under optical excitation (named as photoluminescence (PL)), is commonly used to ascertain physical characteristics of quantum-well heterostructures. Each feature on the luminescence spectrum of the physical system is connected with a definite electronic transition which originates on some excited electronic energy level, and after the emission of a photon terminates when the electron reaches a lower energy level.

In this chapter, the investigated MBE grown quantum-well sample is described. Description of the techniques and state-of-the-art equipment used during measurement of luminescence (recording), features observed in low temperature PL spectra, measurement of PL in 8.7 - 120 K temperature range along with some analysis of experimental results are presented.

3.1   Single quantum well (SQW) sample

In the bulk, single crystals of the alloy $Zn_{1-x}Cd_xSe$ has the zinc-blende structure for x <0.3, the hexagonal wurtzite structure for x> 0.5, and mixed phases for 0.3 <x <0.5 [47]. When grown in bulk, CdSe has the hexagonal wurtzite structure. Samarth et al. [65,66] have successfully grown a single-crystal zinc-blende phase of CdSe on (100) oriented GaAs by molecular beam epitaxy (MBE), despite the large lattice mismatch (~7%) between epilayer and the substrate. The hetero-epitaxy of $Zn_{1-x}Cd_xSe$ on (100) GaAs by MBE results in single-phase zinc-blende crystals over the entire composition range from CdSe to ZnSe.

The investigated $Zn_{1-x}Cd_xSe$ quantum wells (QWs) were grown by MBE on a ZnSe 0.7 µm buffer layer, grown on (100) oriented semi-insulating Cr-doped GaAs substrate. The single quantum well samples have 60Å, 90Å, and 120Å wide $Zn_{0.86}Cd_{0.14}Se$ wells, clad on the top by a 0.1 µm thick ZnSe layer (Fig. 15). The QWs were grown at around 250 degree centigrade and the sample surfaces were monitored by reflection high-energy electron diffraction (RHEED). The details of crystal growth are published elsewhere [65,66]. The heterostructure adapts the zinc blende (ZB) crystallographic form of the substrate. The quantum layer thicknesses were determined by transmission electron microscopy (TEM) and the reflectance spectroscopy method [65,66].

ZnSe   Zn $_{0.86}$ Cd $_{0.14}$ Se   ZnSe

$\} \Delta E_c$

GaAs Substrate

E $_g$ = 2.821 eV
(at 9 K)

$\} \Delta E_v$

L $_w$

Lw = 60 Å, 90Å and 120Å
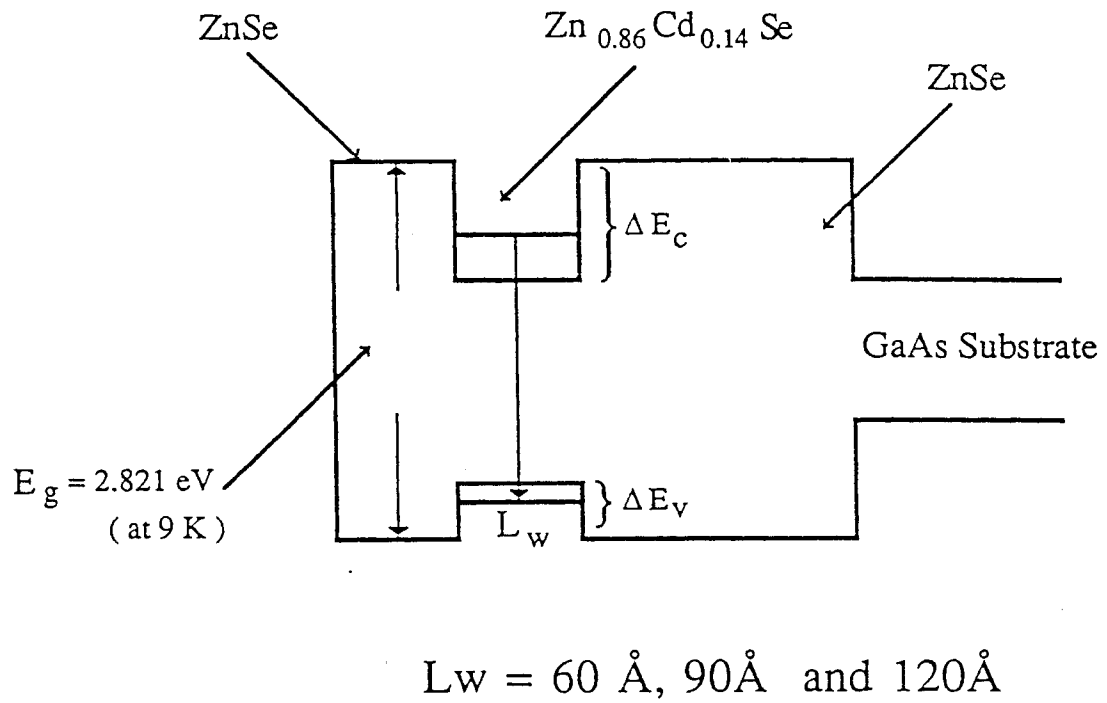
Figure 15.   Investigated single quantum-well structure.

3.2 Experimental setup and Measurement techniques

3.2.1 Setup for Photoluminescence (PL) Spectra

The optical spectra are measured in the backscattering direction at 26^0 from the normal to the quantum well layer, with the sample mounted on a cold finger cooled by a closed cycle helium cryostat down to 8.5 K. The photo-luminescence measurements are performed with an argon ion laser (Fig. 16) for the intrinsic excitation (ZnSe - barrier) using the 351.1-363.8 nm (UV) lines or the 365 nm Hg line from a 100W high pressure Hg lamp (PTI model A1010). The 457.9 nm line from an argon ion laser directly excites the $Zn_{0.86}Cd_{0.14}Se$ quantum well (extrinsic excitation), because the ZnSe cladding layer is transparent for the 457.9 nm line.

Luminescence spectra are recorded with a Jarell-Ash 0.75 m monochromator equipped with a 1180 grooves/ mm grating. The detection electronics has a thermo-electrically cooled photomultiplier (Hamamatsu R928) with a fast preamplifier (ORTEC 474). Signals from the pre-amplifier are fed to the time-correlated-single photon-counting (TCSPC) system or to a gated photon counting apparatus (SR400) both controlled by a computer that also controls the stepping
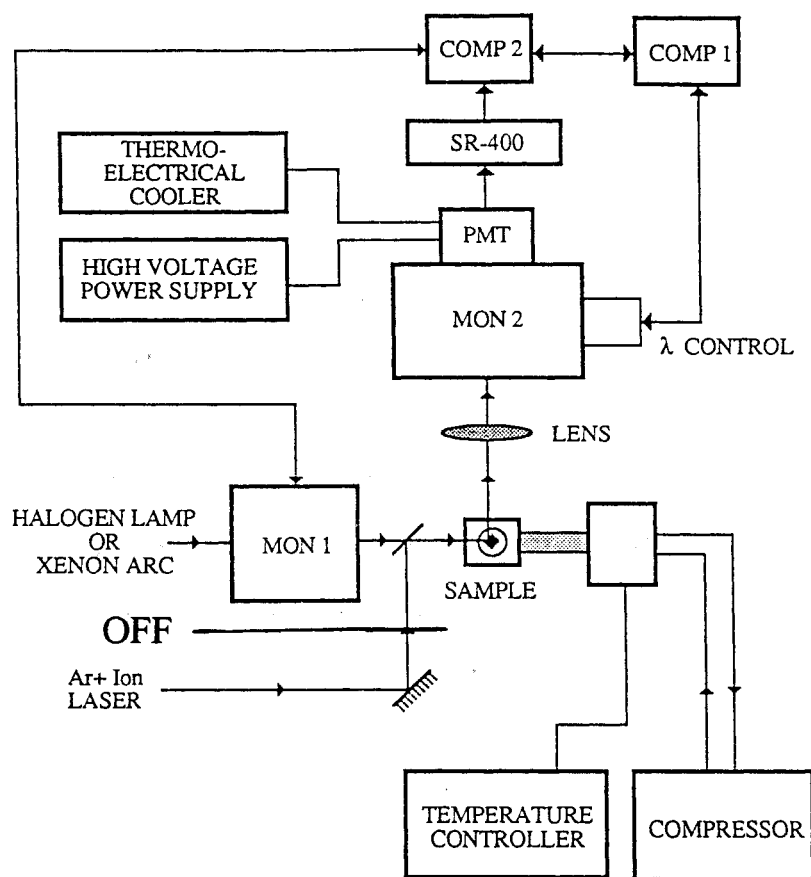
Figure 16. Photoluminescence measurement setup

motor scanning of the Jarell-Ash monochromator. The photomultiplier (PMT) detector used has a rather flat response within the emission range of the $Zn_{0.86}Cd_{0.14}Se$ luminescence. All the spectra are stored in the computer for further processing.

3.2.2 Setup for Photoluminescence excitation (PLE) spectra

For quantum wells, higher energy features that are not seen in standard photoluminescence spectra can be observed in excitation luminescence spectra, since the quantized quantum well states exhibit resonant absorption. If one excites the sample with a tunable excitation source (by scanning the wavelength of excitation) and observes the PL emission at a fixed wavelength, one measures the photoluminescence excitation spectrum (PLE). The instrument setup is similar to the PL measurement setup as shown, except for using a tunable excitation source. The detection wavelength is set to the sample emission peak wavelength and the 100 W tungsten halogen lamp used as the excitation source, is scanned over 400 nm through the wavelengths close to the detection wavelength (Fig. 17).
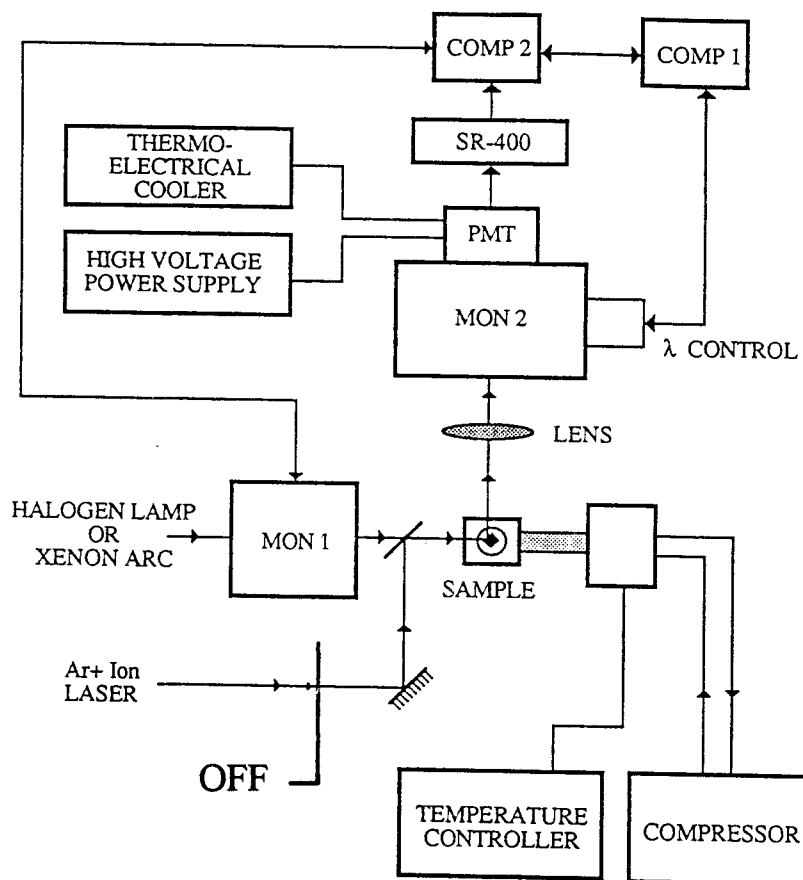
Figure 17. Photoluminescence excitation measurement setup.

3.2.3 Set up for Circular Polarization (CPL) spectra:

Figure 18 gives the block diagram of the experimental setup. The light from the argon-ion laser is linearly polarized by the Glan calcite polarizer P1, and a 90^0 retarder to produce the circular polarized light. The $\sigma+$ and $\sigma-$ polarization is achieved by rotating the linear polarizer by 45^0 clockwise or counter-clockwise. The acceptance angle of excitation is controlled by a diaphragm. By means of lenses the light is focussed on the sample S, mounted in a cryostat.

The degree of polarization of light is analyzed by the photo-elastic modulator (PEM) and the polarizer P2. Because of the large acceptance angle used during measurements, usually a sheet polarizer is used for P2. Emitted light from the sample is dispersed by a 0.75 M Jarrell-Ash monochromator and detected by the R928 (Hamamtsu) photomultiplier. The modulator is driven by the voltage V_M (Fig. 18) at a frequency f=50 KHz gives rise to a retardation that changes rapidly within the modulation cycle. If the maximum retardation is 900, then alternating with 50 KHz the left- and right-circularly polarized components of the luminescence are detected. Within a modulation cycle the retardation is best defined in the intervals 'a' and 'b' that are centered around the peak values of V_M as shown in Figure 18. A dual-channel photon counter
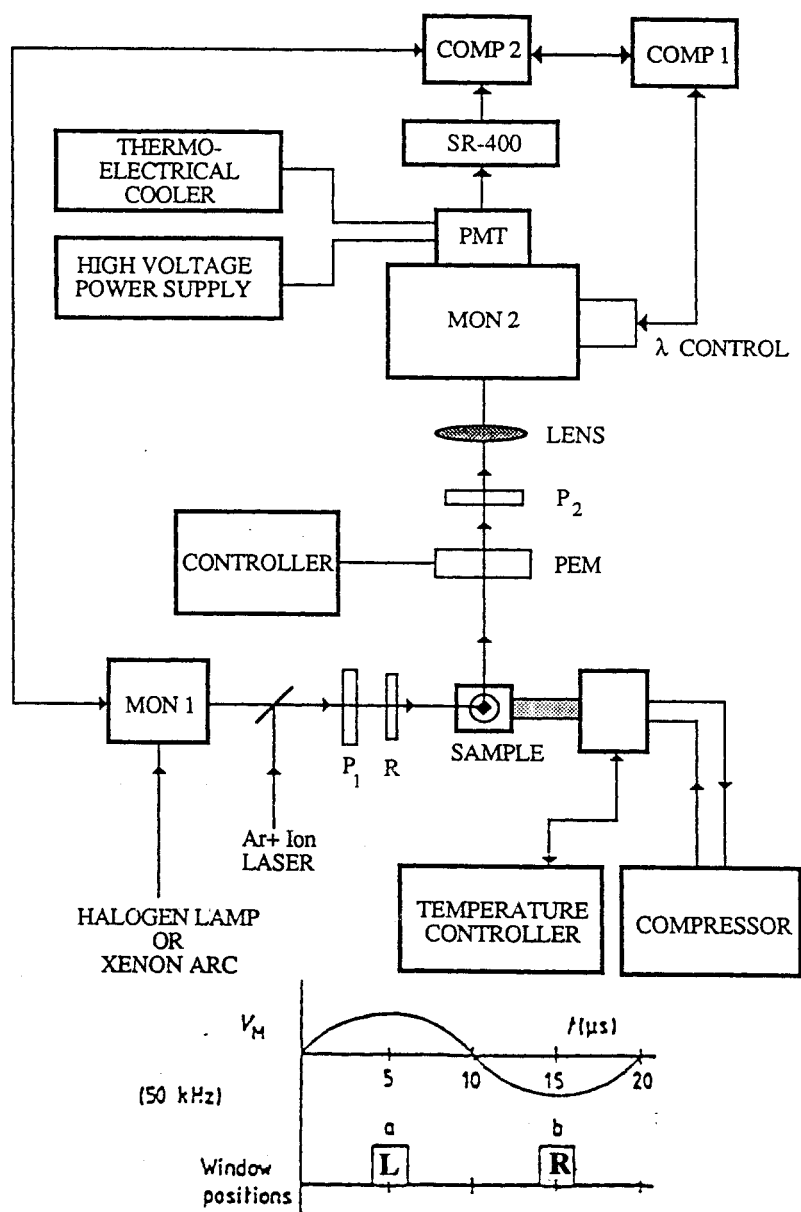
Figure 18. Circular polarization measurement setup and the
position of time windows (intervals 'a' and 'b')
of right and left detection counters.

(SR400) is used to simultaneously record both right- and left circularly polarized emission intensities. The number of photons detected by the photomultiplier in the interval 'b' (I_b) originate from the right-circularly polarized intensity and the number of photons detected in the interval 'a' (I_a) originate from the left-circularly polarized intensity. The degree of circular polarization is then computed as the ratio of sum and difference of two polarized intensities is given by :

$$D_{CPL} = (I_a - I_b) / (I_a + I_b).$$

3.3 The Photoluminescence spectra of the single quantum well

The photoluminescence spectra of $Zn_{1-x}Cd_xSe$ single quantum-well samples were recorded under direct excitation by an Argon laser 2.707 eV laser line, and under indirect excitation by UV lines of Argon laser (3.407 - 3.53 eV) as well as 3.396 eV line from a Hg- lamp. Our investigation was aimed to study the photoluminescence (PL) emission intensity, peak wavelength and the linewidth (FWHM) in $Zn_{1-x}Cd_xSe$ single quantum wells of different well width.

What we mean by direct and indirect excitation of the QW in this study is, the ZnSe barrier has the bandgap E_g = 2.821 eV at 8.7 K and the single quantum-well of $Zn_{1-x}Cd_xSe$ for the composition x = 0.14,

has the bandgap E_g = 2.6355 eV. If the excitation energy is above the bandgap of $Zn_{1-x}Cd_xSe$ single quantum-well and below the ZnSe barrier bandgap (2.6355 < E_{ex} < 2.821 eV), it is the <u>direct excitation</u> of the QW. If the excitation energy is greater than the bandgap of the ZnSe barrier, then it is referred to as the <u>indirect excitation</u> of the QW (E_{ex} > 2.821 eV).

The photoluminescence spectra shown in Figure 19 and Figure 24 are due to radiative transitions in $Zn_{1-x}Cd_xSe$ well for three of the $Zn_{1-x}Cd_xSe/ZnSe$ single quantum-well samples (PL intensity normalized to unity), with well widths of 60Å, 90Å and 120Å respectively. The spectra in Figure 19 were measured at 8.7K, using UV lines (3.407 eV-3.53 eV) from an argon ion laser. It distinctively features two emission bands. The emission bands show a clear shift to lower energies (2.6604 eV -> 2.6405 eV) and become narrower (8.02 meV -> 3.377 meV) as the well width is increased [78,79]. The higher energy peak is ascribed to the free exciton, and the lower energy peak to the bound exciton transitions. Figure 20 shows the PL spectrum of the highest-quality single quantum-well with well-thickness 90 Å (SQW-5), with its deconvolution into two emission bands. Figure 21 shows the PL spectrum of the single quantum-well with well-thickness 60 Å (SQW-4), with its deconvolution into two emission bands.
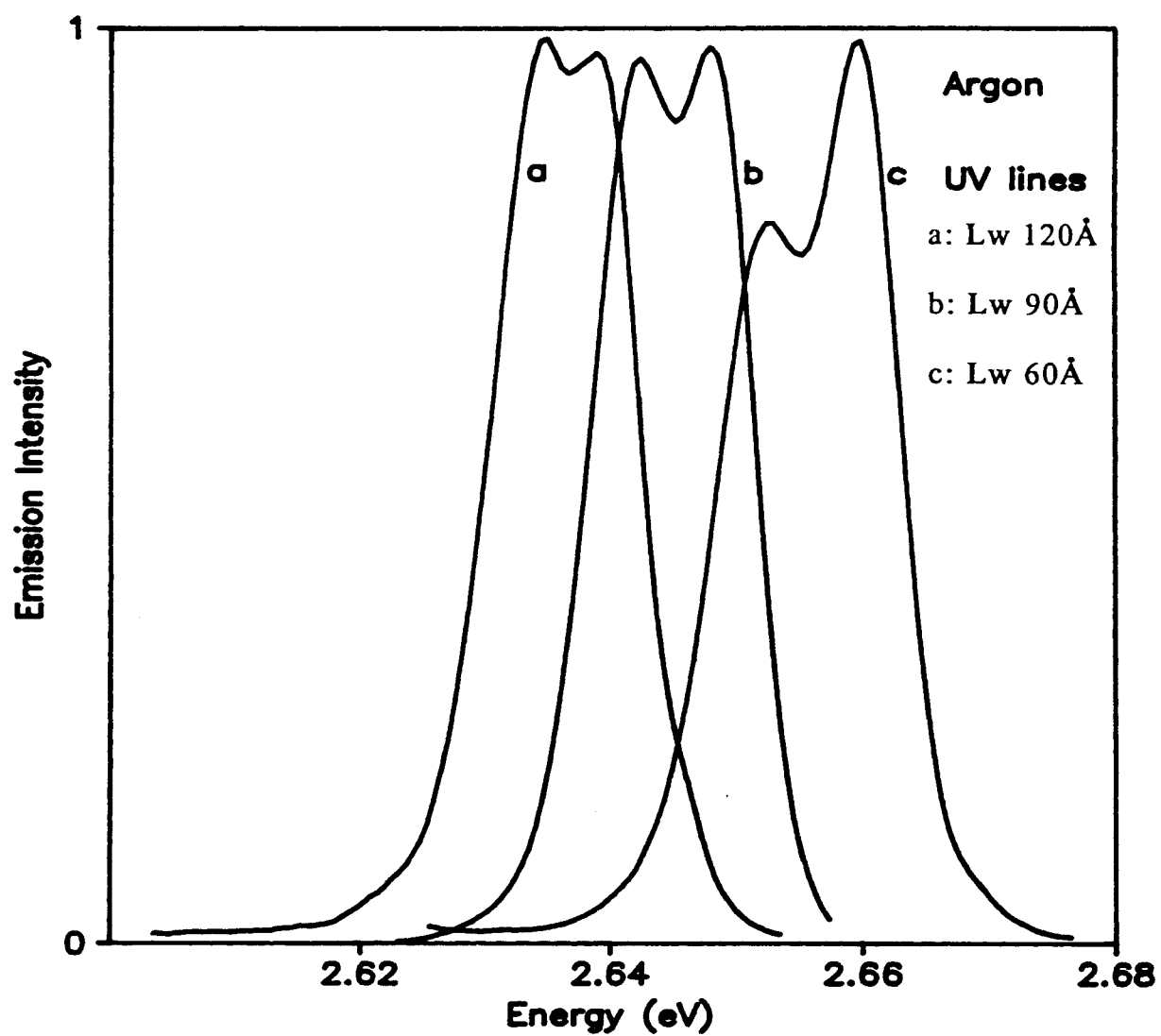
Figure 19.   PL of single quantum-wells by argon UV lines

SQW−5 (Lz 90A)
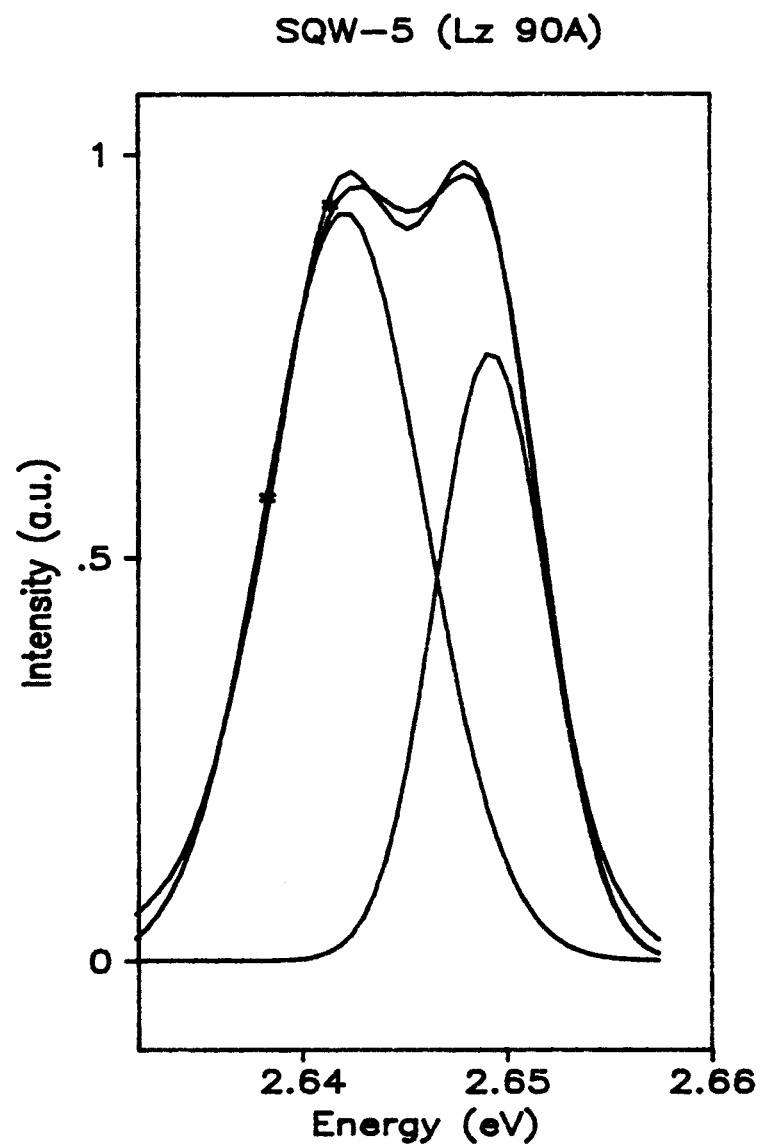
Figure 20. SQW-5 PL by argon UV lines and its deconvolution into two emission bands.
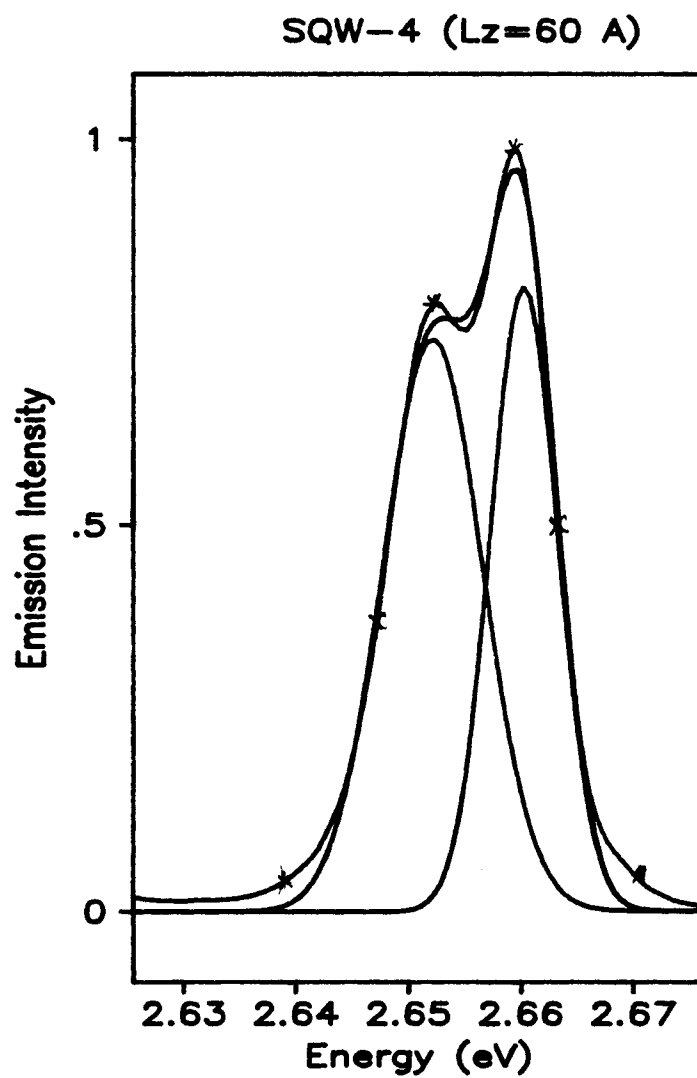
Figure 21. SQW-4 PL by argon UV lines and its deconvolution into two emission bands.

Figure 22 shows the PL spectrum of SQW-5 by the mercury line 3.396 eV, and its deconvolution into two emission bands. Under mercury line (3.396 eV) excitation, the free exciton peak (high energy peak) shows higher intensity than the bound exciton (low energy peak). The 3.407 eV - 3.53 eV argon UV laser lines, and mercury 3.396 eV lines are strongly absorbed in the ZnSe barrier layers. If we assume an absorption coefficient of 1×10^5 cm^{-1} for ZnSe (E_g = 2.821 eV at 8.7K), 95% of the excitation photons are absorbed within 300 nm of the barrier layers (100 nm ZnSe cladding barrier and 200 nm of the barrier buffer layer of 700 nm total thickness). Figure 23 shows the comparison between argon UV lines and Hg-lamp excitation of SQW-5, featuring less intense bound-exciton intensity by the Hg-lamp. Table III lists the results of the PL spectra under direct and indirect excitation with deconvolution into two and three emission bands in sample SQW-5.

The excitation process will be predominantly indirect, being limited by diffusion of the photo-generated free carriers from the ZnSe barriers into the $Zn_{0.86}Cd_{0.14}Se$ quantum well [48,49]. Indirect excitation of the quantum well gives very strong emission, and the photo-generated carriers in the barriers are efficiently transferred into the $Zn_{0.86}Cd_{0.14}Se$ well before recombination occurs.

SQW—5 (Lz 90A)
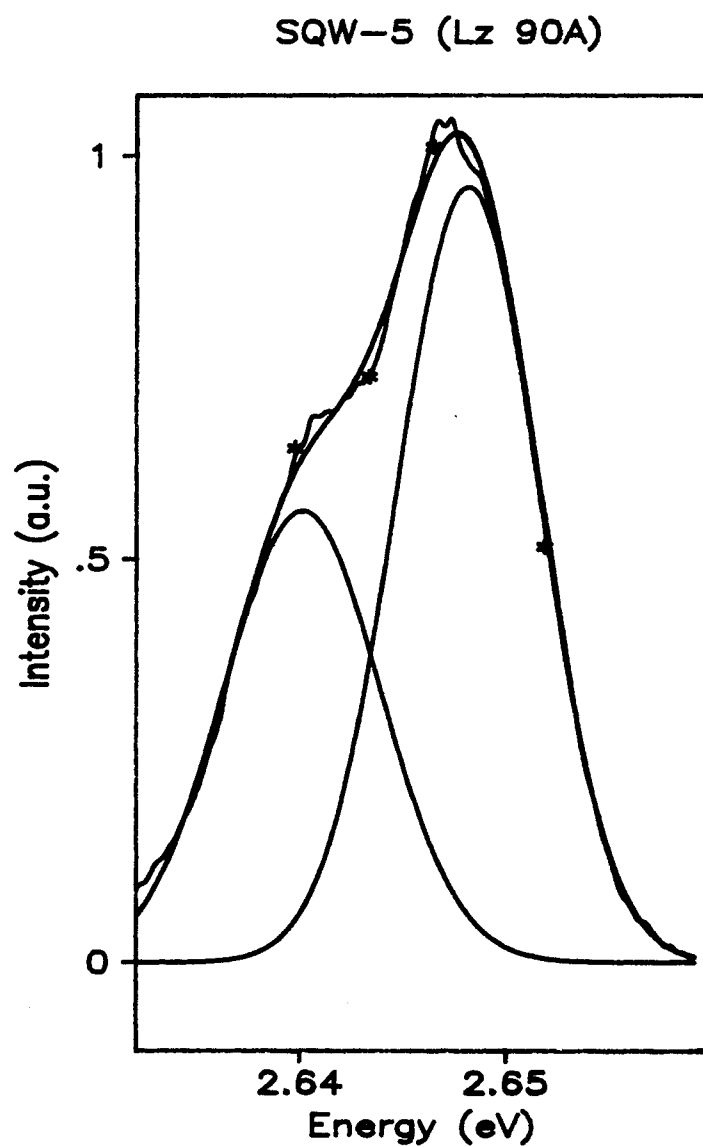
Figure 22. SQW-5 PL under Hg-lamp excitation and deconvolution into two emission bands.
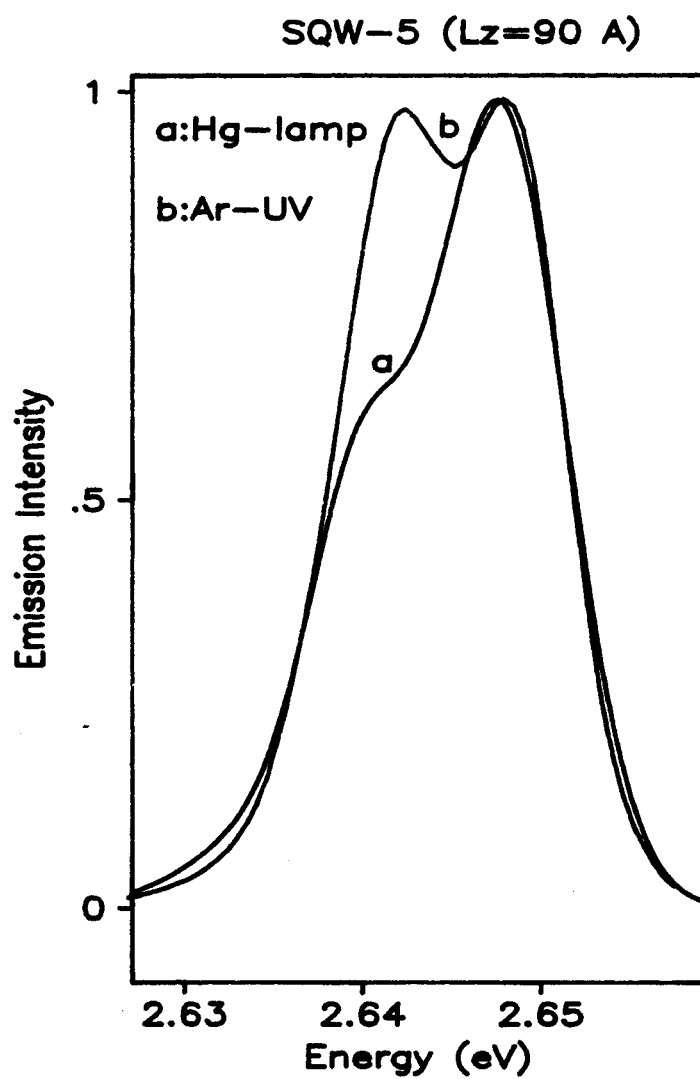
Figure 23.   Comparison of PL spectra of SQW-5 under argon
UV lines and Hg-lamp excitations.

TABLE III

Experimental results of SQW-5 PL spectra

---

	peak position (eV)	Intensity	FWHM (eV)
Under direct-excitation :			
Free exciton	2.6486	0.95293	0.009036
RRS	2.6453	0.40305	0.001581
Bound-exciton	2.6393	0.08079	0.007455
Under indirect-excitation :			
a) Ar -UV excitation :			
Free-exciton	2.649	0.6931	0.007778
Bound-exciton	2.6424	0.8703	0.011112
b) Hg-lamp excitation :			
Free-exciton	2.6484	0.9043	0.011968
Bound-exciton	2.6406	0.5811	0.009596

Figure 24 shows PL spectra obtained by <u>direct excitation</u> of the quantum-well; note the excitation photon energy of 2.707 eV (457.9 nm) is smaller than the energy gap of the ZnSe barrier layer. In this case, the barrier is transparent to the excitation energy. The PL spectrum can be deconvolved distinctively into three to four Gaussian bands by the least-square fit. The PL emission bands show a clear shift to lower energies and become narrower as the well-width is increased, similar to the features observed in Figure 19.

Figure 25 shows the luminescence spectrum at 8.7 K (curve with stars) obtained from $ZnSe/\ Zn_{0.86}Cd_{0.14}Se$ single quantum well heterostructure (SQW-5, 90Å well), under direct quantum-well excitation using the 2.707 eV laser line and the least square fit to three Gaussian bands. The main peak at 2.649 eV originates from the confined $n=1$ heavy hole free exciton transition. The peak at 2.639 eV is the exciton bound to a neutral donor that is likely to be the Ga donor at the Zn or Cd site, and the sharp peak at 2.645 eV, with half-width 1.58 meV, is the resonant Raman scattering (RRS) peak.

The emission spectra obtained by indirect excitation exhibit different features from spectra obtained by direct excitation. The main differences are - much-stronger low energy band (as can be seen from

Figure 19) and the absence of a strong Raman peak (R) that appears in the directly excited quantum well (Figure 24). The free and donor-bound exciton peaks obtained from least squares fit have linewidths of 7.7 meV and 11.1 meV, respectively, and correspond well to peaks obtained from the indirectly excited PL spectra.

Figure 26 shows the PL emission from the sample SQW-4, under direct excitation by the 2.707 eV laser line and its deconvolution into four Gaussian bands.

3.4 Temperature dependency:

Figure 27 shows the temperature dependence of PL emission from the sample SQW-5. We see that the resonant Raman peak is dominant even at temperature 90 K. The usual decrease in peak position can be attributed to the bandgap shrinkage, as the temperature is increased. But the interesting feature in the PL spectra is that the resonant Raman peak at 8.7 K appears on the lower energy side of the free-exciton energy peak, and shifts gradually toward lower energy. At about 50 K the the free-exciton and RRS peaks are overlapping. The resonant Raman peak at 70.5K appears on the high energy side of the free exciton line and is still dominant. At a temperature of 80.5K, the Raman peak decreases and shifts a little toward higher energy, and at
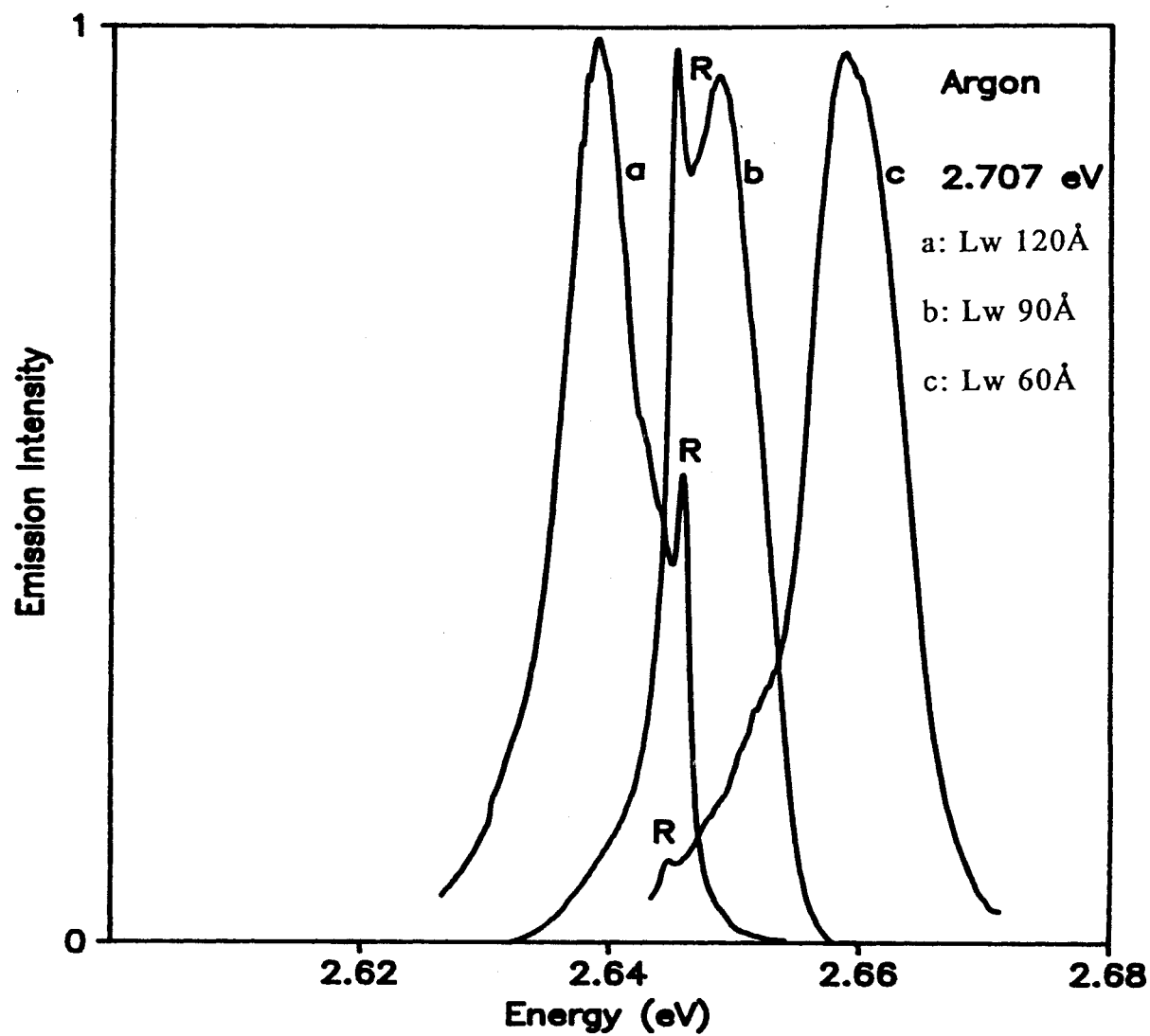
Figure 24. PL of single quantum-wells under argon 2.707 eV excitation.
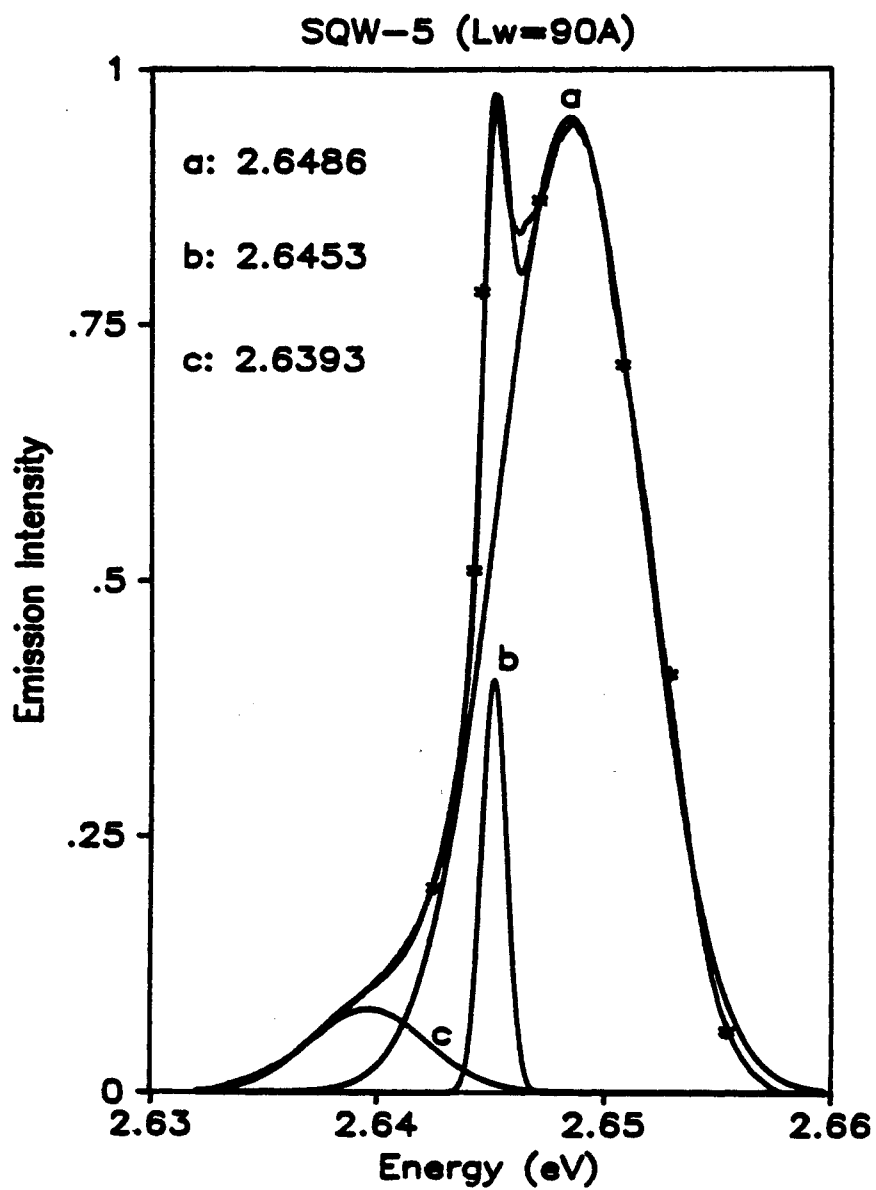
Figure 25. SQW-5 PL by argon 2.707 eV excitation and its deconvolution into three emission bands.
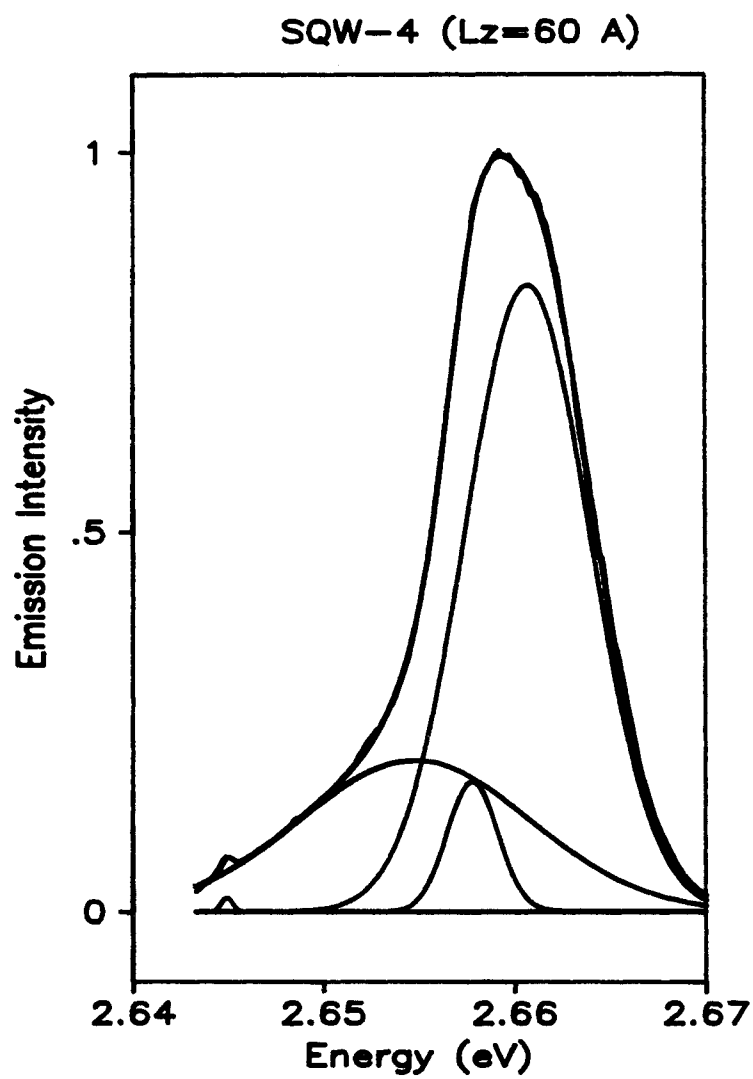
Figure 26. SQW-4 PL by argon 2.707 eV excitation and its
deconvolution into three emission bands.

90K it is weak. Figure 28 shows the temperature dependence of PL emission from the sample SQW-4.

Figure 29 shows the temperature dependence of the free exciton E_{1h} peak energies with circles denoting experimental data and the solid line indicating a theoretical fit to empirical data, as discussed in Chapter 2, using Varshni's formula [35]:

$$E_g (T) = E_g (0) - \alpha T^2/ (T+\beta)$$ (3.1)

where $E_g(0)= 2.648$ eV, the $Zn_{1-x}Cd_xSe$ bandgap at 0^0 K, constant $\alpha = (-4.022 \times 10^{-4})$ eVK^{-1}, and $\beta = (-350.23)$ K for quantum well SQW-5. Figure 30 shows the temperature dependence of the free exciton E_{1h} peak energies in SQW-4, with $E_g(0)= 2.6605$ eV, the $Zn_{1-x}Cd_xSe$ bandgap at 0^0 K, constant $\alpha= (-2.65 \times 10^{-3})$ eVK^{-1}, and $\beta= (-1420)$ K as the parameters that satisfy Eqn. (3.1).

Figure 31 shows the temperature dependence of the linewidth of this free excitonic emission for SQW-5. The half-width (FWHM) of the n=1 electron heavy hole excitonic emission increases slowly in the temperature range of 8.7-40 K, but increase more rapidly with temperatures above 40 K.
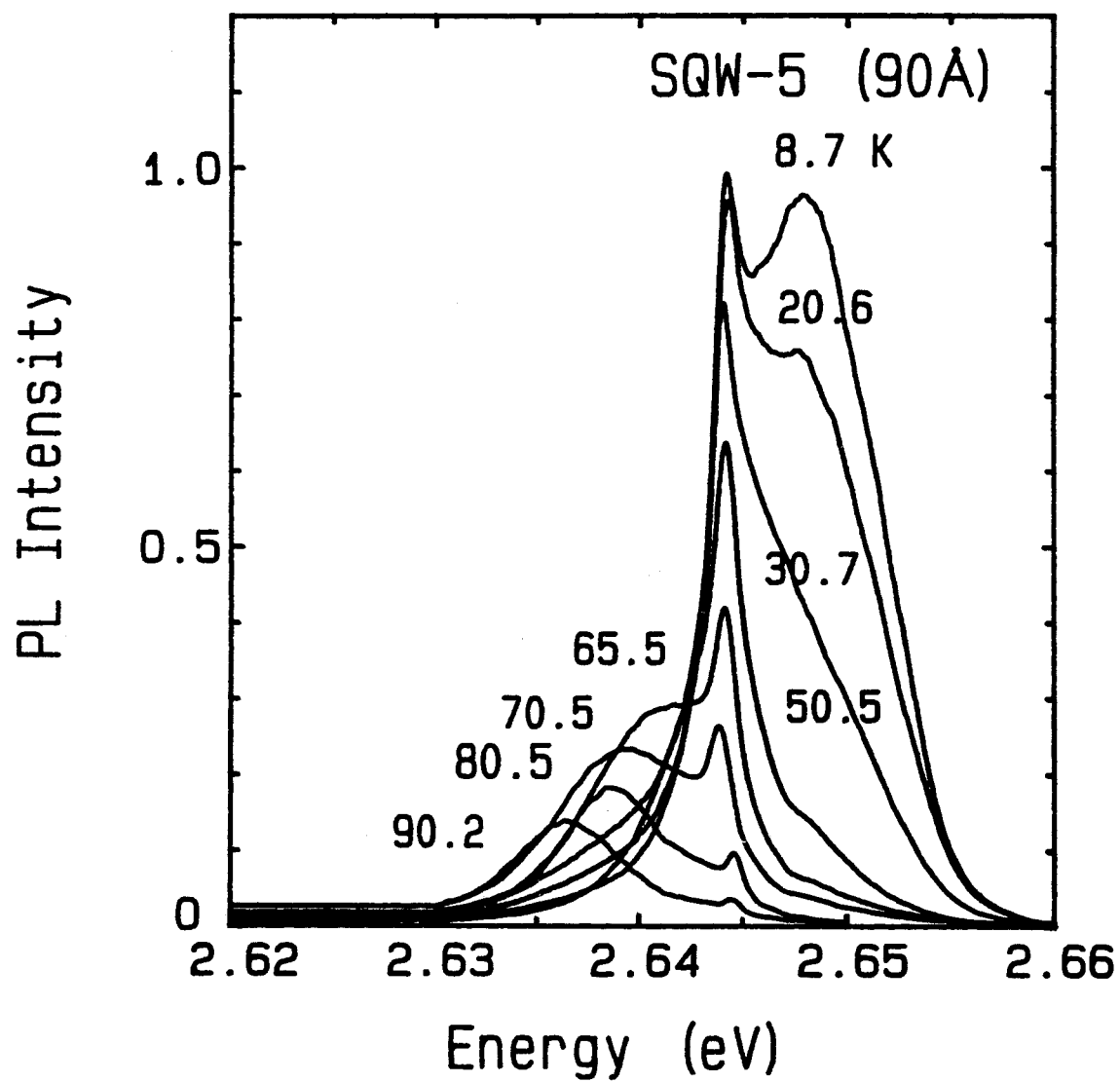
Figure 27. Temperature dependence of PL for SQW-5
under direct (argon 2.707 eV) excitation.
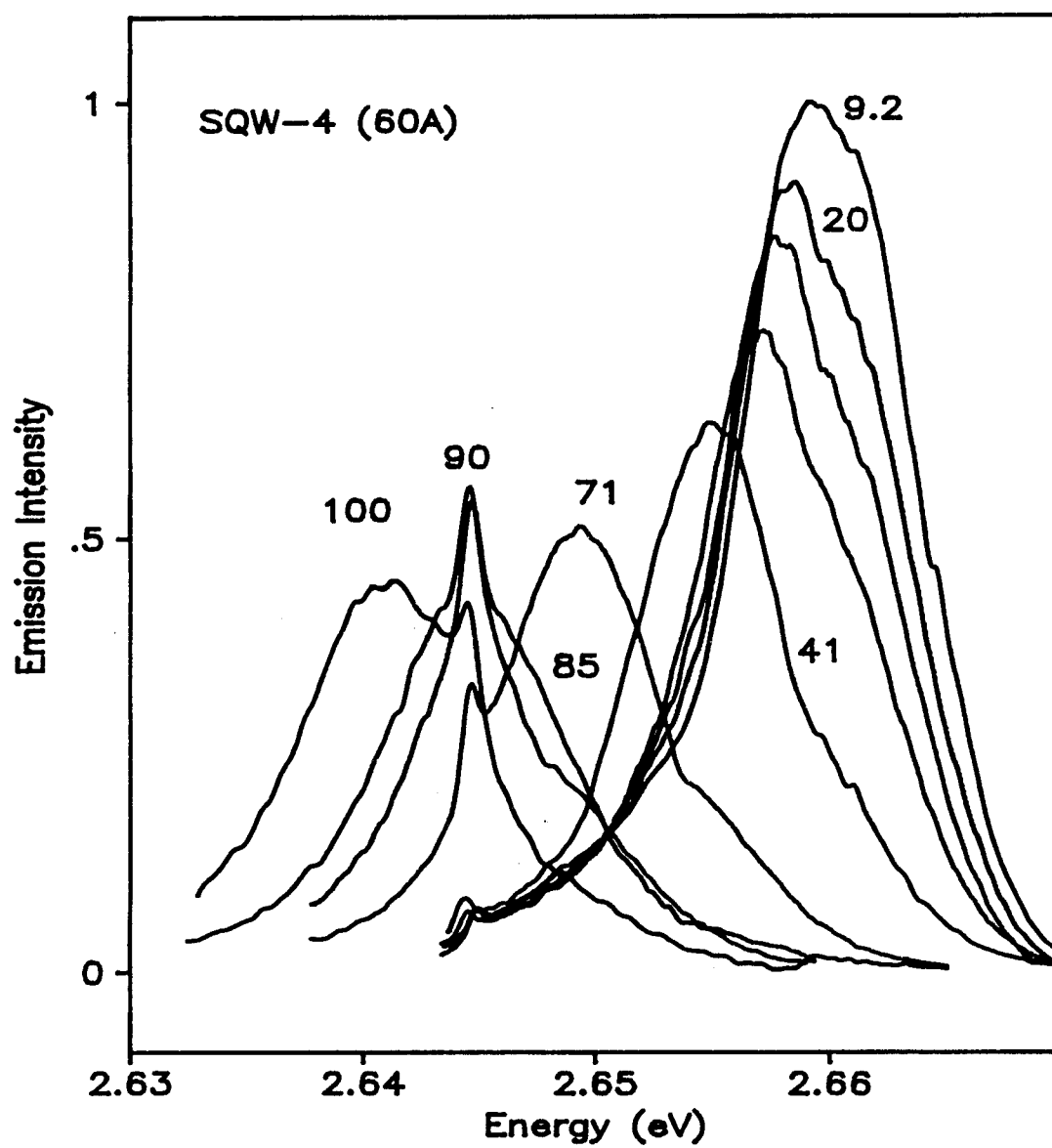
Figure 28. Temperature dependence of PL for SQW-4
under direct (argon 2.707 eV) excitation.
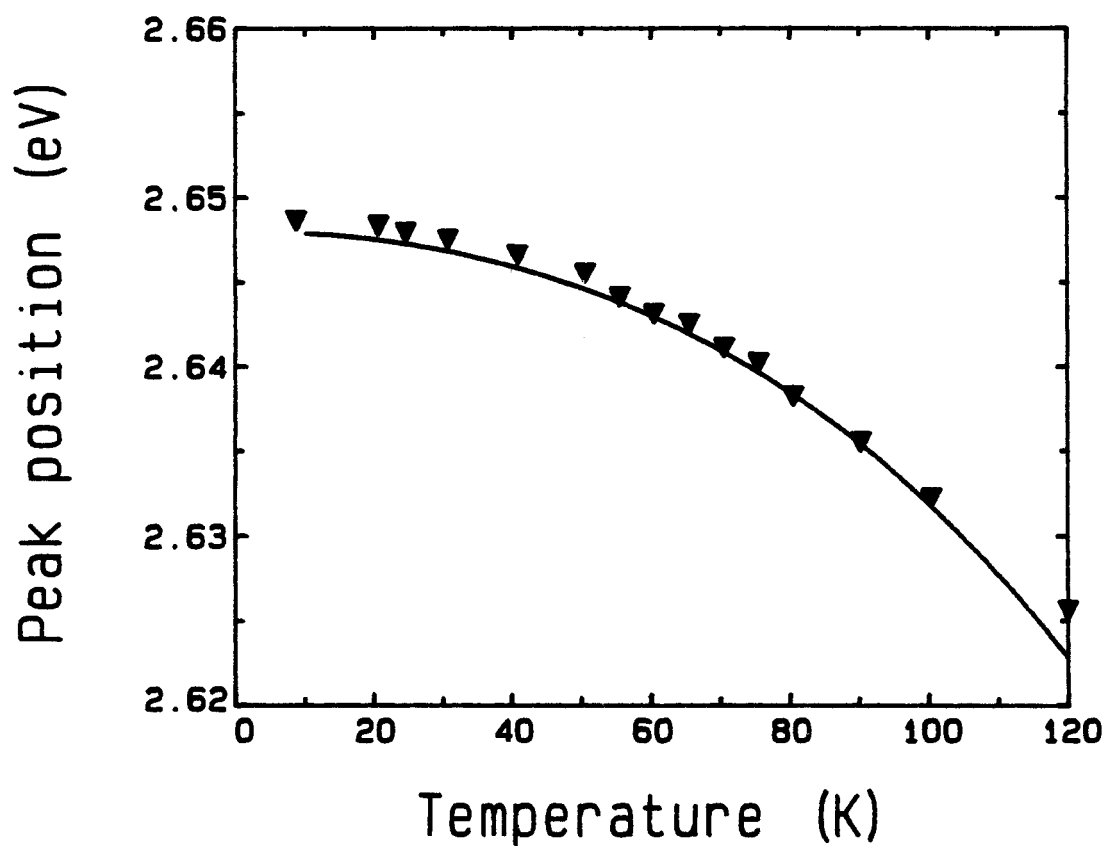
Figure 29. Temperature dependence of the free exciton E_{1h} peak energies, for SQW-5. The symbol denoting the experimental data and the solid line representing the theoretical fit.
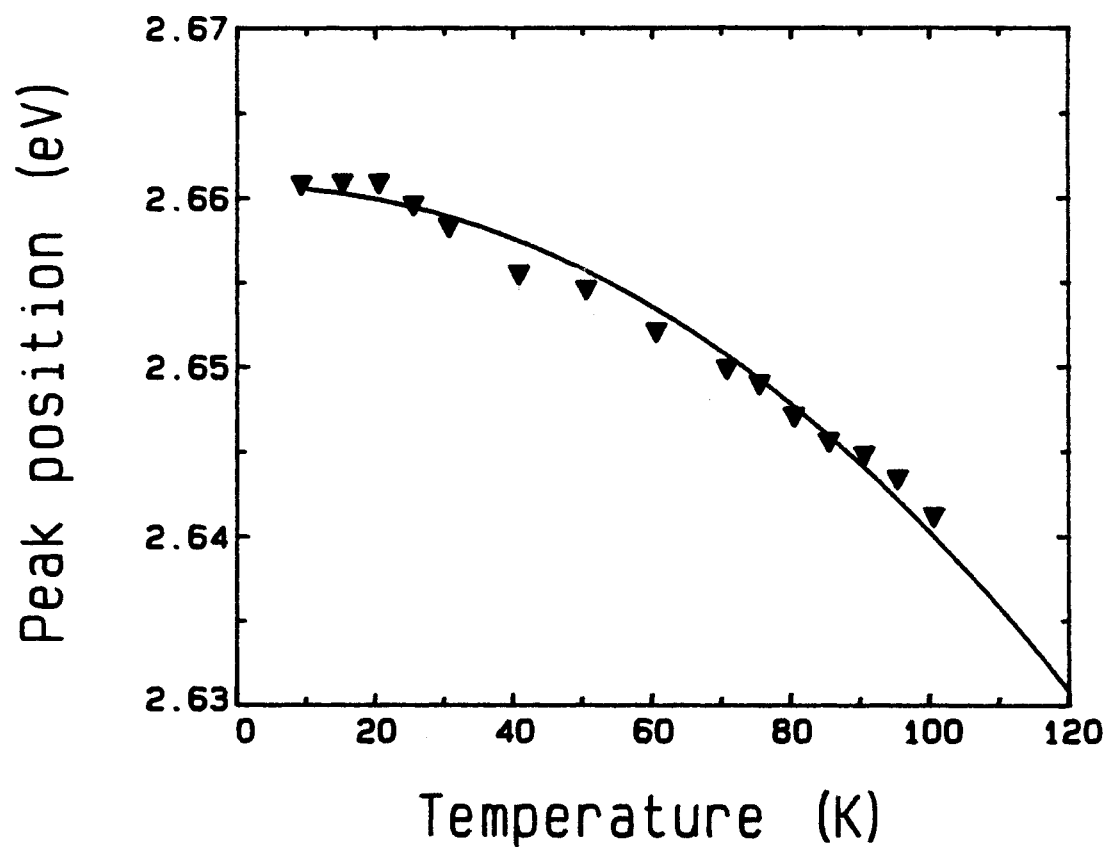
Figure 30.   Temperature dependence of the free exciton E_{1h}
peak energies, for SQW-4. The symbol denoting
the experimental data and the solid line
representing the theoretical fit.

The temperature dependence of the emission linewidth for the heavy hole exciton can be analyzed using equation [38]:

$$\Gamma_{total} = \Gamma_0^+ + \Gamma T + \Gamma_{ph}\left[\exp\left(\frac{E_{LO}}{kT}\right) - 1\right]^{-1} + \Gamma_{imp}\exp\left[\frac{-\langle E \rangle}{kT}\right]$$

(3.2)

The above equation for the linewidth of the exciton luminescence includes interactions with polar optical phonons (LO) Γ_{ph} (the third term), and with acoustic phonons via deformation and piezoelectric potential Γ (the second term). The first term Γ_0^+ is the linewidth due to inhomogeneous fluctuation of well thickness and the last term Γ_{imp} is the linewidth due to the ionized impurity scattering. The $\langle E \rangle$ is the average binding energy of the donor. The best fit to the experimental data shown in Figure 31 (solid line) is obtained if we choose $\Gamma_0^+= 8.8$ meV, $\Gamma= 4\times10^{-5}$ eV/K, $\Gamma_{ph}= 70$ meV, $E_{LO}= 30.81$ meV, $\Gamma_{imp}= 0.5$ eV and the donor binding energy $\langle E \rangle =25$ meV. Figure 32 details the temperature dependence of linewidth (FWHM) of heavy-hole exciton of sample SQW-4 (60A) . The best fit to the experimental data shown in Figure 32 (solid line) is obtained if we choose $\Gamma_0^+= 8.8$ meV, $\Gamma= 4\times10^{-5}$ eV/K, $\Gamma_{ph}= 70$ meV, $E_{LO}= 30.81$ meV, $\Gamma_{imp}= 0.35$ eV and the donor binding energy $\langle E \rangle =27.5$ meV.
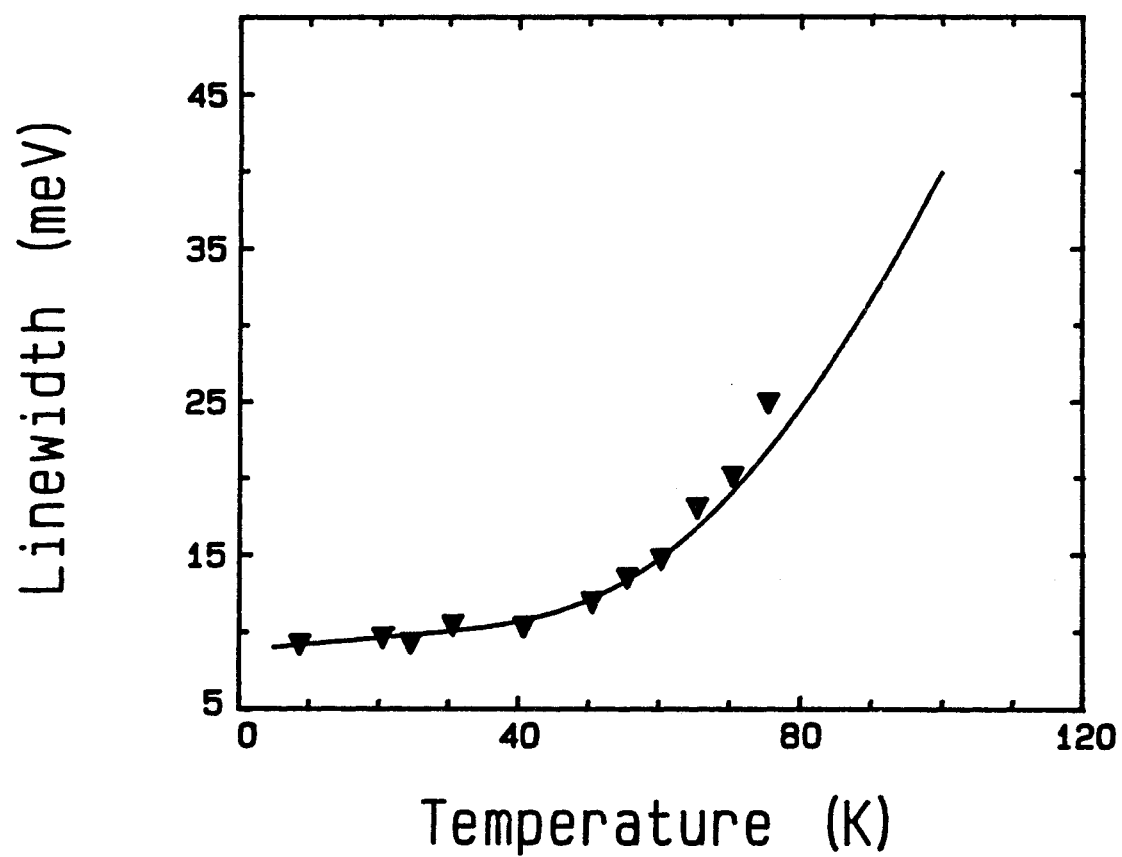
Figure 31. Temperature dependence of linewidth (FWHM) of free excitonic emission in SQW-5.
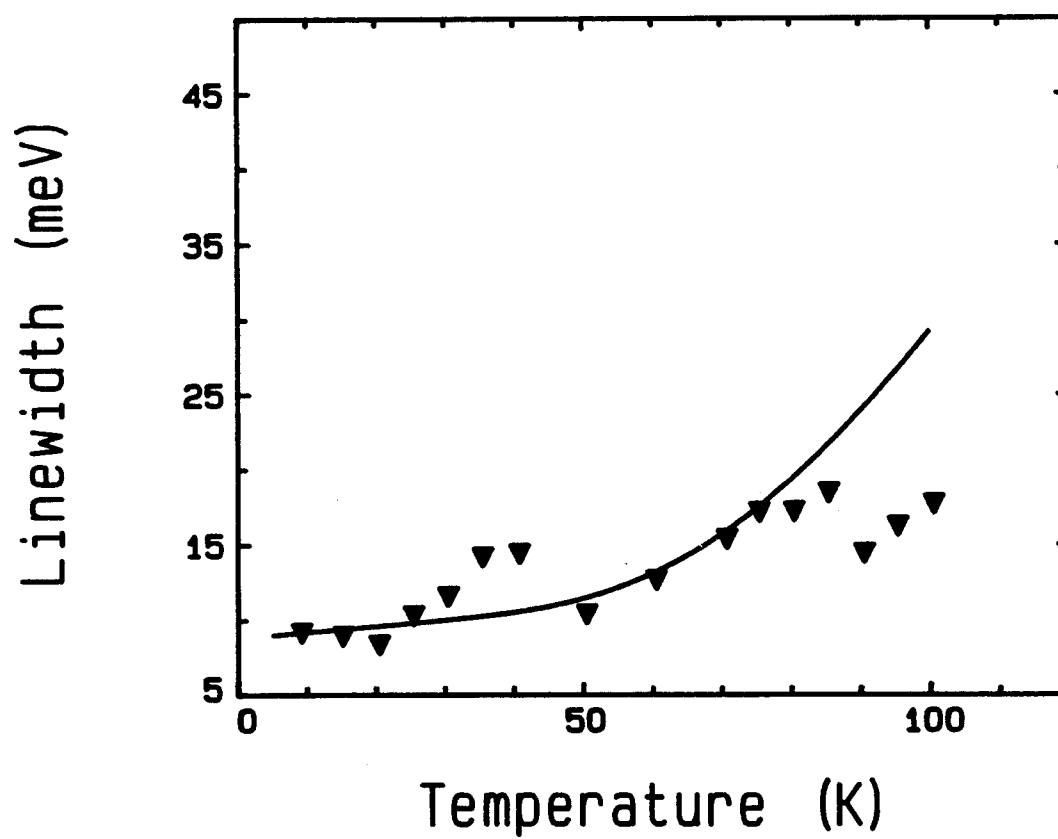
Figure 32. Temperature dependence of linewidth (FWHM) of free excitonic emission in SQW-4.

Tables IV and V list the experimental results for SQW-5 and SQW-4 respectively.

The temperature dependency of n=1 heavy hole exciton integral intensity is shown in Figure 33. The photoluminescent intensity is exponentially reduced in the temperature region 8.7 K-50 K mainly due to the thermal dissociation of excitons. In the higher temperature regions above 50 K, the PL intensity is exponentially reduced mainly due to the thermally activated nonradiative recombination channel. This PL quenching is characterized by higher activation energy. It is possible to fit the thermal quenching data for the integral emission intensity to the exponential expression [50]:

$$\frac{I(T)}{I(0)} = (1 + A\exp[-E_1/kT] + B\exp[-E_2/kT])^{-1}$$

(3.3)

From the fit of this expression shown in Figure 33 (solid line), the two activation energies are derived $E_1 = 17.7$ meV and $E_2 = 37.7$ meV for SQW-5. The activation energy E_1 corresponds to the dissociation of the excitons, however, if the exciton no longer exists, the reason for appearance of a second activation energy, despite this fact, is found in the difference between constants A and B (A=180, B=2.5×10^4) [48,50].
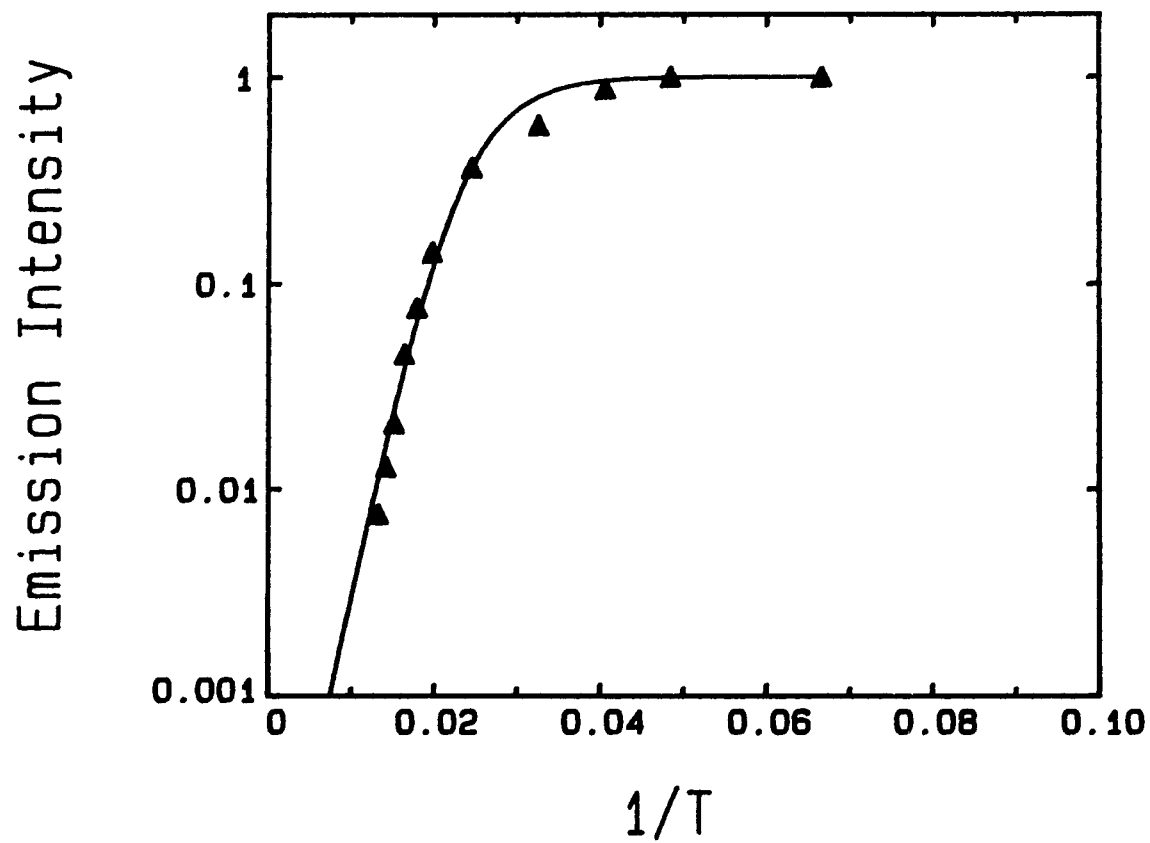
Figure 33. Temperature dependence of heavy-hole exciton integral intensity for SQW-5.

TABLE IV

Experimental details of the temperature dependency of
free-exciton emission in sample SQW-5 (Lz=90A)
under direct excitation

Temp (K)	Intensity	peak emission (eV)	FWHM (meV)	Area (x 10^5)
8.7	1154583	2.6486	9.1494	2485.1
20.6	1144477	2.6483	9.601	1930.1
24.6	998306	2.6479	9.2524	1678.8
30.7	666599	2.6475	10.3916	1346.0
40.8	416526	2.6466	10.0786	877.7
50.5	163281	2.6455	11.8602	480.9
55.5	153229	2.6441	13.4414	339.2
60.4	100412	2.6431	14.6842	229.5
65.5	78451	2.6425	17.96	158.6
70.5	58191	2.6411	19.9928	110.6
75.5	45497	2.6402		97.4
80.5	14049	2.6382		73.9
90.2	12999	2.6355		39.3
100.4	4778	2.6322		26.5
120.0	3950	2.6256		7.44

TABLE V

109

Experimental details of the temperature dependency

of free-exciton emission in sample SQW-4 (Lz=60A)

under direct excitation

Temp (K)	Intensity normalized	peak emission (eV)	FWHM (meV)	Area (x 10^5)
9.2	0.8072	2.6607	9.1318	1531.0
15.2	0.7936	2.6608	8.9034	825.2
20.5	0.6954	2.6608	8.3326	528.67
25.5	0.73935	2.6595	10.2734	361.19
30.6	0.79025	2.6582	11.5288	383.1
35.6	0.57366	2.6569	13.698	155.36
40.8	0.5508	2.6554	14.383	107.9
50.5	0.9942	2.6545	10.3434	122.4
60.6	0.80905	2.652	12.62	713.1
70.8	0.53422	2.6498	15.345	447.5
75.5	0.41485	2.6489	17.129	331.85
80.5	0.3126	2.647	17.163	251.5
85.5	0.22763	2.6455	18.413	182.9
90.6	0.49615	2.6447	14.374	184.6
95.4	0.45779	2.6433	16.184	134.1
100.6	0.45108	2.6411	17.656	95.78

3.5 Resonant Raman Scattering

Under resonant conditions, Raman scattering by longitudinal optical (LO) phonons in polar semiconductors can be observed in scattering configurations, which are forbidden according to selection rules. This phenomenon is due to the phonon-wave vector dependent contribution of the Frohlich electron - phonon interaction to Raman process. Phonon-wave vector is small in the first order scattering due to conservation of crystal momentum, where as the pairs of phonons participating in the corresponding second order scattering which enhances the Raman efficiency and is stronger [45].

In II - VI semiconductors which are more polar than III - V, the exciton - phonon coupling via the Frohlich interaction (LO phonons) is much stronger than via the deformation potential (LO and TO phonons). The ratios of the Frohlich (F) interaction to deformation potential (DP) interactions in II - VI semiconductors are larger than in III - V semiconductors (F/DP (II - VI) > F/DP (III- V)) [46,53]. In our experiment, the Raman scattering from a (100) crystal face was similar to the back scattering configuration and the Raman spectra are dominated by forbidden scattering from LO phonons [51,92].

Assuming the LO-phonon frequency in the quantum well layer with x=0.14 ($Zn_{0.86}Cd_{0.14}Se$) is the same as in bulk mixed crystal, the frequency is ω_{LO}= 248.5 cm^{-1} (30.81 meV). The Stokes shift of the resonant Raman peak for sample SQW-5 is 496.99 cm^{-1} (61.62 meV) which corresponds to two LO phonons with frequency ω_{LO} = 248.5 cm^{-1} (30.81 meV, Fig. 24). For SQW-6 and SQW-4, the LO frequencies are ω_{LO}= 246.48 cm^{-1} (30.56 meV) and ω_{LO}= 250.91 cm^{-1} (31.11 meV), respectively (see Table VI) . In Figure 24, under argon 2.707 eV excitation we find Raman peak (R1) at 2.6447 eV in SQW-4, peak R2 at 2.6453 eV in SQW-5, and peak R3 at 2.6458 eV in SQW-6, respectively. The observed Raman 2LO scattering (Fig. 34) is resonant with the free exciton energy for SQW-5 and near resonant with the free exciton energy for SQW-6 single quantum wells as can be seen in Figure 24. For SQW-4, a weak resonant peak is observed at the low energy shoulder of the exciton peak (Fig. 24). The striking feature of the 2LO outgoing resonance [44,52,53], (where the scattered photon energy equals that of the optical transition) is its sharpness and the large intensity (2 million photons/s for 100 mm wide slit) of the 2LO phonon which is comparable with the exciton E_{1h} photoluminescence intensity as shown in Figures 27 and 28. The detailed discussion of this 2LO resonant Raman scattering in $Zn_{1-x}Cd_xSe$ QW has been published [54,77].

TABLE VI

Phonon energies of II - VI compounds in meV

Compound	TO	Zone center TO$_1$	edge TO$_2$	LO	LO	Zone center LA	edge TA$_1$	TA$_2$
ZnO	-	54	52	-	60	30	17	12
ZnS	-	39	37	-	42	22	11	9
ZnS	290	37	-	31	26	20	11	-
ZnSe	26	26	-	31	26	20	11	-
ZnTe	24	22	-	26	23	16	6	-
CdS	30	30	30	38	37	19	10	9
CdSe (W)	23	19	-	27	25	14	7	-
CdTe (ZB)	17.4	17	-	21	22	13	8	-

The $E_{22h} = E_{2e} - E_{2hh}$, free exciton transition versus temperature is plotted (solid line) taking the theoretical value for E_{22h} at 8.7 K from our model (see theoretical approach section), and assuming the same temperature dependence as for E_{1h} transition. The two horizontal lines represent the energy of the exciting laser line E_{ex} and the 2LO phonon scattered photon energy $\hbar\omega_{S2LO}$, is shown in Figure 34. The inter-section of the E_{1h} curve with the 2LO phonon scattered photon line defines the condition for (the outgoing resonance) RRS. At the 2LO resonance the scattered $\hbar\omega_{S2LO}$ photon energy peak falls right on the top of the E_{1h} free exciton peak (see Figure 27) which occurs at temperature 50 K. With the temperature tuned bandgap (1e -1hh) of the single quantum well, we have been able to observe RRS of the confined 2LO phonon from the $Zn_{0.86}Cd_{0.14}Se$ well layer. The heavy hole exciton E_{22h} curve in Figure 34 for SQW-5 crosses the excitation laser energy E_{ex} line at a temperature of about 47 K and defines the incoming resonance [44], which is very close to the temperature (50 K) where we observed outgoing resonance with E_{1h} free exciton. Similarly, the heavy hole exciton E_{22h} curve in Figure 35 for SQW-4 crosses the excitation laser energy E_{ex} line at a temperature of about 90 K and defines the incoming resonance [44], which is very close to the temperature (89 K) where we observed outgoing resonance with E_{1h} free exciton.
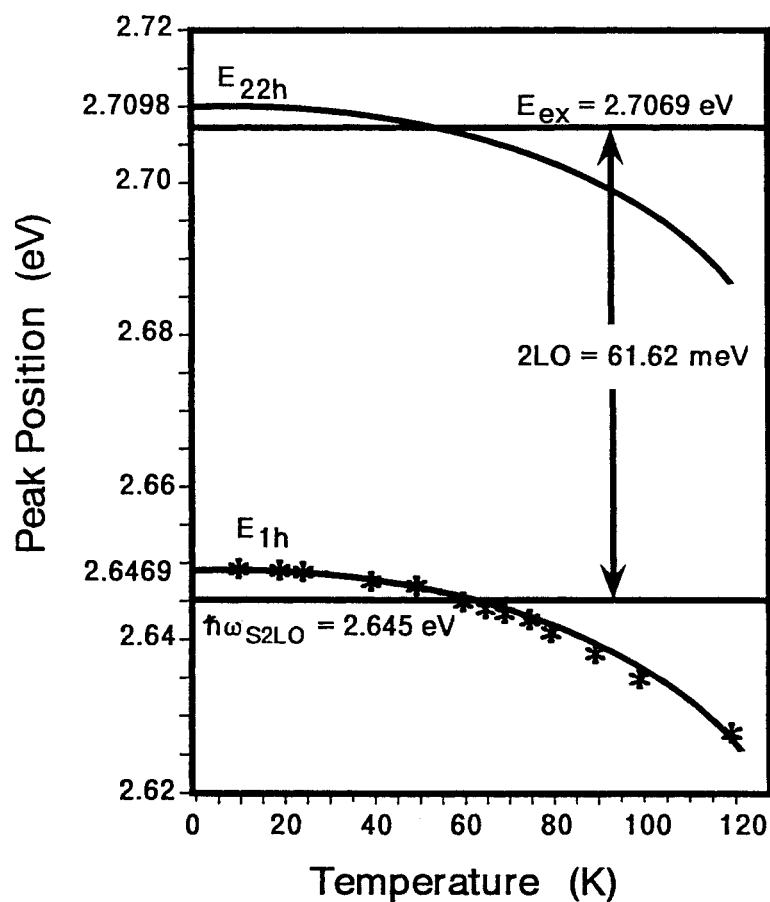
Figure 34. Temperature dependence of the free exciton
peak energy E_{1h} and E_{2hh} from SQW-5. The two
horizontal lines represent the exciting laser line
E_{ex} and the 2LO-phonon scattered phonon energy
$\hbar\omega_{S2LO}$.
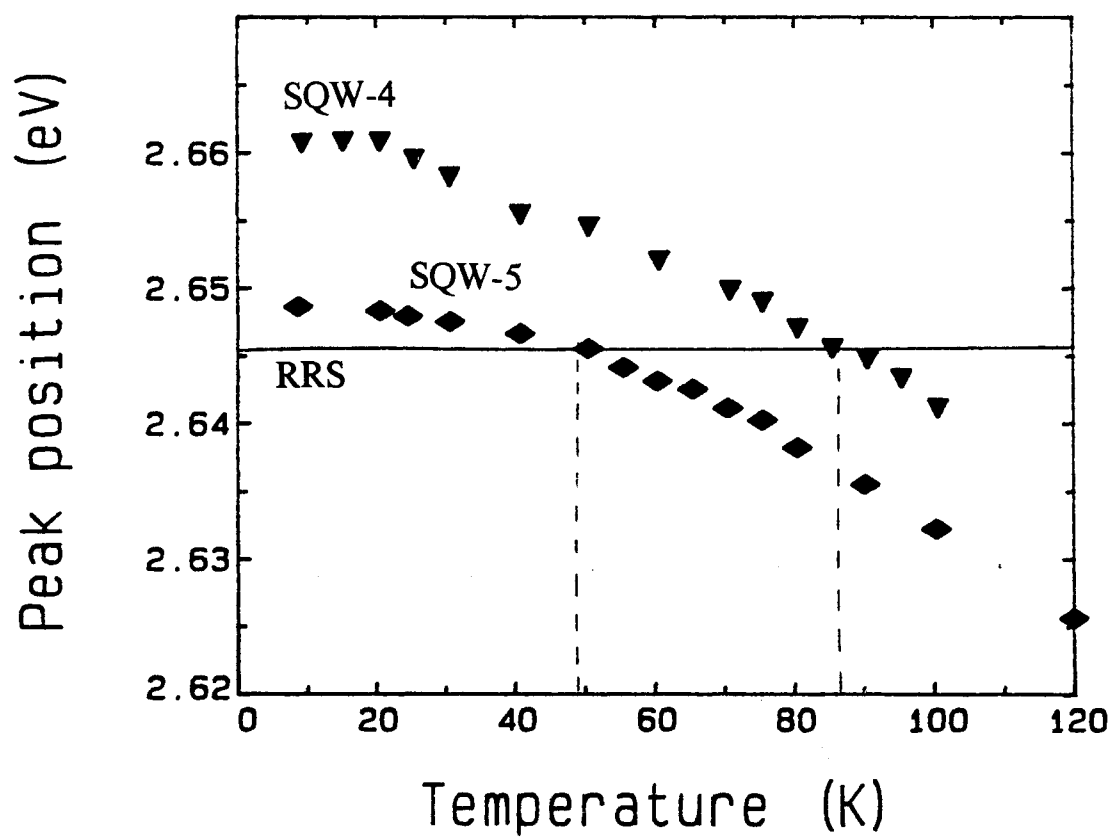
Figure 35. Temperature dependence of the free-exciton peak energy E_{1h} in SQW-5 and SQW-4 and the intersection of Raman scattered line.

Figure 36 shows the Raman peak intensity as a function of temperature in the temperature range 8.7-120K. The experimental data is the convolution of three effects: the temperature dependence of the Raman scattering process; the temperature dependence of LO frequencies [55]; and temperature detuning of the resonance Raman scattering process, which has been discussed in detail above (Fig. 24). The linewidth (FWHM) of the RRS line is 1.65 meV and remains fairly constant with temperature.

3.6 Circular Polarization (CPL) spectra:

Figure 37 shows the SQW-5 PL emission under σ+ excitation and Figure 38 shows the sample SQW-5 PL emission under σ- excitation. The spin-flip of Raman peak is evident in these figures. And also the intensity of free exciton peak is stronger under σ- excitation than the Raman peak, where as the intensities are almost equal under σ+ excitation. The degree of polarization is approximately +0.02 for σ+ excitation and -0.05 for σ- excitation.
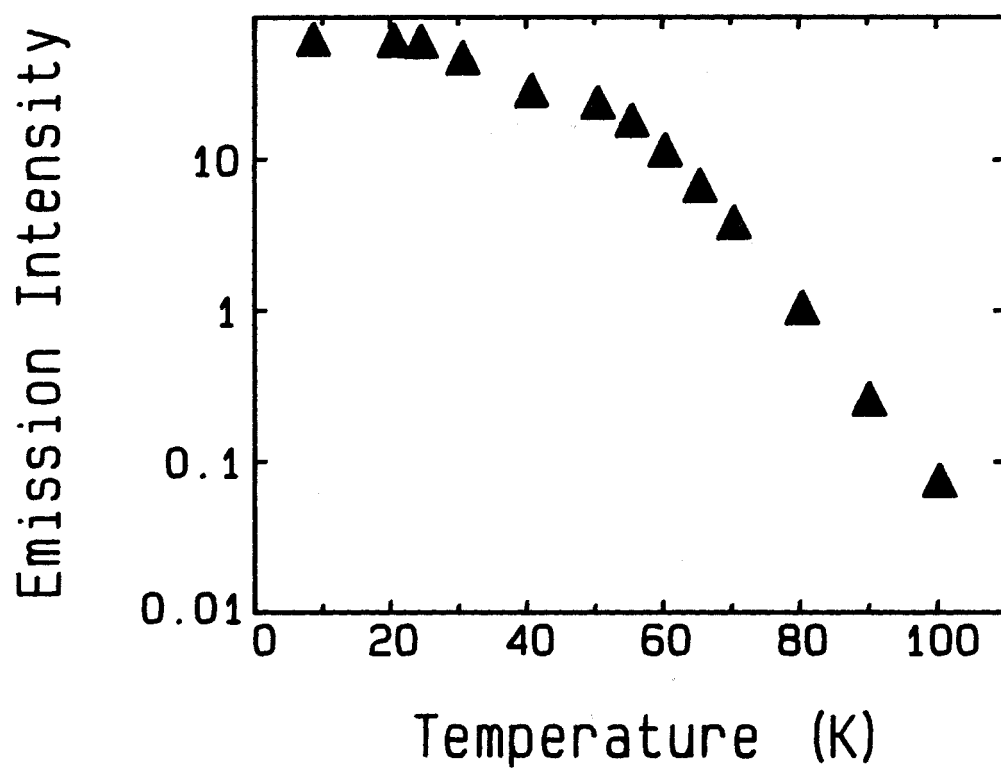
Figure 36. Raman peak intensity as a function of temperature.
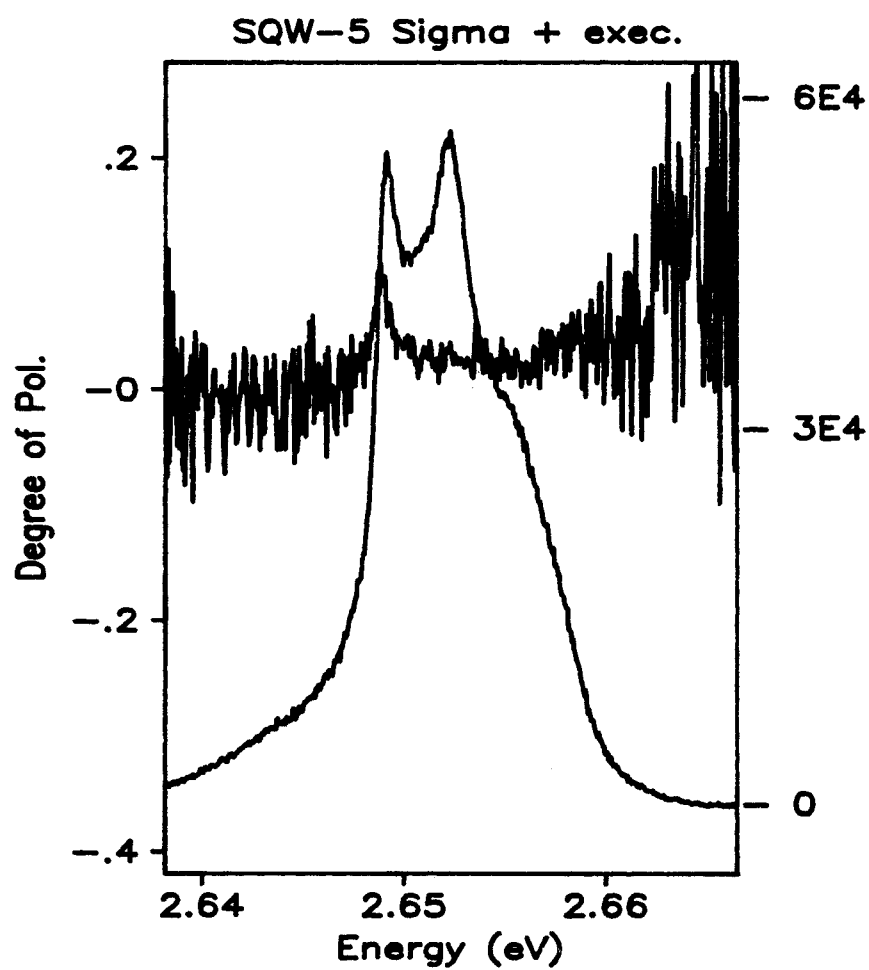
Figure 37.   CPL spectra of SQW-5 under σ+ excitation.
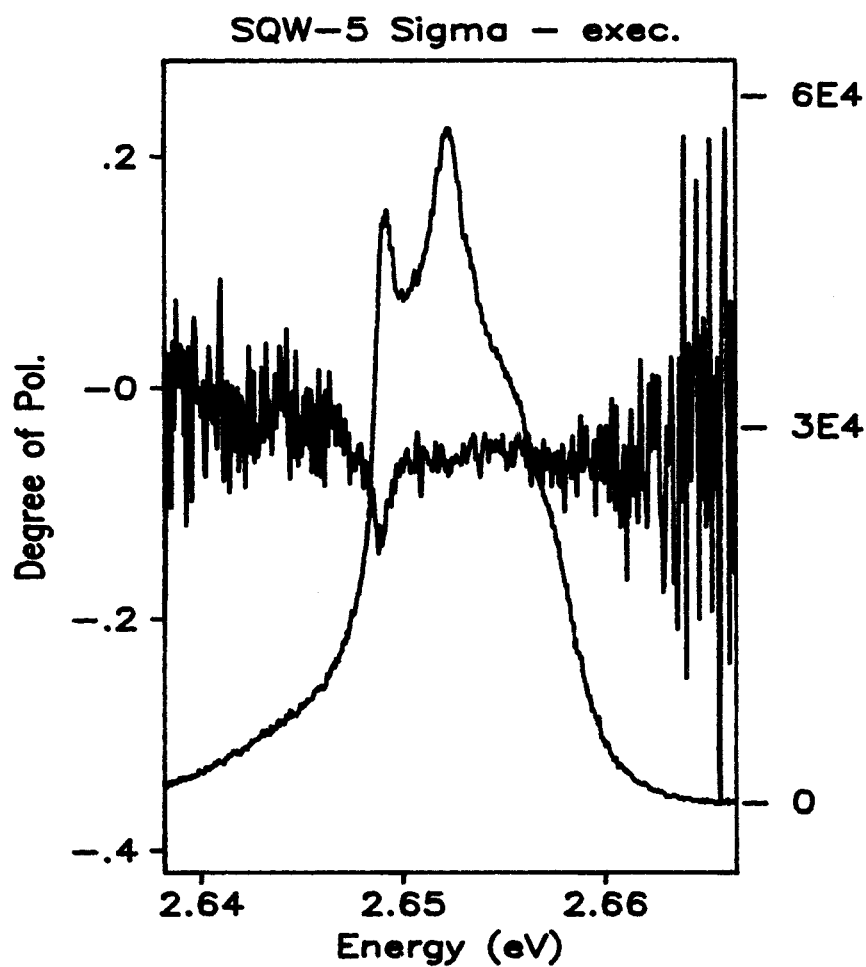
Figure 38.   CPL spectra of SQW-5 under σ- excitation.

CHAPTER 4

THEORETICAL ANALYSIS
AND DISCUSSION

In this Chapter, the bandgap as a function of the composition, the band offset, confined carrier energies in the quantum-well based on a finite-square-potential-well model taking into account the band nonparabolicity by energy dependent effective masses, strain due to lattice-mismatch, and the effects of strain on the transition energies are computed. Experimental results found by luminescence measurements are compared with the theoretical calculations.

4.1   Theoretical bandgap as a function of composition:

The theoretical bandgap of $Zn_{1-x}Cd_xSe$ varies with composition, and is calculated by substituting Bandgap of CdSe for E_g (B) and bandgap of ZnSe for E_g (A), in Eqn (2.26) of Chapter 2, and write :

$$E_g(x) = E_{gCdSe} + (E_{gZnSe} - E_{gCdSe} - b)x + bx^2$$

$$(4.1)$$

where ' b' is the bowing parameter. The bowing parameter, b, is calculated from the equation:

$$b = \frac{Ze}{8\pi\epsilon_0} \left\{ \left(\frac{1}{r_M} - \frac{1}{r_N} \right)^2 (r_M + r_N) \exp\left(-sa\frac{\sqrt{3}}{8}\right) \right\}$$

(4. 2)

where 'Z' is the valence number of the intersubstitutional ions Cd and Zn, 'a' is the lattice constant of the mid-composition alloy, 's' is the screening constant (s=0.25 $Å^{-1}$) and r_{Cd} (r_M) and r_{Zn} (r_N) are the Pauling's covalent radii of elements Cd and Zn, respectively.

The lattice constant of the mid-composition alloy, 'a', is calculated from Vegard's law which states that the lattice constant of the solid solution varies linearly with composition. Using for $ZnSe_{ZB}$ lattice constant a=5.6676Å and for $CdSe_{ZB}$ lattice constant a = 6.077Å [65], the lattice constant of the mid-composition ($Zn_{0.5}Cd_{0.5}Se$) is a= 5.8723 Å. Using covalent radii, r_{Cd} = 1.405 Å and r_{Zn} =1.225 Å [57], the calculated bowing parameter is b = 0.301. Figure 39 shows the composition dependence of the band gap for $Zn_{1-x}Cd_xSe$ alloys at 10 K, computed by taking the bowing parameter b=0.301, the band gap of ZnSe (ZB) E_g = 2.821 eV and the band gap of CdSe (ZB) E_g= 1.765 eV. The band gap of CdSe (ZB) E_g=1.765 eV is obtained by adding the free exciton binding energy, 15 meV (for CdSe-WZ [58,59]) to free exciton energy 1.75 eV, determined at 10K, from the photo-reflectance and piezomodulation spectroscopy at 10K [65] (see Tables VII and VIII). By substituting the band gap of ZnSe and CdSe (ZB), the
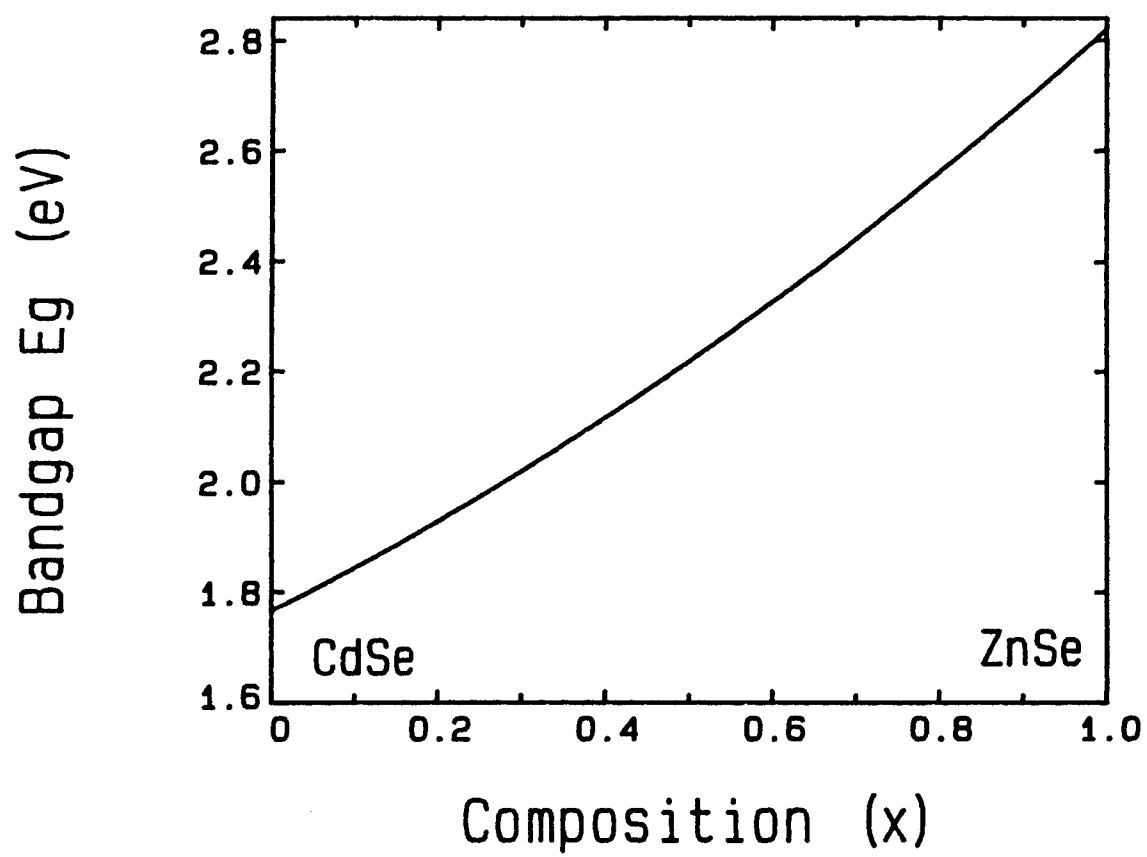
Figure 39. Bandgap computed as a function of composition 'x'.

TABLE VII

Exciton binding energies and Valence band
splitting energies in meV

Compound	Structure	E_{eb}	Δ_{SO}
ZnO	W	59	8.7
ZnS	ZB	40.1	72
	W	40.1	92
ZnSe	ZB	19	430
ZnTe	ZB	10	900
CdS	W	29.4	65
CdSe	W	15.7	420
CdTe	ZB	10	900

TABLE VIII

Band gap and Lattice constants of II-VI compounds

Compound	Lattice constant (A)	Eg (eV)
ZnS	5.4093	3.84
ZnSe	5.6676	2.821
ZnTe	6.1037	2.395
CdS	5.802	2.58
CdSe (ZB)	6.077	1.765
CdTe	6.481	1.597

bandgap of $Zn_{1-x}Cd_xSe$ quantum-well sample for composition x=0.14 is, E_g = 2.6355 eV.

4.2 Conduction and valence-band offsets:

A discussion of the theory of band offsets and experimental techniques used to obtain bandoffsets [16,60] has been done in Chapter 2. We have not experimentally obtained the band offset between ZnSe and $Zn_{0.86}Cd_{0.14}Se$, but we estimate the band offset from the Harrison Atomic Like Orbital (HAO) theory given by H. Kroemer [60] in a simple table form (Table IX). The electron affinity rule gives the conduction band step ΔE_c= 120 meV and the valence band step ΔE_v= 65 meV, for the electron-affinities χ_{CdSe} = 4.95 eV and χ_{ZnSe} = 4.09 eV. Based on the HAO theory, the valence band edge energy E_{v1} (ZnSe) = -0.82 eV and E_{v2} (CdSe) = - 1.05 eV; the valence and conduction band discontinuities are ΔE_v= 32.2 meV and ΔE_c= 153.28 meV respectively. The ZnSe/ $Zn_{0.86}Cd_{0.14}Se$ value is the value extrapolated from ZnSe/ CdSe value. The electron-affinity rule gives twice the valence band offset ΔE_v, as compared to the value obtained from HAO theory.

TABLE IX

126

Bandedge energies in eV.

All energies are expressed relative to the top of

the valence band of GaAs (HAO theory). The columns represent

equal anions and the rows represent equal cations.

III/V Compounds

	P	As	Sb
Al	1.95	2.17	2.44
	-0.50	-0.04	+0.86
Ga	1.79	+1.42	+1.57
	-0.47	0.00	+0.84
In	+1.24	+0.68	+1.29
	-0.11	+0.32	+1.12

II/VI Compounds

	S	Se	Te
Zn	+1.93	+1.82	+2.42
	-1.87	-1.05	+0.03
Cd	+0.97	+1.02	+1.81
	-1.59	-0.82	+0.21

The bottom entry represents the valence bandedge, and the

top entry the conduction bandedge.

4.3 Confined carrier energies :

The single quantum well is characterized by a finite square potential well model. The confined electron and hole energies are calculated by finding the root of the equation numerically, similar to Gershoni [28]:

$$f(k_b K_w) = \left(\frac{K_w m_{eb}}{k_b m_{ew}} - \frac{k_b m_{ew}}{K_w m_{eb}} \right) \sin(K_w L_w) - 2\cos(K_w L_w)$$

where:

$$k_b = \sqrt{\frac{8\pi^2(V - E) m_{eb}}{h^2}} \quad , \quad K_w = \sqrt{\frac{8\pi^2 E m_{ew}}{h^2}} \tag{4.3}$$

L_w, m_{ew}, m_{eb} stand for the width of the well and the carrier effective masses for well and barrier respectively. V is the barrier potential or the band discontinuity.

C.K. Williams et al. [61] have studied the ballistic transport of carriers in GaAs using Monte Carlo simulation, defining the duration and spatial extent of ballistic transport for an electron distribution. They propose a model for GaAs that includes nonparabolic conduction bands described by

$$p^2 = 2m^*\varepsilon \,(1 + \alpha \,\varepsilon) \qquad\qquad (4.4)$$

where p is the momentum, ε is the kinetic energy of the electrons, m^* is the band-edge effective mass, and α is band nonparabolicity given by:

$$\alpha = (1 - m^*/ m_0)^2 \,/\, E_g \qquad\qquad (4.5)$$

D. F. Welch et al. [62] have calculated the conduction band discontinuity, using the effective mass and band nonparabolicity in (Ga,In)As/ (Al,In)As heterojunction. They report that, the energy dependence of the mass is $m^* = m_0^* \,(1 + \alpha\varepsilon)$. Then, the energy-dependent effective mass for electrons $m_e^* = m_{e0}^* \,(1 + \alpha_e\varepsilon)$, and for holes $m_h^* = m_{h0}^* \,(1 + \alpha_h\varepsilon)$, respectively. Values of m_{eo}^* and m_{ho}^* are obtained by linear combination of the respective binaries. In our calculations, the band nonparabolicity correction is introduced by using an energy dependent effective mass $m_{ew}(E) = m_{ew}(0)$ $(1 + 2\alpha_{w,b}E)$, $\alpha_{w,b} = (1 - m_{ew,b}(0)/ m_0)^2 / E_{gw,b}$ [61,62], where $m_{ew,b}(0)$ are the band edge effective masses of electrons in the well or barrier respectively; $\alpha_{w,b}$, $E_{gw,b}$ are the nonparabolicity and the band gaps of the well or barrier respectively; m_0 is the free electron mass and E is the electron energy. For the heavy and light hole valence bands, equivalent relationships are formed. A computer algorithm was used to calculate the eigenvalues satisfying the time-independent solutions of

Schrodinger equations. The constants used in the calculations that satisfy Eqn. (4.3) are listed in Table X.

4.4 Strain and strain shifts:

The effect of elastic strain in the quantum wells are computed using equations developed for III-V structures [33]. The lowest conduction bands in ZnSe and $Zn_{0.86}Cd_{0.14}Se$ have s-like character so they do not change due to uniaxial strain. However, the fourfold $P_{3/2}$ multiplets and a twofold $P_{1/2}$ multiplet of the valence bands will split under the stress and shift relative to the conduction band [34]. The ZnSe- $Zn_{0.86}Cd_{0.14}Se$ quantum well has internal strain because of the 1.011% lattice mismatch between the ZnSe (ZB) (lattice constant $a = 5.6676$ Å) and $Zn_{0.86}Cd_{0.14}Se$ (ZB) (lattice constant $a = 5.7249$ Å). The planes of ZnSe that are parallel to the quantum well interface will be under the action of tensile stress, while the $Zn_{0.86}Cd_{0.14}Se$ will be compressed. The effect of biaxial compressive and tensile strain on the energy bands of ZnSe/ $Zn_{1-x}Cd_xSe$ quantum-well is shown in Figure 40. An increase of the band gap of $Zn_{0.86}Cd_{0.14}Se$ and a splitting of the Γ_8 valence band due to uniaxial compression, as discussed in the literature review, is given by [33]:

$$\Delta E_0(1) = \left[-2a\left(\frac{C_{11} - C_{12}}{C_{11}} \right) + b\left(\frac{C_{11} + 2C_{12}}{C_{11}} \right) \right] \epsilon$$

$$\Delta E_0(2) = \left[-2a\left(\frac{C_{11} - C_{12}}{C_{11}} \right) - b\left(\frac{C_{11} + 2C_{12}}{C_{11}} \right) \right] \epsilon \qquad (4.6)$$

$$\Delta(E_0 + \Delta) = -2a\left(\frac{C_{11} - C_{12}}{C_{11}} \right) \epsilon$$

for heavy hole, light hole and split band respectively. In the above equations, "a" is the hydrostatic deformation potential, "b" is the shear deformation potential, C_{11}, C_{12} are the elastic stiffness constants, and ϵ is the elastic strain (positive for compressive stress) calculated from:

$$\epsilon = \frac{[a(Zn_{1-x}Cd_xSe) - a(ZnSe)]}{a(ZnSe)} \qquad (4.7)$$

the computed value of strain is $\epsilon = 0.01$, for x=0.14 and taking parameters from Table X.

Because the experimental elastic constants, C_{ij}, and deformation potentials, a and b for zinc blende CdSe are unavailable, we computed the elastic constants C_{11} and C_{12} for cubic CdSe from wurtzite experimental data using the procedure described by Martin [63]. According to Martin, the bulk modulus $B = 1/3 (C_{11} + 2C_{12})$, and two

TABLE X

Constants Used in Confined Energies Calculations

Name	ZnSe	CdSe	$Zn_{0.86}Cd_{0.14}Se$	
E_g (eV at 9K)	2.821	1.765	2.63552	a
m_e (e.m.u)	0.16	0.13	0.1558	b
m_h (e.m.u)	0.6	0.45	0.579	b
ΔE_c (eV at 9K)	0.826		0.15328	b
ΔE_v (eV at 9K)	0.23		0.0322	b
α_{ew}			0.270411	b
α_{hw}			0.067251	b
α_{eb}			0.250124	b
α_{hb}			0.056717	b

a . From our calculation [Eqn. (4.1)].

b . Linearly interpolated from the binary materials data.

E   E   E

E_c

$E_g'' > E_g$ E_g $E_g' < E_g$

J=3/2, m$_J$ = ±1/2

J=3/2, m$_J$ = ±3/2 E_{hh} J=3/2, m$_J$ = ±3/2

J=3/2, m$_J$ = ±1/2 E_{lh} J=1/2, m$_J$ = ±1/2

J=1/2, m$_J$ = ±1/2 E_{so}

K_z K_z K_z

Compressive   No   Tensile
Stress   Stress   Stress
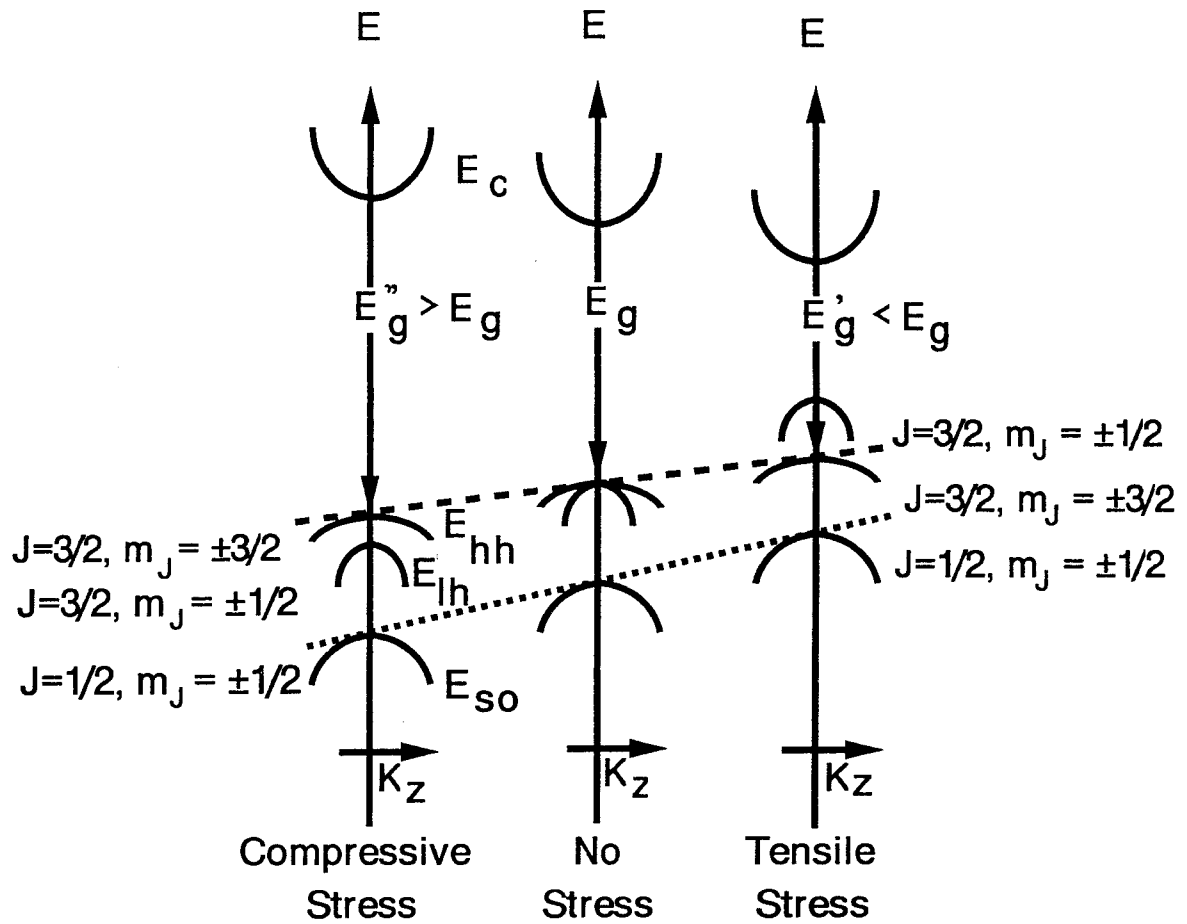
Figure 40.   Effect of biaxial compressive (in $Zn_{1-x}Cd_xSe$ QW)
              and tensile (in ZnSe barrier) strain on the energy
              bands.

shear constants $C_s = 1/2 (C_{11} - C_{12})$ and C_{44} for any semiconductor can be computed. All these constants have units of 10^{11} dyn /cm^2. From Table-II, the effective cubic constants for wurtzite CdSe are:

$$B^{eff} = 5.31$$
$$C_s^{eff} = 1.02$$
$$C_{44}^{eff} = 2.23$$

substituting the above constants into the expressions of B and C_s, we get the elastic constants $C_{11} = 6.67 \times 10^{11}$ dyn/cm2 and $C_{12} = 4.63 \times 10^{11}$ dyn/cm^2 for CdSe (ZB) zinc-blende structure derived from wurtzite values.

The hydrostatic deformation potential "a" was obtained using the relationship:

$$a = -\frac{1}{3}(C_{11} + 2C_{12}) \frac{\partial E_g}{\partial P} = -3.664 \quad eV \qquad (4.8)$$

where $\dfrac{\partial E_g}{\partial P} = 6.9 \times 10^{-11}$ [eV m^2/ N] [64] is the theoretical value of the pressure dependence of the band gap of CdSe (W).

The material parameters for $Zn_{1-x}Cd_xSe$ listed in Table XI were computed by linear interpolation from the binary materials data.

TABLE XI

The material parameters C_{ij} - elastic stiffness, in (N/m^2) a - the hydrostatic deformation potential (eV),   b - the shear deformation potential (eV)

	C_{11}	C_{12}	a	b
ZnSe (ZB)	8.26×10^{10} (a)	4.98×10^{10} (a)	-4.25 (b)	-1.2 (b)
CdSe (ZB)	6.67×10^{10} (a)	4.63×10^{10} (a)	-3.664	-0.8 (d)
$Zn_{0.86}Cd_{0.14}Se$ (ZB)	8.04×10^{10} (c)	4.93×10^{10} (c)	-4.17 (c)	-1.14 (c)

a. Reference 63

b. Reference 91

c. Linearly interpolated from the values of ZnSe and CdSe parameters.

d. taken as a fitting parameter.

The shear deformation potential "b" for CdSe- ZB is taken as a fitting parameter. The calculated energy shifts of the heavy-hole, light-hole and split valence bands at k=0, equation (4.6), to the first order in the strain are:

$$\Delta E_o (1) = 0.69\epsilon \ \ eV$$
$$\Delta E_o (2) = 5.77\epsilon \ \ eV$$
$$\Delta(E_o + \Delta) = 3.22\epsilon \ \ eV$$

The light hole subbands are not confined because, the elastic strain energy shift is 58.3 meV, which is bigger than the valence band offset 32.2 meV. Figure 41 shows the allowed electron- heavy hole transitions.

Figure 42 shows the peak luminescence photon energy versus the well thickness for samples with x= 0.14 measured at 8.6 K and the thicknesses of quantum wells of 60Å, 90Å, and 120Å respectively. The solid lines show the results of the calculations including the strain-induced shift and exciton binding energy which we assume as 18 meV. The 18 meV binding energy corresponds to a Bohr radius of about 38 Å which is smaller than the width of the investigated quantum wells and no increase of exciton binding energy is expected.

The experimental results are in good agreement with calculated theoretical values. The E_{1e} and E_{1hh} confinement energies are 17.85 meV, and 4.55 meV respectively, taking the effective mass and other parameters as listed in Table X.

The observed energy position for the free exciton peak is interpreted in terms of a strain induced $Zn_{1-x}Cd_xSe$ band increase which we computed from equation (4.6). The computed strain shift of the heavy-hole band is 6.82 meV (~7.0 meV). From a quantum well model, the sum $E_{1e}+E_{1hh}$ of the corresponding confinement energies are 22.4 meV and 40.15 meV for SQW-5 and SQW-4, respectively. Thus, under biaxial compression stress, the $Zn_{0.86}Cd_{0.14}Se$ layer is characterized by a fundamental heavy-hole to conduction band gap:

SQW-5: $E_{1h} = E_{1e} - E_{1hh} = E_{g\,Zn_{0.86}Cd_{0.14}Se} + 22.4\ meV + 7.0\ meV$
$$= 2.6649\ eV.$$

SQW-4: $E_{1h} = E_{1e} - E_{1hh} = E_{g\,Zn_{0.86}Cd_{0.14}Se} + 40.15\ meV + 7.0\ meV$
$$= 2.6826\ eV.$$

Subtracting the binding energy of a free exciton energy which we assume is 18 meV (same as a free exciton binding energy in bulk

ZnSe) from the above band gap energy, we obtained 2.6469 eV, as compared to the experimental value 2.6486 eV for sample SQW-5, and 2.6646 eV, as compared to experimental value 2.6605 for sample SQW-4, respectively.

The experimental PL data and numerical values computed from the discussed model are listed in Table XII.
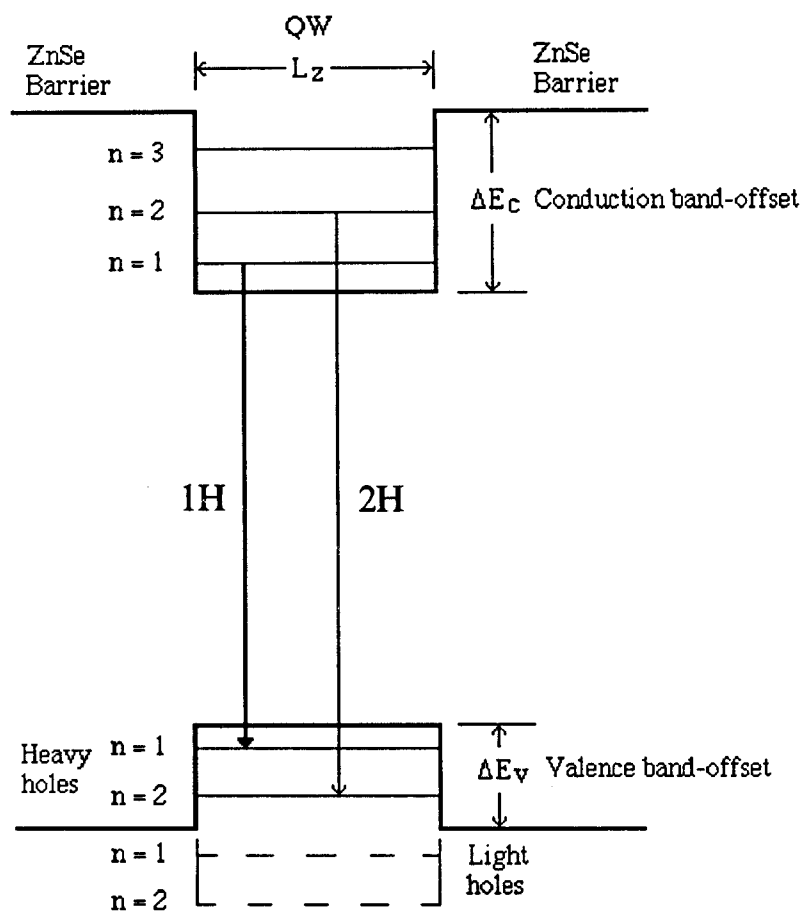
Figure 41. Schematic representation of $E_{1\text{-}1h}$ (1H) and $E_{2\text{-}2h}$ excitonic transitions in single quantum-wells.
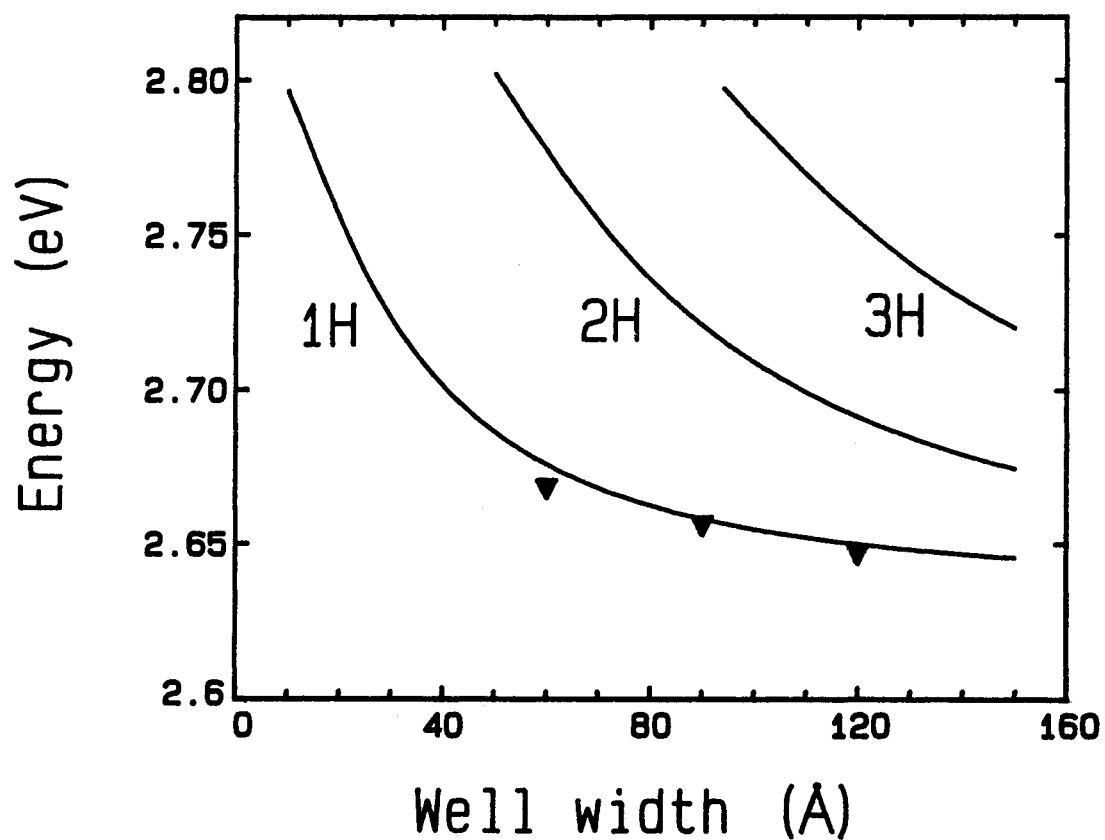
Figure 42.   Exciton transition energies as a function of well-
width. Symbols represents the experimental data
and solid line represents the theoretical values.

TABLE XII

140

Energies of the Photoluminescence observed transitions (at 8.7K) together with the results of calculations for electron confinement energies (E_{ne}) and ground-state heavy-hole (E_{nhh}) and strain induced shifts ($\Delta E_0(1)$) computed using parameters from Table I and II . The exciton binding energy E^b_{ex} used is 18meV. The last column indicates the sum of electron and heavy-hole confinement energies as a function of 5% well width fluctuations.

Sample Well width	Transition $[E_{ne}\text{-}E_{nhh}]$	Eg^a (eV)	E_{ne} (meV)	E_{nhh} (meV)	$\Delta E_0(1)$ (meV)	PL (eV)	Computed (eV)	Variation (meV)
SQW-4 60Å	[1 - 1]	2.6355	32.10	8.05	7.0	2.6605	2.6646	± 2.8
	[1 - 2]		32.10	27.80			2.6844	
	[2 - 1]		113.5	8.05			2.7461	
	[2 - 2]		113.5	27.80			2.7658	
SQW-5 90Å	[1 - 1]	2.6355	17.85	4.55	7.0	2.6486	2.6469	± 2.0
	[1 - 2]		17.85	17.40			2.6598	
	[2 - 1]		67.88	4.55			2.6969	
	[2 - 2]		67.88	17.40			2.7098	
	[3 - 1]		136.3	4.55			2.7654	
	[3 - 2]		136.3	17.40			2.7782	
SQW-6 120Å	[1 - 1]	2.6355	11.35	2.92	7.0	2.6393	2.6388	± 1.0
	[1 - 2]		11.35	11.48			2.6474	
	[1 - 3]		11.35	24.42			2.6603	
	[2 - 1]		44.03	2.92			2.6715	
	[2 - 2]		44.03	11.48			2.6800	
	[2 - 3]		44.03	24.42			2.6930	
	[3 - 1]		94.0	2.92			2.7214	
	[3 - 2]		94.0	11.48			2.7299	
	[3 - 3]		94.0	24.42			2.7429	
	[4 - 1]		149.3	2.92			2.7767	
	[4 - 2]		149.3	11.48			2.7853	
	[4 - 3]		149.3	24.42			2.7982	

a - using our calculation [Eqn. (4.1)].

4.5 Comparison:

Experimental results are in good agreement with the theoretical calculations. As can be seen from the Table XII, for SQW-5, the theoretical fundamental heavy-hole to conduction-band transition energy E_{1h} is 2.6469 eV, taking into account the confined carrier energy in the conduction band-offset as well as the valence band offset and the strain effects on heavy-hole transitions and the exciton binding energy. The experimental free-exciton peak is observed at 2.6486 eV in SQW-5. The difference between theory and experiment being 1.68 meV. Similarly we find a difference of 4.1 meV in SQW-4 and 0.5 meV in SQW-6, respectively.

In our calculation we use an effective mass ratio of $\sigma = m_e / m_h$ =0.269 and predict a binding energy for an exciton X trapped on an ionized donor D^+, of $E_{XD^+} = 1.12\ E_D$, where E_D is the binding energy of the isolated donor D^0. For a exciton bound to neutral donors D^0, we calculate a dissociation energy of $D_0 = 0.33\ E_D$, giving a binding energy of $E_{XD^0} = E_X + 0.33\ E_D$. Here E_X is the binding energy of the free exciton. The binding energy of exciton-neutral acceptor complex is estimated to be $E_{XA^0} = E_X + 0.09\ E_A$ for $Zn_{1-x}Cd_xSe$ QW. We estimate the photon emission energy $\hbar\omega$ of radiative annihilation of the exciton complexes (D^0,X), (D^+,X), (A^0,X), and (A^-,X) as [83]:

$$\hbar\omega(X_D0) = E_g - E_X - 0.33\ E_D$$

$$\hbar\omega(X_{D+}) = E_g - E_D - 0.12\ E_D$$

$$\hbar\omega(X_A0) = E_g - E_X - 0.09\ E_A$$

We find that the above mentioned relationship of exciton complexes, is consistent with the experimental observations in both the samples SQW-5 and SQW-4.

CHAPTER 5

SUMMARY AND CONCLUSIONS

In this research, an investigation of optical properties of three $Zn_{1-x}Cd_xSe$ single-quantum-wells has been made, for the first time, the temperature dependence of the photoluminescence from sphalerite $Zn_{0.86}Cd_{0.14}Se$ strained quantum well heterostructures in the range 8.7 - 300 K, in order to get some insight into the PL and RRS spectra. The temperature dependence of the photoluminescence from the 60Å, 90Å and 120Å $Zn_{0.86}Cd_{0.14}Se/$ ZnSe single quantum well are studied under indirect (by the UV 3.407 - 3.53 eV Argon laser and 3.396 eV Hg- UV line) and direct (by the 2.707 eV Argon laser line) excitation. The emission spectra obtained by the indirect excitation shows two emission bands, namely the free exciton and exciton bound to neutral donor which we believe is the Ga donor at the Zn or Cd site.

The directly excited quantum wells exhibit a free exciton PL band and a strong Raman peak in samples SQW-5 and SQW-6, and only a trace of a Raman peak in SQW-4. We observe resonant Raman scattering in $Zn_{0.86}Cd_{0.14}Se/$ ZnSe single QWs' for the first time. By

temperature tuning the bandgap, the E_{1h} exciton transition (in SQW-5) is brought into resonance with the double photon Raman scattering $\hbar\omega_{S2LO}$. This resonance occurs at a temperature of 50 K, which is almost the same temperature ($\sim$ 47 K) at which the E_{2hh} heavy-hole free exciton is in resonance with excitation laser energy (E_{ex}). The single quantum well SQW-4 shows E_{1h} exciton transition in resonance with a Raman scattered photon $\hbar\omega_{S2LO}$ at a temperature of $\sim$ 92 K, having a different temperature dependence as compared to sample SQW-5. If the temperature dependencies of SQW-5 and SQW-4 are the same, the single quantum well SQW-4 should show E_{1h} exciton transition in resonance with a Raman scattered photon at a temperature $\sim$ 108 K. The precise composition of the $Zn_{1-x}Cd_xSe$ single quantum-well as well the accurate measurement of the well-width (L_z) are the possible cause of any observed discrepancies. It will be very interesting to perform an experiment with a tunable dye laser in the range 2.6 - 2.8 eV to confirm our results.

In summary, this work reports a detailed comparison between the measured and calculated excitonic transitions in strained $Zn_{1-x}Cd_xSe$ heterostructure. Quantum wells have been modelled as finite square-potential wells and theoretical calculations are presented for the confined carrier energies, including band-nonparabolicity correction induced by an energy dependent effective mass, in a single quantum

well and calculated the strain and its effect on the energy transitions of the heterostructure. Theoretical calculations and experimental observations are in good agreement. The temperature dependencies of PL emission peak position, intensity and linewidth (FWHM) under direct and indirect excitation are analyzed and discussed in detail.

By temperature tuning of the bandgap, the E_{1h} exciton transition is brought into resonance with the Raman scattered photon $\hbar\omega_{S2LO}$. This resonance occurs at a temperature of 50 K in sample SQW-5, and coincides with the temperature ($\sim$ 47 K) at which the E_{2hh} heavy-hole free exciton is in resonance with the excitation laser energy (E_{ex}). Based on Hill's theory, the bandgap of $Zn_{1-x}Cd_xSe$ has been computed as a function of composition.

Circular polarization measurements show the spin-flip of resonant Raman peak and decrease or enhancement of free-exciton transition to heavy-hole band under $\sigma+$ and $\sigma-$ excitations, respectively.

From a device point of view, as a future work, one can develop a blue-green $Zn_{1-x}Cd_xSe$ QW laser by photopumping [70-72], and in an external-cavity configuration [73,74], adapting longitudinal pumping

technique and use of tight focus to improve beam quality and birefringent filter for tunability. Lithium doped ZnSe films and epilayers have been successfully grown recently [90] and there potential for p-n junction type of $Zn_{1-x}Cd_xSe$ light-emitting diodes (LEDs') and QW lasers in the near future.

REFERENCES

1. L. Esaki and R. Tsu, " Superlattice and Negative Conductivity in Semiconductors ", IBM Res. Note, RC-2418, March 1969.

2. L. Esaki and R. Tsu, " Superlattice and Negative Differential Conductivity in Semiconductors ", IBM J. Res. Develop., Vol. 14, 61, January 1970.

3. R. de L. Kronig and W. J. Penny, " Quantum Mechanics of Electrons in Crystal Lattices ", Proc. Roy. Soc. A130, 499 (1930).

4. R. Dingle, W. Weigmann, and C. H. Henry, " Quantum states of Confined Carriers in Very Thin $Al_xGa_{1-x}As$ -GaAs-$Al_xGa_{1-x}As$ Heterostructures ", Phys. Rev. Lett., Vol. 33, 827, Sept. 1974.

5. J. H. van der Merwe, " Crystal interfaces ", J. Appl. Phys., 34, 117 , January 1963.

6. G. C. Osbourn, " Strained-Layer Superlattices from Lattice Mismatched Materials ", J. Appl. Phys., 53, 1586, March 1982.

7. J. Tersoff, " The Theory of Heterojunction Band-Lineups ", in Heterojunction Band Discontinuities: Physics and Characterization, Edited F. Capasso and G. Margaritondo, Ch. 1, Elsevier Science Publishers, North Holland.

8. R. L. Anderson, " Experiments on Ge-GaAs Heterojunctions", Solid State Electron. 5, 341 (1962).

9. G. Margaritondo and J. H. Weaver, " Photoemission Spectroscopy of Valence State " in Methods of Experimental Physics, Vol. 22, Ch.4 (1985).

10. C. Mailhiot and C. B. Duke, " Many Electron Model of Equilibrium Metal-Semiconductor Contacts and Semiconductor Heterojunctions ", Phys. Rev. B, 33, 1118 (1986).

11. C. Tejedor and F. Flores, " A Simple Approach to Heterojunctions", J. Phys. C 11, L19 (1978).

12. W. A. Harrison, " Elementary Theory of Heterojunctions ", J. Vac. Sci. & Technol., 14, 1016 (1977).

13. W. R. Frensley and H. Kroemer, " Theory of Energy-Band Lineup at an Abrupt Semiconductor Heterojunction ", Phys. Rev. B 16, 2642 (1977).

14. G. Margaritondo and P. Perfetti, " The Problem of Heterojunction Band Discontinuities ", in Heterojunction Band Discontinuities: Physics and Characterization, Edited F. Capasso and G. Margaritondo, Ch. 2, Elsevier Science Publishers, North Holland.

15. J. Tersoff, " Theory of Semiconductor Heterojunctions: The Role of Quantum Dipoles ", Phys. Rev. B 30, 4874 (1984).

16. J. Menendez and A. Pinczuk, " Light Scattering Determinations of Band-Offsets in semiconductor heterostructures ", IEEE J. QuantumElectronics, Vol 24 (8), 1698, August 1988.

17. A. D. Katnani, " Trends in Semiconductor Heterojunctions ", in Heterojunction Band Discontinuities: Physics and

Characterization, Edited F. Capasso and G. Margaritondo, Ch. 3, Elsevier Science Publishers, North Holland.

18. C. G. van de Walle and R. M. Martin, " Theoretical Study of Band-Offsets Semiconductor Interfaces ", Phys. Rev. B 35, 8154 (1987).

19. S. Massida, B. I. Min, and A. J. Freeman, " Interface Phenomena at Semiconductor Heterojunctions: Local Density Valence Band-Offset in GaAs/ AlAs ", Phys. Rev. B 35, 9871 (1987).

20. R. Dingle, W. Weigman, and C. H. Henry, " Quantum States of Confined Carriers in Very Thin $Al_xGa_{1-x}As-GaAs-Al_xGa_{1-x}As$ Heterostructures ", Phys. Rev. Lett. 33, 827 (1974).

21. D. A. Broido and L. J. Sham, " Effective Mass of Holes at GaAs-AlGaAs Heterojunctions ", Phys. Rev. B, 31, 888 (1985).

22. G. Bastard and J. A. Brum, " Electronic States in Semiconductor Heterostructures ", IEEE J. Quantum Electronics, QE-22 (9), 1625 (1986).

23. M. A. Herman, D. Bimberg, and J. Christen, " Heterointerfaces in Quantum Wells and Epitaxial Growth Processes: Evaluation by Luminescence Techniques ", J. Appl. Phys. 70 (2), R1 (1991).

24. F. Bassani, " Methods of Band Calculations Applicable to III-V Compounds ", in Semiconductors and Semimetals, Vol. 1, Ch. 2, Academic Press, New York, 1966.

25. E. O. Kane, " The k.p Method ", in Semiconductors and Semimetals, Vol. 1, Ch. 3, Academic Press, New York, 1966.

26. M. P. Houng, Y. C. Chung, and W. I. Wang, " Orientation Dependence of Valence-Subband Structures in GaAs-Ga$_{1-x}$Al$_x$As Quantum Well Structures ", J. Appl. Phys. 64, 4609 (1988).

27. J. M. Luttinger, "Quantum Theory of Cyclotron Resonance in Semi-conductors: General Theory ", Physics Rev. 102, 1030 (1956).

28. D. Gershoni, H. Temkin, and M. B. Panish, " Excitonc Transitions in Lattice-matched Ga$_{1-x}$In$_x$As/ InP Quantum Wells ", Phys. Rev. B 38, 7870 (1988).

29. M. Grundmann and D. Bimberg, " Anisotropy Effects on Excitonic Properties in Realistic Quantum Wells ", Phys. Rev. B 38,13486 (1988).

30. D. Bimberg, in Vol. XVII, Vieweg, Braunschweig, (1977) or E. I. Rashba and M. D. Sturge, Editors, in Title Excitons, North Holland, Amestardam, 1982) as referenced in 29. D. Bimberg, J. Christen, A. Steckenborn, G. Weimann, and W. Schlapp, " Injection, Intersubband Relaxation and Recombination in GaAs Multiple Quantum Wells ", J. Lumin. 30, 562 (1985).

31. C. Weisbuch and B. Vinter, " The Electronic Properties of Thin Semiconductor Heterostructures ", Quantum Semiconductor Structures - Fundamentals and Applications, Ch. 2, Academic Press, New York, 1991, and references therein.

32. B. P. Zakharchenya, D. N. Mirlin, V. I. Perel, and I. I. Reshina, " Spectrum and Polarization of Hot-Electron Photoluminescence in Semiconductors ", Sov. Phys. Usp 25, 143 (1982).

33. H. Asai and K. Oe, " Energy Bandgap Shift with Elastic Strain in $Ga_xIn_{1-x}P$ Epilayers on (001) GaAs Substrates", J. Appl. Phys.54, (4), 2052 (1983).

34. G. E. Pikus and G. L. Bir, " Effect of Deformation on the Energy Spectrum and the Electrical Properties of Imperfect Germanium and Silicon ", Sov. Phys. Solid State 1, 136 (1959); " Effect of Deformation Potential on the Hole Energy Spectrum of Germanium and Silicon ", Sov. Phys. Solid State 1,1502 (1960).

35. Y. P. Varshni, " Temperature Dependence of the Energy Gap in Semiconductors ", Physica 34, 149 (1967).

36. D. S. Chemla, D. A. B. Miller, P. W. Smith, A. C. Gossard, and W. Weigman, " Room-Temperature Excitonic Nonlinear Absorption and Refraction in GaAs-AlGaAs Multiple Quantum-Well Structures", IEEE J.Quantum Electronics, QE-20, 265 (1984).

37. H. Iwamura, H. Kobayashi, and H. Okamota, " Excitonic Absorption Spectra of GaAs-AlAs Superlattice at High Temperature ", Japan J. Appl. Phys. 23, L795 (1984).

38. J. Lee, E. S. Kotels, and M. O. Vassel, " Luminescence Linewidths of Excitons in GaAs Quantum Wells Below 150 K ", Phys. Rev. B 33 (8), 5512 (1986).

39. Y. Shinozuka and M. Matsuura, "Wannier Excitons in Quantum Wells", Phys. Rev. B 28, 4878 (1983); 29, 3717 (1984).

40. W. C. Tait and R. L. Weiher, " Contribution of Scattering of Polaritons by Phonons to Absorption of Light Waves in II-VI

Crystals ", Phys. Rev. 166, 769 (1968); " Contributions of Scattering of Polaritons by Phonons to Emission of Radiation by Solids ", 178, 1404 (1969).

41. G. Bastard," Hydrogenic Impurity States in a Quantum Well: A Simple Model ", Phys. Rev. B 24, 4714 (1981).

42. R. C. Miller, D. A. Kleinman, W. A. Nordland, and A. C. Gossard, " Luminescence Studies of Optically Pumped Quantum Wells in GaAs-$Al_xGa_{1-x}As$ Multilayer Structures ", Phys. Rev. B 22, 863 (1980).

43. C. Weisbuch, R. C. Miller, R. Dingle, and A. C. Gossard, " Intrinsic Radiative Recombination from Quantum States in GaAs-$Al_xGa_{1-x}As$ Multi-Quantum Well Structures ", Solid State Communications, 37, 219 (1981).

44. J. E. Zucker, A. Pinczuk, D. S. Chemla, A. C. Gossard, and W. Weigman, " Raman Scattering with Quasi-2D Excitons in Semi-conductor Quantum Wells ", Phys. Rev. Lett., 51 (14), 1293 (1983).

45. A. K. Sood, J. Menendez, M. Cardona, and K. Ploog, " Second-Order Raman Scattering by Confined Optical Phonons and Interface Vibrational Modes in GaAs-AlAs Superlattices ", Phys. Rev. B 32 (2), 1412 (1985).

46. J. Menendez, M. Cardona, and L. K. Vodopyanov, " Resonance Raman Scattering by LO Phonons in $Cd_xHg_{1-x}Te$ at the $E_0+\Delta_0$ Gap ", Phys. Rev. B 31 (6), 3705 (1985).

47. A. S. Nasibov, Yu. V. Korostelin, P. V. Shapkin, L. G. Suslina, D.L. Fedorov and L.S. Markov, " Exciton Luminescence in Ideal Solid Solutions ($Zn_xCd_{1-x}Se$ system, 0<x<1) ", Solid State Commun. 71, 867 (1989).

48. D. S. Jiang, H. Jung, and K. Ploog, " Temperature Dependence of Photoluminescence from GaAs Single and Multiple Quantum Well Heterostructures Grown by Molecular-Beam-Epitaxy ", J. Appl. Phys. 64, 1371 (1988).

49. E. H. Reihlen, A, Persson, T. Y. Wang, K. L. Fry and G. B. Stringfellow, " Photoluminescence Study of Carrier Collection and Recombination in Thin GaInAs/ Inp Single Quantum Wells, J. Appl. Phys., 66, 5554 (1989).

50. P. O. Holtz, B. Monemar, and H. J. Lozykowski, " Optical Properties of Ag-related Centers in Bulk ZnSe ", Phys. Rev. B 32, 986 (1985).

51. M. Cardona, in Light Scattering in Solids II, edited by M. Cardona and G. Guntherodt, Vol. 50, Topics in Applied Physics,(Springer, Berlin, 1982), p 50, and references therein.

52. R. C. Miller, D. A. Kleinman, and A. C. Gossard, " Observation of Doubly Resonant LO-Phonon Raman Scattering with GaAs-$Al_xGa_{1-x}As$ Quantum Wells ", Solid State Comm. 60, 213 (1986).

53. J. Menendez, " Phonons in GaAs- $Al_xGa_{1-x}As$ Superlattices ", J. Lumin. 44, 285 (1989).

54. H. J. Lozykowski and V. K. Shastri, " Excitonic and Raman Properties of ZnSe/ $Zn_{1-x}Cd_xSe$ Strained-Layer Quantum Wells ", J. Appl. Phys. 69 (5), 3235 (1991).

55. M. Y. Valakh, A. P. Litvinchuk, R. S. Pekar, and A. M. Yaremko, " Resonant Raman Scattering of Light in $Zn_{1-x}Cd_xSe$ Crystals ", Phys. Status Solidi (B) 113, 635 (1982).

56. R. Hill, " Energy-Gap Variations in Semiconductor Alloys ", J. Phys. C7, 521 (1974).

57. W. Girit and J. K. Furdyna, in Semiconductors and Semimetals, Vol. 25, Ch.1, 1 (1988).

58. Y. S. Park and D.C. Reynolds, " Exciton Structure in Photoconductivity of CdS, CdSe and CdS:Se Single Crystals ", Phys. Rev.132, 2450(1963).

59. B. Ray, II - VI compounds (Pergman Press, New York, 1969).

60. H. Kromer, " Theory of Heterojunctions: a Critical Review ", in Molecular Beam epitaxy and heterostructures, NATO ASI series E Applied Sciences, No. 87, edited by L.L. Chang and K. Ploog, Martinus Nijhoff Pub., 331 (1985).

61. C. K. Williams, T. H. Glisson, M. A. Little John and J. R. Hauser, " Ballistic Transport in GaAs ", IEEE Electron Device Lett. EDL-4, 161 (1983).

62. D. F. Welch, G. W. Wicks and L. F. Eastman, " Calculation of the Conduction Band Discontinuity for $Ga_{0.47}In_{0.53}As/$

$Al_{0.48}In_{0.52}As$ Heterjunction ", J. Appl. Phys. 55, 3176 (1984).

63. R. M. Martin, " Relation Between Elastic Tensors of Wurtzite and Zinc-Blende Structure Materials ", Phys. Rev. B6, 4546 (1972).

64.   D. L. Camphausen, Connell, and W. Paul, " Calculation of Energy-Band Pressure Coefficients from the Dielectric Theory of the Chemical Bond ", Phys. Rev. Lett. 26, 184 (1971).

65. N. Samarth, H. Luo, J. K. Furdyna, S. B. Qadri, Y. R. Lee, A. K. Ramdas, and N. Otsuka, " Growth of Cubic (zinc-blende) CdSe by Molecular Beam Epitaxy ", Appl. Phys. Lett. 54, 2680 (1989).

66. N. Samarth, H. Luo, J. K. Furdyna, R. G. Alonso, Y. R. Lee, A. K. Ramdas, S. B. Qadri, and N. Otsuka, " Molecular Beam Epitaxy of $Zn_{1-x}Cd_xSe$ Epilayers and ZnSe/ $Zn_{1-x}Cd_xSe$ Superlattices ", Appl. Phys. Lett. 56, 1163 (1990).

67.   P. Manuel, G. A. Sai-Halasz, L. L. Chang, Chin-An Chang, L. Esaki, " Resonant Raman Scattering in a Semiconductor Superlattice ", Phys. Rev. Lett. 37, 1701 (1976).

68.   G. A. Sai -Halasz, A. Pinczuk, P. Y. Yu, and L. Esaki, " Resonance Enhanced Umklapp Raman Processes in $GaAs-Ga_{1-x}Al_xAs$ Super-lattices ", Solid Sate Commun. 25, 381 (1978).

69.   D. A. Kleinman, R. C. Miller, and A. C. Gossard, " Doubly Resonant LO Phonon Raman Scattering Observed with $GaAs-Al_xGa_{1-x}As$ Quantum Wells", Phys. Rev. B 35, 664 (1987).

70.   I. Suemune, K. Yamada, H. Masato, Y. Kan, and M. Yamanishi, " Lasing in a $ZnS_{0.12}Se_{0.88}$ / ZnSe Multilayer Structure with

Photopumping ", Appl. Phys. Lett. 54 (11), 981 (1989).

71.   J. Ding, H. Jeon, A. V. Nurmikko, H. Luo, N. Samarth, and J. K. Furdyna, " Laser Action in the Blue-Green from Optically Pumped (Zn,Cd)Se/ ZnSe Single Quantum Well Structures ", Appl. Phys. Lett. 57 (26), 2756 (1990).

72.   H. Jeon, J. Ding, A. V. Nurmikko, H. Luo, N. Samarth, and J. K. Furdyna, W. A. Bonner and R. E. Nahory, " Room-temperature Blue Lasing action in (Zn,Cd)Se/ ZnSe Optically Pumped Multiple Quantum Well Structures on Lattice-Matched (Ga,In)As Substrates ", Appl. Phys. Lett. 57 (23), 2413 (1990).

73.   C. B. Roxlo, R. S. Putnam, and M. M. Salour, " Optically Pumped Semiconductor Platelet Lasers ", IEEE J. Quantum Electronics, QE-18 (3), 338 (1982).

74.   A. Fuchs, D. Bebelaar, and M. Salour, " Optically Pumped CW Semiconductor Ring Laser ", Appl. Phys. Lett. 43 (1), 32 (1983).

75. J. S. Blakemore, " Semiconducting and Other Major Properties of GaAs ", J. Appl. Phys. 53, R123 (1982).

76. J. L. Freeouf and J. M. Woodall, " Schottky Barriers: An Effective Work Function Model ", Appl. Phys. Lett. 39, 727 (1981).

77. H. J. Lozykowski and V. K. Shastri, " Excitonic Properties of ZnSe/ $Zn_{1-x}Cd_xSe$ Strained Layer Quantum Wells ", J. Lumin. 48 & 49, 740 (1991).

78. H. J. Lozykowski, V. Shastri, T. Li, N. Samarth, H. Luo, and J. K. Furdyna, " Photoluminescence Studies of ZnSe - $Zn_{1-x}Cd_xSe$

Quantum Wells ", Bull. Am. Phys. Soc., Vol. 35 (3), M20.2 (1990).

79. H. J. Lozykowski, V. Shastri, T. Li, N. Samarth, H. Luo, and J. K. Furdyna, " Excitonic Properties of ZnSe - $Zn_{1-x}Cd_xSe$ Strained Layer Quantum Wells, ICL-90, Lisbon, Portugal, 16-20 July 1990.

80. J. R. Haynes, " Experimental Proof of the Existence of a New Electronic Complex in Silicon ", Phys. Rev. Lett. Vol. 4(7), 361 (1960).

81. G. Abstreiter and K. Ploog, " Inelastic Light Scattering from a Quasi-Two-Dimensional Electron System in GaAs - $Al_xGa_{1-x}As$ Heterojunctions ", Phys. Rev. Lett. 42 (19), 1308 (1979).

82. E. H. Bogardus, H. B. Bebb, and R. A. Reynolds Bull. Am. Phys. Soc., 13, 497 (1968).

83. E. H. Bogardus and H. B. Bebb, " Bound-Exciton, Free-Exciton, Band-Acceptor, Donor-Acceptor, and Auger Recombination in GaAs ", Phys. Rev., 176 (3), 993 (1968).

84. R. R. Sharma and S. Rodriguez, " Theory of Excitons Bound to Ionized Impurities in Semiconductors ", Phys. Rev. 153, 823 (1967), " Exciton-Donor Complexes in Semiconductors ", 159, 649 (1967).

85. J. J. Hopfield, " Theory of the Contribution of Excitons to the Complex Dielectric Constant of Crystals ", Phys. Rev. 112 (5), 1555 (1958).

86. V.I. Zemskii, B. P. Zakharchenya, and D.N. Mirlin, " Polarization of Hot Photoluminescence in Semiconductors of the GaAs type ",

Soviet Phys., JETP Lett. 24 (2), 82 (1976).

87. M. I. D' yakonov and V. I. Perel', " Circular Polarization of Recombination Light of Semiconductors in a Weak Magnetic Field", Soviet Physics-Solid State, 14(5), 1245 (1972).

88. B. P. Zakharachenya, Proc. Eleventh International Conference on Physics of Semiconductors, Warsaw, 1312 (1972).

89. R. C. Miller and D. A. Kleinman, "Excitons in GaAs Quantum Wells", J. Lumin. 30, 520 (1985).

90. K. Hingerl, H. Sitter, J. Lilja, E. Kuusisto, K. Imal, M. Pessa,G. Kudlek, and J. Gutowski, " Electrical and Optical Properties of Li-Doped MBE Grown p-type ZnSe Films ", Semicond. Sci. Technol. 6, A72 (1991).

91. D. W. Langer, R.N. Euwema, K. Era, and T. Koda, " Spin Exchange in Excitons, the Quasicubic Model and Deformation Potentials in II-VI Compounds ", Phys. Rev. B 2, 4005 (1970).

92. G. A. Kourouklis, A. Jayaraman, R. People, S.K. Sputz, R. G. Maines, Sr.,D. L. Sivco, and A.Y. Cho, " Pressure-Induced Resonance Raman Scattering in $Ga_{1-x}In_xAs/ Ga_{1-y}Al_yAs$ Strained Quantum-Well Structures ", J. Appl. Phys. 67 (10), 6438 (1990).

APPENDICES

The appendices contain computer programs written in FORTRAN. The complete listing of the program together with several numerical examples and pertinent outputs are included.

Program #1   compute the bowing parameter

Program #2   compute the bandgap as a function of composition, the band-nonparabolicity, and the effective mass.

Program #3   compute the band-offsets.

Program #4   compute strain, and strain shifts due to heavy-hole, light-hole and split-off bands.

Program #5a   confined carrier energies in the conduction-band.

Program #5b   confined carrier energies in the valence-band.

```
C    Program to compute the bowing parameter
C    based on Hill's theory :  Program # 1
C    Program for Equation # (4.2) by Vasant Shastri
C
     REAL  A1,A2,A,RM,RN,Z,Q,E,S,B,PI,VAL,TERM2,TERM3
C    A1 - the lattice constant of compound M
C    A2 - the lattice constant of compound N
C    A  - the lattice constant of the mixed composition
C    RM & RN -  Pauling constants for material M & N
C    Z   - the valence number of the substitution ion
C    E   - the dielectric constant
C    Q   - the charge of an electron
C    S   - the screening constant
C    TERM2 & TERM3 - intermediate terms in calculation
C
     WRITE(6,*) ' Enter the valence number Z '
     READ(5,*) Z
     WRITE(6,*) ' Enter r(M) & r(N) '
     READ(5,*) RM,RN
     WRITE(6,*) ' Enter lattice constants of M & N '
     READ(5,*) A1,A2
C    Compute the lattice constant of mid-composition alloy
     A= (A1+A2)/2
C    Use the constants
     E=8.85E-12
     Q=1.602E-19
     S=0.25E10
     PI=3.141593
C    Now compute the bowing parameter
```

```
            VAL=(-S*A*0.216506)
            TERM3=(RM+RN)*(EXP(VAL))
            TERM2=(((1/RM)-(1/RN))**2)
        B=((Z*Q)/(8*PI*E))*TERM2*TERM3
C   Write the computed values
            WRITE(6,*) ' The lattice constant (mixed alloy) : ',A
            WRITE(6,*) ' The computed bowing parameter : ',B
        STOP
        END
```

EXAMPLE #1

Computation of bowing parameter for $Zn_{1-x}Cd_xSe$ mixed alloy, let us execute the Program #1 as below :

For the prompts of the program M: Zn and N:Cd, enter the following values:

Enter the valence number Z	**2**
Enter r(M) & r(N)	**1.225, 1.405**
Enter lattice constants of M & N	**5.6676, 6.077**

The lattice constant (mixed alloy) : 5.8723

The computed bowing parameter :   0.301164

```
C    Program to compute the Bandgap, effective mass and
C    band nonparabolicity : Program # 2
C    Program for Equation # (4.1) & (4.5) by Vasant Shastri
C
     REAL  EG1,EG2,X,B,M1,M2
C    EG1 - the bandgap of compound M
C    EG2 - the bandgap of compound N
C    X   - the value of Cd in the mixed composition alloy
C    M1 & M2 -  effective masses for electron & holes respectively
C    B   - theoretically computed bowing parameter
C
     WRITE(6,*) ' Enter the bandgap of compound M '
     READ(5,*) EG2
     WRITE(6,*) ' Enter the bandgap of compound N '
     READ(5,*) EG1
     WRITE(6,*) ' Enter the START  x-value '
     READ(5,*) X
     WRITE(6,*) ' Enter the STOP  x-value & STEP '
     READ(5,*) X2, DX
     WRITE(6,10)
10   FORMAT (' ',2X,' X ', 2X, ' EGX ', 2X, ' M1 ', 2X, ' A1 ',
     +              2X, ' M2 ', 2X, ' A2 ' )
C    to compute a table of RESULTS
C    Loop
15   CONTINUE
     IF (X.GE.X2) GOTO  20
     EGX=EG1 + ((EG2-EG1-B)*(1-X)) + B*((1-X)**2)
     M1=0.13 + (1-X)*0.03
     A1=((1-M1)**2)/EGX
```

```
            M2=0.45 + (1-X)*0.15
            A2=((1-M2)**2)/EGX
C    to write the computed values
            WRITE(6,25) X, EGX, M1, A1, M2, A2
25   FORMAT(' ',2X, F5.4,2X, F8.6, 4(2X, F8.6))
            X=X+DX
            GOTO  15
20   CONTINUE
        STOP
        END
```

```
C    Program to compute the Band-offsets
C    based on HAO theory :  Program # 3
C    Program using TABLE I & IX :  by Vasant Shastri
C
        REAL  XM, XN, X, DELTAX, XCOMP,EM, EN, ECOMP
        REAL DELXC, DELXV, DELEG, DELEC, DELEV, DELTAE
C    XM - the electron affinity of compound M
C    XN - the electron affinity of compound N
C    X  - the value of Cd  in the mixed composition alloy
C    EM & EN -  valence band energies of  M & N respectively
C
        WRITE(6,*) ' Enter the composition x '
        READ(5,*) X
        WRITE(6,*) ' Enter  delta Eg '
        READ(5,*) DELEG
        WRITE(6,*) ' By electron-affinity-rule : '
        WRITE(6,*) ' ( Conduction band-offset first) '
        WRITE(6,*) ' Enter Chi-value of M & N '
        READ(5,*) XM, XN
            DELTAX=ABS(XM-XN)
            XCOMP=XN-(1-X)*DELTAX
        DELXC=XCOMP - XM
        DELXV=DELEG - DELXC
        WRITE(6,*) ' The conduction band-offset = ', DELXC
        WRITE(6,*) ' The valence band-offset = ', DELXV
        WRITE(6,*) ' By Harrison Atomiclike theory : '
        WRITE(6,*) ' ( Valence band-offset first) '
        WRITE(6,*) ' Enter energy-value of M & N '
        READ(5,*) EM, EN
```

```
          DELTAE=ABS(EM-EN)
          ECOMP=EN-(1-X)*DELTAE
      DELEV=ECOMP - EM
      DELEC=DELEG - DELEV
      WRITE(6,*) ' The valence band-offset = ', DELEV
      WRITE(6,*) ' The conduction band-offset = ', DELEC
   STOP
END
```

EXAMPLE #2

Computation of band-offset for $Zn_{1-x}Cd_xSe$ mixed alloy, let us execute the Program #3 as below :

For the prompts of the program M: Zn and N:Cd, enter the following values:

Enter the composition x	**0.14**
Enter delta Eg	**0.18548**

By electron-affinity-rule :

(Conduction band-offset first)

Enter Chi-value of M & N   **4.09, 4.95**

The conduction band-offset =   0.1204

The valence band-offset =   0.06508

By Harrison Atomiclike theory :

(Valence band-offset first)

Enter energy-value of M & N   **-1.05, -0.82**

The valence band-offset =   0.0322

The conduction band-offset =   0.15328

```
C    Program to compute the Strain  and strain effects
C    on the confined carrier energies :  Program # 4
C    Program for Equation # (4.6) & (4.7)  by Vasant Shastri
C
        REAL  AM, AN, DELA, ALLOY, STRAIN, X, A1, A2, A3
        REAL TERM1, TERM2, B1, B2, B3, DE01, DE02, DE03
        REAL C11M, C12M, C11N, C12N, C11, C12
C    AM & AN - the lattice constants of  M & N
C    A1, A2, A3 -  hydrostatic deformation potentials
C    B1, B2, B3 -  shear deformation potential
C    X   - the value of  Cd  in the mixed composition alloy
C    Cij -  elastic stiffness of M & N compounds
C
            WRITE(6,*) ' Enter the lattice constant of M &N '
            READ(5,*) AM, AN
            WRITE(6,*) ' Enter the composition x '
            READ(5,*) X
        ALLOY=AM*(1-X) + AN*X
        DELA=ABS(ALLOY-AM)
            STRAIN=DELA/AM
C    write the computed strain
            WRITE(6,*) X, ALLOY, STRAIN
C    enter the material parameters
            WRITE(6,*) ' Enter the hydrostatic/shear potential of M '
            READ(5,*) A1,B1
            WRITE(6,*) ' Enter elastic stiffness c11 & c12 for M '
            READ(5,*) C11M, C12M
            WRITE(6,*) ' Enter the hydrostatic/shear potential of N '
            READ(5,*) A2,B2
```

```
        WRITE(6,*) ' Enter elastic stiffness c11 & c12 for N '
        READ(5,*) C11N, C12N
C    compute the parameters for the ternary/mixed compound
        A3=A1*(1-X) + A2*X
        B3=B1*(1-X) + B2*X
        C11=C11M*(1-X) + C11N*X
        C12=C12M*(1-X) + C12N*X
C    compute the intermediate terms
        TERM1=(C11 - C12)/C11
        TERM2=(C11 + 2*C12)/C11
C    compute the strain effect due to heavy-hole
        DE01=((-2*A3*TERM1) + (B3*TERM2))* STRAIN
C    compute the strain effect due to light-hole
DE02=((-2*A3*TERM1) - (B3*TERM2))* STRAIN
C    compute the strain effect due to split-off band
        DE03=(-2*A3*TERM1)* STRAIN
C    now write the results
        WRITE(6,*) ' The computed strain shifts are : '
        WRITE(6,*) '  for heavy-hole ', DE01
        WRITE(6,*) '  for light-hole ' , DE02
        WRITE(6,*) '  for split-off band ' , DE03
     STOP
   END
```

```
C   Program to compute the confined carrier energies
C   in the quantum well :  Program # 5a
C   Program for Equation # (4.3)  by Vasant Shastri
C
        REAL  X1, X2, X3, ABSERR, DELX, V, LZ
        INTEGER N
        LOGICAL  OK
        COMMON / BLK / V, LZ
C   LZ - width of the quantum well
C   V -  depth of the quantum well
C   X1, X2 -  bounds of root finding limits
C   X   - the root/ bound state in the well
C   DELX - increment value
C
            WRITE(6,*) ' Transitions in the conduction band '
            WRITE(6,*) ' Enter the barrier height (band-offset) V '
            READ(5,*) V
            WRITE(6,*) ' Enter the well width Lz '
            READ(5,*) LZ
        X1=1E-3
        X3=(V-5E-4)
            DELX=1E-4
            ABSERR=1E-6
        N=1
10  CONTINUE
        IF (X. GE. X3) GOTO 20
            X=X1
            X2=X1 + DELX
        CALL  ESTATE ( X1, X2, ABSERR, ROOT, OK)
```

```
            IF (OK) THEN
            WRITE(6,*) ' The root for n = ', N, ' is ', ROOT, ' eV '
                N=N + 1
            ENDIF
                X=X + DELX
                X1=X
            GOTO 10
20  CONTINUE
            STOP
        END
C  ===================================================
            REAL  FUNCTION  QWELL (X)
C
            REAL  X
            REAL  V, LZ
            COMMON / BLK / V, LZ
C
            REAL B1, C1, KW, KB, MB, MW, B
C   MB & MW -  effective masses for the well & barriers
C
            B= 5.121934E9
            MB= 0.1558* (1 + 0.541 * X)
            MW= 0.1558* (1 + 0.541 * X)
            KB= B*SQRT(MB* (V - X))
            KW= B*SQRT(MW* X)
            C1=KW* LZ
            B1=(((KW*MB)**2) - ((KB*MW)**2)) / (KW*MW*KB*MB)
            QWELL = (B1*SIN(C1) - 2*COS(C1))
        RETURN
        END
```

```
C ========================================================
      SUBROUTINE  ESTATE ( X1, X2, EPS, ROOT, OK)
C
      REAL X1, X2, EPS, ROOT
      LOGICAL  OK
C
      REAL XX1, XX2, EEPS
      REAL MID, FX1, FX2, FMID
C    begin finding the roots
      XX1=X1
      XX2=X2
      EEPS=EPS
         IF(EEPS.LT.1E-4) EEPS = 1E-4
      FX1=QWELL (XX1)
      FX2=QWELL (XX2)
         IF (FX1*FX2.GT.0.0) THEN
             OK = .FALSE.
         ELSE
10  CONTINUE
      MID=(XX1 + XX2)/2.0
      IF (ABS(XX1 - XX2) . LT. EEPS) GO TO  20
         FMID=QWELL (MID)
      IF (FX1*FMID) . LT. 0.0 ) THEN
         XX2=MID
         FX2=FMID
      ELSE
         XX1=MID
         FX1=FMID
      ENDIF
         GO TO 10
```

```
20  CONTINUE
            ROOT=MID
            OK= .TRUE.
        ENDIF
     RETURN
    END
```

```
C   Program to compute the confined carrier energies
C   in the quantum well :  Program # 5b
C   Program for Equation # (4.3)  by Vasant Shastri
C
        REAL  X1, X2, X3, ABSERR, DELX, V, LZ
        INTEGER N
        LOGICAL  OK
        COMMON / BLK / V, LZ
C   LZ - width of the quantum well
C   V -  depth of the quantum well
C   X1, X2 -  bounds of root finding limits
C   X  - the root/ bound state in the well
C   DELX - increment value
C
        WRITE(6,*) ' Transitions in the valence band '
        WRITE(6,*) ' Enter the barrier height (band-offset) V '
        READ(5,*) V
        WRITE(6,*) ' Enter the well width Lz '
        READ(5,*) LZ
    X1=1E-3
    X3=(V-5E-4)
        DELX=1E-4
        ABSERR=1E-6
    N=1
10  CONTINUE
        IF (X. GE. X3) GOTO 20
            X=X1
            X2=X1 + DELX
        CALL  ESTATE ( X1, X2, ABSERR, ROOT, OK)
```

```
                IF (OK) THEN
                WRITE(6,*) ' The root for n = ', N, ' is ', ROOT, ' eV '
                   N=N + 1
                ENDIF
                   X=X + DELX
                   X1=X
                GOTO 10
20  CONTINUE
                STOP
            END
C  =================================================
                REAL  FUNCTION  QWELL (X)
C
                REAL  X
                REAL  V, LZ
                COMMON / BLK / V, LZ
C
                REAL B1, C1, KW, KB, MB, MW, B
C    MB & MW -  effective masses for the well & barriers
C
                B= 5.121934E9
                MB= 0.5790* (1 + 0.1345 * X)
                MW= 0.5790* (1 + 0.1345 * X)
                KB= B*SQRT(MB* (V - X))
                KW= B*SQRT(MW* X)
                C1=KW* LZ
                B1=(((KW*MB)**2) - ((KB*MW)**2)) / (KW*MW*KB*MB)
                QWELL = (B1*SIN(C1) - 2*COS(C1))
            RETURN
            END
```

```
C ===========================================================
          SUBROUTINE  ESTATE ( X1, X2, EPS, ROOT, OK)
C
          REAL X1, X2, EPS, ROOT
          LOGICAL   OK
C
          REAL XX1, XX2, EEPS
          REAL MID, FX1, FX2, FMID
C     begin finding the roots
          XX1=X1
          XX2=X2
          EEPS=EPS
              IF(EEPS.LT.1E-4) EEPS = 1E-4
          FX1=QWELL (XX1)
          FX2=QWELL (XX2)
              IF (FX1*FX2.GT.0.0) THEN
                  OK = .FALSE.
              ELSE
10   CONTINUE
          MID=(XX1 + XX2)/2.0
          IF (ABS(XX1 - XX2) . LT. EEPS) GO TO  20
              FMID=QWELL (MID)
          IF (FX1*FMID) . LT. 0.0 ) THEN
              XX2=MID
              FX2=FMID
          ELSE
              XX1=MID
              FX1=FMID
          ENDIF
              GO TO 10
```

```
20  CONTINUE
            ROOT=MID
            OK= .TRUE.
        ENDIF
      RETURN
      END
```

EXAMPLE #3

Computation of confined carrier energies for $Zn_{1-x}Cd_xSe$ mixed alloy QW, let us execute the Program #5a & 5b as below :

Transitions in the conduction band

Enter the barrier height (band-offset) V   **0.15328**

Enter the well width Lz   **9e-9**

The root for n = 1 is   17.85 e-3 eV

The root for n = 2 is   67.88 e-3 eV

The root for n = 3 is   136.3e-3 eV

Transitions in the valence band

Enter the barrier height (band-offset) V   **32.2e-3**

Enter the well width Lz   **9e-9**

The root for n = 1 is   4.55 e-3   eV

The root for n = 2 is   17.4 e-3   eV

Transitions in the conduction band

Enter the barrier height (band-offset) V   **0.15328**

Enter the well width Lz   **6e-9**

The root for n = 1 is   32.1 e-3   eV

The root for n = 2 is   113.5 e-3   eV

Transitions in the valence band

Enter the barrier height (band-offset) V **32.2e-3**

Enter the well width Lz **6e-9**

The root for n = 1 is   8.05 e-3   eV

The root for n = 2 is   27.8 e-3   eV